Layer-by-layer Self-assembled Active Electrodes for Hybrid Photovoltaic Cells

DISSERTATION

zur Erlangung des akademischen Grades
doctor rerum naturalium
(Dr. rer. nat.)
im Fach Physik

eingereicht an der
Mathematisch-Naturwissenschaftlichen Fakultät I
Humboldt-Universität zu Berlin

von
Herrn Dipl.-Phys. Rolf Kniprath
geboren am 24.02.1978 in München

Präsident der Humboldt-Universität zu Berlin:
Prof. Dr. Dr. h.c. Christoph Markschies

Dekan der Mathematisch-Naturwissenschaftlichen Fakultät I:
Prof. Dr. Lutz-Helmut Schön

Gutachter:

1. Priv.-Doz. Dr. Stefan Kirstein
2. Prof. Dr. Recardo Manzke
3. Prof. Dr. Dieter Neher

eingereicht am:	28.07.2008
Tag der mündlichen Prüfung:	18.11.2008

Für meine Eltern.

‘We will make electricity so cheap that only the rich will burn candles.’

Thomas Alva Edison (1847–1931)

‘The more physics you have the less engineering you need.’

Lord Ernest Rutherford (1871–1937)

Summary

Solar cells based on thin organic / inorganic heterofilms are currently in the focus of research, since they represent promising candidates for cost-efficient photovoltaic energy conversion. In this type of cells, charges are separated at a heterointerface between dissimilar electrode materials. These materials either absorb light themselves, or they are sensitized by an additional absorber layer at the interface.

The present work investigates photovoltaic cells which are composed of nanoporous TiO_2 combined with conjugated polymers and semiconductor quantum dots (QDs). The method of layer-by-layer self-assembly of oppositely charged nanoparticles and polymers is used for the fabrication of such devices. This method allows to fabricate nanoporous films with controlled thicknesses in the range of a few hundred nanometers to several micrometers. Investigations with scanning electron (SEM) and atomic force microscopy (AFM) reveal that the surface morphology of the films depends only on the chemical structure of the polyions used in the production process, and not on their molecular weight or conformation. From dye adsorption at the internal surface of the electrodes one can estimate that the internal surface area of a 1 μm thick film is up to 120 times larger than the projection plane. X-ray photoelectron spectroscopy (XPS) is used to demonstrate that during the layer-by-layer self-assembly at least 40% of the TiO_2 surface is covered with polymers. This feature allows to incorporate polythiophene derivatives into the films and to use them as sensitizers for TiO_2. Further, electrodes containing CdSe or CdTe quantum dots (QDs) as sensitizers are fabricated.

For the fabrication of photovoltaic cells the layer-by-layer grown films are coated with an additional polymer layer, and Au back electrodes are evaporated on top. The cells are illuminated through transparent doped SnO_2 front electrodes. The I/V curves of all fabricated cells show diode behaviour in the dark and a pronounced photovoltaic effect in simulated sunlight. Measurements of the photocurrent action spectra of the devices reveal that the charge injection efficiencies of the absorbers are different. While CdSe QDs effectively sensitize TiO_2, CdTe QDs do not. This finding is attributed to

different strengths of the charge carrier confinement in the QDs.

The power conversion efficiency is optimized and the charge transport is investigated by a variation of the cell structure with respect to the layer thicknesses and composition. Comparisons with simulated diode I/V curves show that the efficiencies of the cells investigated here are limited by high internal resistances of the cells.

Zusammenfassung

Solarzellen aus organisch / anorganischen Dünnschichtmaterialien sind Gegenstand der aktuellen Forschung und gelten als aussichtsreiche Kandidaten für eine kostengünstige photovoltaische Energieumwandlung. Bei diesem Zelltyp geschieht Ladungstrennung an der Grenzschicht zweier unterschiedlicher Elektrodenmaterialien, die entweder selbst Licht absorbieren oder durch eine zusätzliche Absorberschicht an der Grenzfläche sensibilisiert werden.

In der vorliegenden Arbeit werden photovoltaische Zellen untersucht, die sich aus nanoporösem TiO_2 sowie konjugierten Polymeren und Halbleiter-Quantenpunkten (QP) zusammensetzen. Zum Aufbau der Zellen wird die schichtweise, alternierende Adsorption entgegengesetzt geladener Nanopartikel und Polyionen verwendet. Diese Methode erlaubt die Herstellung nanoporöser Filme mit kontrollierten Dicken im Bereich von wenigen hundert Nanometern bis zu mehreren Mikrometern. Rasterelektronen- (SEM) und rasterkraftmikroskopische (AFM) Untersuchungen zeigen, dass die Oberflächenmorphologie der Schichten nur von der chemischen Struktur der verwendeten Polymere abhängt, nicht dagegen von ihrem Molekulargewicht und ihrer Konformation. Durch die Adsorption von Farbstoffen an der inneren Oberfläche der Elektroden kann abgeschätzt werden, dass die interne Fläche bei 1 μm Schichtdicke bis zu 120 mal größer ist als die Grundfläche. Mit Hilfe von Röntgen-Photoelektronenspektroskopie (XPS) wird gezeigt, dass beim Schichtaufbau mindestens 40% der TiO_2-Oberfläche mit Polymeren bedeckt wird. Dieser Umstand ermöglicht den Einbau von Polythiophen-Derivaten in die Filme und ihre Verwendung als Sensibilisatoren für TiO_2. Außerdem werden Elektroden hergestellt, die neben TiO_2 kolloidale CdSe- oder CdTe-QP als Sensibilisatoren enthalten.

Zur Herstellung photovoltaischer Zellen werden die schichtweise produzierten Heterofilme mit einem zusätzlichen Polymerfilm versehen und anschließend Au-Elektroden aufgedampft. Die Beleuchtung erfolgt durch transparente Frontelektroden aus dotierten SnO_2-Schichten. Die Strom-Spannungs-Kennlinien aller so hergestellten Zellen zeigen

im Dunkeln eine Diodencharakteristik und bei Beleuchtung mit simuliertem Sonnenlicht einen ausgeprägten photovoltaischen Effekt. Die Messung der Photoströme bei unterschiedlichen Anregungswellenlängen ergibt für verschiedene Sensibilisatoren unterschiedliche Effizienzen der Ladungsträgererzeugung. Während TiO_2 durch CdSe-QP effektiv sensibilisiert wird, ist dies für CdTe-QP nicht der Fall. Dies wird auf die unterschiedlich starke Lokalisierung der Ladungsträger in den QP zurückgeführt.

Durch eine Variation der Zellstruktur hinsichtlich der Dicken und der Zusammensetzung der einzelnen Schichten wird die Konversionseffizienz optimiert und die Effizienz des Ladungstransports untersucht. Vergleiche mit simulierten Diodenkennlinien ergeben, dass bei den hier untersuchten Zellen eine zu geringe Leitfähigkeit der nanoporösen Schichten die Konversionseffizienz auf 0,02% limitiert.

Acknowledgements

The scientific work presented in this dissertation was carried out under the supervision of PD Dr. Stefan Kirstein in the Physics of Macromolecules Group (PMM) at the Institute of Physics, Humboldt University of Berlin (HU), chaired by Prof. Dr. Jürgen P. Rabe. For the preparation of this manuscript, suggestions from Dr. Helfried Näfe from the Max Planck Institute for Metals Research in Stuttgart were very valuable. Naturally, this work could not have been completed without the continuous help and support from both inside the PMM Group and outside. I would like to thank in particular the people listed below for their contributions.

Institute of Physics, HU

Evi Poblenz (Prof. Rabe Group) was very helpful with solution preparations, substrate cleaning, and other chemical matters. Yingchuan Yu (Prof. Rabe Group) conducted the experiments with polymers in salted solution. Dr. Helmut Dwelk (Prof. Manzke Group) was very supportive with metal vapor deposition, and Dr. Sylke Blumstengel (Prof. Henneberger Group) supported photocurrent action spectrum measurements. Dr. Siegfried Rogaschewski (Prof. Niehus Group) and Dr. Peter Schäfer (Prof. Henneberger Group) took scanning electron microscopy (SEM) images shown in this work.

I would like to thank Steffen Duhm and Hendrik Glowatzki (Dr. Koch Group) for performing all X-ray photoelectron spectroscopy (XPS) measurements described in this work. Dr. Norbert Koch advised me on XPS measurements and analysis and on polymer material choice. He also granted access to his measurement and preparation equipment. I thank all other members of both Prof. Rabe's and Dr. Koch's Group, especially Dr. Nikolai Severin and Jörn-Oliver Vogel, for supporting my work with their expertise and helpful advice.

Collaboration partners

I am grateful to Dr. Akira Fujisawa (Nippon Sheet Glass Research Department, Tokyo) for the donation of fluorine-doped tin oxide coated glass substrates.

Dr. Hans Berlepsch (Institut für Elektronenmikroskopie, Freie Universität Berlin) took the transmission electron microscopy images of TiO_2 nanoparticles.

Prof. Dr. Mingyuan Gao (Chinese Academy of Sciences, Beijing) introduced us to colloidal quantum dots, Dr. Dayang Wang and Dr. Hao Zhang (Max Planck Institute of Colloids and Interfaces, Potsdam) synthesized the quantum dots used in this work.

Virginia Commonwealth University (VCU), Richmond, VA (USA)

Prof. Dr. James T. McLeskey, Jr., encouraged us to use charged polythiophenes for this work and supplied us with materials. I thank Prof. McLeskey for accepting me as a visiting researcher at the Energy Conversion Systems Lab (ECSL) from May to July 2007, and for his generous support and advice.

Joseph Kim (ECSL) conducted profilometer thickness measurements of composite films. Dr. Jim Spivey (Department of Chemistry) supported me with taking SEM images of our samples. I also thank my colleagues and the faculty at the VCU School of Engineering, especially Dr. Hoda Hafez, Prof. Dr. Kam K. Leang, Prof. Dr. Karla M. Mossi, Dr. Mona Saif, Prof. Dr. Curtis R. Taylor, Dr. Tarek M. Trad, Matthew Vaerewyck and Dr. Chunya Wu for inspiring discussions, for helpful support in the lab, and for making my research stay very enjoyable.

Funding sources

This work was funded by a scholarship from the German Research Foundation (DFG) through the Research Training Group 1025 (Graduiertenkolleg 1025) 'Fundamentals and functionality of size and interface controlled materials: spin- and optoelectronics'.

The German Academic Exchange Service (DAAD) supported my research stay at VCU with funding from the 'Kurzstipendien für Doktoranden' program.

Dr. Norbert Koch and his collaborators at H. C. Starck GmbH funded the final stage of this work. I am very grateful for all granted funding, which offered me the opportunity to conduct this research project.

Research Training Group 1025

I would like to thank Prof. Dr. Vlasta Bonačić-Koutecký and Prof. Dr. Wolfgang Nolting for accepting me as a student in the Research Training Group, and for the frequent opportunities to present and discuss my work in seminars and workshops. Prof. Dr. Bonačić-Koutecký supported my application for additional funding for my research stay at VCU. I thank the members of the Research Training Group for lively discussions in the seminars.

Supervisors

I am very grateful to PD Dr. Stefan Kirstein and Prof. Dr. Jürgen P. Rabe for the initiation of this project and for giving me the opportunity to contribute. I thank Prof. Dr. Rabe for admitting me to the Physics of Macromolecules Group, for his permission to use the equipment I needed and for his support and motivation. I am also very thankful for the regular opportunities to present and discuss my work in the group seminars.

Last, but not least, I thank PD Dr. Kirstein for his careful supervision. He was always ready to give me his support in all matters of this project. His experience and his advice guided this work in the right direction at all stages. His support with the preparation of publications and with my application for additional funding was especially useful to me. He also gave me the opportunity to present my work at scientific meetings and established helpful links to collaboration partners.

Abbreviations

The following abbreviations and codes will be used in this dissertation (see page):

A, B, C	sample types (57)
AFM	atomic force microscopy (58)
ASF	atomic sensitivity factor (68)
CB	conduction band (10)
DI	de-ionized (49)
DSSC	dye-sensitized solar cell (31)
EA	electron affinity (100)
EMA	effective mass approximation (37)
EQE	external quantum efficiency (107)
FF	fill factor (20)
FTO	fluorine-doped tin oxide (36)
HOMO	highest occupied molecular orbital (9)
IE	ionization energy (100)
IPCE	internal photon-to-current conversion efficiency (110)
ITO	indium tin oxide (47)
LUMO	lowest unoccupied molecular orbital (9)
NDR	negative differential resistance (90)
PDAC	poly(diallyldimethyl ammonium chloride) (48)
PEI	poly(ethylene imine) (48)
PSS	poly(sodium styrene sulfonate) (48)
PTEBS	poly(2-(3-thienyl)-ethoxy-4-butylsulfonate) (48)
QD	semiconductor quantum dot (37)
RF	roughness factor (74)
Rhod6G	rhodamine 6G (50)
Ru535	ruthenium complex dye (50)
SEM	scanning electron microscopy (58)

TCO	transparent conductive oxide (47)
TEM	transmission electron microscopy (51)
TFB	poly(9,9'-dioctylfluorene-*co*-*N*-(4-butylphenyl)diphenylamine) (48)
TGA	thioglycolic acid (50)
THF	tetrahydrofurane (49)
TOPO	trioctylphosphine oxide (38)
UHV	ultrahigh vacuum (30)
VB	valence band (10)
XPS	X-ray photoelectron spectroscopy (58)

Contents

1 Introduction **1**

1.1 Fossil resources and the global supply of energy 1

1.2 Photovoltaics as a renewable energy source 2

1.3 Nanoengineered photovoltaics 4

1.4 Scope of the present work 6

2 Scientific background **8**

2.1 Outline 8

2.2 Conventional vs. excitonic solar cells 9

2.2.1 Conventional *p*-*n* homojunction cells 9

2.2.2 Excitonic heterojunction cells 22

2.2.3 Consequences for excitonic cell designs 27

2.3 Nanostructured excitonic cell designs 28

2.3.1 Nanostructured organic cells 29

2.3.2 Dye-sensitized solar cells 31

2.3.3 Hybrid organic / inorganic cells 34

2.3.4 Quantum dot photovoltaic cells 37

2.4 Layer-by-layer self-assembly of nanostructured thin films 41

2.4.1 Self-assembly by electrostatic interaction 42

2.4.2 Applications 45

3 Materials and methods **47**

3.1 Materials 47

3.1.1 Sample substrate types 47

3.1.2 Molecules and nanoparticles 48

3.2 Methods 52

3.2.1 Substrate cleaning and compact TiO_2 coatings 52

3.2.2 Layer-by-layer self-assembly 55

3.2.3 Structure characterization 58

3.2.4 Optical and electronic characterization 59

4 Structure of self-assembled TiO_2 / polyion heterofilms **62**
4.1 Outline . . . 62
4.2 Characterization results and discussion . . . 62
4.2.1 Film morphology and thickness . . . 62
4.2.2 Film composition . . . 66
4.2.3 Internal film structure . . . 71
4.3 Summary and conclusions . . . 75

5 TiO_2 / polythiophene thin film devices **77**
5.1 Outline . . . 77
5.2 Device fabrication and electronic structure . . . 78
5.2.1 Electronic material properties . . . 78
5.2.2 Cell fabrication . . . 79
5.3 Results and discussion . . . 83
5.3.1 Film structure . . . 83
5.3.2 Photoelectronic characteristics . . . 86
5.4 Summary and conclusions . . . 96

6 Quantum dot sensitized hybrid photovoltaic devices **98**
6.1 Outline . . . 98
6.2 Device fabrication and electronic structure . . . 98
6.2.1 Material properties . . . 98
6.2.2 Cell fabrication . . . 102
6.3 Results and Discussion . . . 105
6.3.1 Film structure . . . 105
6.3.2 Photovoltaic behaviour . . . 107
6.4 Summary and conclusions . . . 115

7 Conclusions and outlook **117**

Chapter 1

Introduction

1.1 Fossil resources and the global supply of energy

The economies of developed countries have been dependent on the consumption of fossil fuels ever since the beginning of the industrialization in the late 18th century, when fossil coal replaced timber as the prime source of energy for steel production [1]. In 2004, coal, petroleum, and natural gas still accounted for 80% of the global supply of primary energy. The economic development in the industrialized and especially in the developing countries is expected to increase the demand for primary energy further in the coming decades, since efficiency improvements in the use of energy will not be a sufficient compensation [2]. It is desirable for both economic and environmental reasons that alternative non-fossil sources of energy will be available to meet the future demand.

Fossil resources of energy are limited. The most economic reservoirs are depleting and more costly ones have to be exploited, ending the abundance of cheap primary energy that has been driving the industrialization process [3]. If the future supply of primary energy still relies on fossil fuels, then the inevitable price increase of this resource will seriously affect the economic system of the industrialized world [4]. Also, energy supply is a crucial issue for the development and the reduction of poverty in agricultural societies in, e.g., sub-Saharan Africa, that cannot be solved with centralized systems based on fossil fuel powered plants and wide area power grids [5]. Low population densities and scarce natural resources make decentralized, environmentally friendly, and economic sources of energy a necessity.

Furthermore, the release of carbon dioxide from fossil fuel combustion into the atmosphere is today accepted as the primary cause of the global warming trend observed

over the last decades [6, 7], as well as of an increase of ocean acidity threatening life in the largest natural habitat and food source [8, 9]. An effective protection of the global climate and of the agricultural resources and water supplies of the earth will require a dramatic reduction of the consumption of fossil fuels. As a substitute for fossil fuels, sustainable energy supplies with a closed carbon cycle or free of CO_2 emission have to be introduced on a large scale.

1.2 Photovoltaics as a renewable energy source

Under the impression of environmental and economic challenges, sustainable means of energy supply have been developed. They include hydroelectric, ocean wave, tidal, wind, solar thermal, photovoltaic, biomass and geothermal power generation [10].

With the exception of geothermal and tidal power, all sustainable energy sources are fueled by solar radiation, which is by far the most abundant primary source of renewable energy [10]. Photovoltaic power generation, based on the 'photovoltaic effect' discovered by the French physicist Alexandre Edmond Becquerel in 1839 [11], stands out from all available harvesting technologies. It directly converts solar radiation into electricity, which can be transported and converted into all other forms of energy efficiently. It can be used on a very small scale in most parts of the earth, since sufficient solar radiation to drive solar cells is available basically everywhere on the globe.

Photovoltaic technology has the potential to play an important role in the energy mix of the future and is well suited for both decentralized and centralized application. The power generation process requires no fuel supply and is essentially free of CO_2 emissions. These advantages of photovoltaic power generation and the urgent need for clean energy, however, contrast sharply with its current contribution to the energy supply. In 2004, the photovoltaics share in the global mix of primary energy was below 0.01%, far behind other renewable energy sources like hydroelectric or wind power. In Germany, where 70% of the total European photovoltaic power is installed, the share had just passed 0.02% [12].

The reason for the low acceptance is the high unit cost of the market dominating silicon solar cells, which were invented in 1954 [13]. Figure 1.1 shows an array of photovoltaic modules containing this type of cells. As of 2002, bulk Si accounted for 93% and amorphous thin film Si for another 5% of production worldwide, with the best modules based on bulk Si reaching power conversion efficiencies of 13–15% [14]. The potential for cost reduction of efficient cells appears to be limited, since the main driver

is the expensive and highly energy consuming production of raw Si [15]. The payback period for generating the energy that was initially consumed in the production process is three to five years depending on geographic latitude [16]. The specific production cost per peak output power was estimated to be 5100 €/kW_p in 2004 [12], making the cost of solar electricity in Germany ten times higher than from conventional sources [17]. Consequently, cost reduction of photovoltaic power generation is a critical issue if application on a larger scale shall be achieved.

Figure 1.1: Array of solar panels (La Réunion, Pacific Ocean). Image taken from [18].

Of course, a reasonable application also requires high conversion efficiencies, since these determine the size of the area that is necessary for the production of a given amount of electrical power. The power conversion efficiency η is defined as the ratio between the maximum electrical power output $P_{\mathrm{el}}^{\mathrm{max}}$ and the total solar radiative power incident on the cell surface P_{rad}:

$$\eta = \frac{P_{\mathrm{el}}^{\mathrm{max}}}{P_{\mathrm{rad}}} \tag{1.1}$$

The area $A(\eta)$ necessary for the production of P_{el} is given by

$$A(\eta) = k\,\frac{P_{\mathrm{el}}}{\eta}, \tag{1.2}$$

where $k = P_{\mathrm{rad}}/A$ is the radiation intensity. Since area is generally scarce in populated regions of the world, high efficiencies are critical for economic application. Figure 1.2 illustrates that very large areas need to be devoted to solar power generation in order to contribute to a country's consumption of energy significantly. The yellow square represents an area of 25,921 km^2 which would need to be used for a solar power plant with $\eta = 10\%$ to cover the annual energy consumption of the USA in 1999, an enormous area even for a country with low population density [10]. With current 13% efficient Si cells, the actual plant area would need to be much larger since additional space is necessary for module access and maintenance.

Figure 1.2: Photovoltaic energy farm covering an area of 25,921 km^2 (yellow square). Taken from [10].

1.3 Nanoengineered photovoltaics

A number of different solar cell concepts has been developed so far to meet the requirements of high efficiency and low cost. They can generally be classified in three generations along the lines of materials and designs used. The graph in Fig. 1.3 characterizes these cell generations in terms of production cost, conversion efficiency, and electricity price.

First generation photovoltaic systems are based on bulk semiconductor crystals of very high quality. Important device types are gallium arsenide cells used in space applications and the silicon cells mentioned above. These devices are characterized by high efficiencies and high production cost. Especially Si cells, which have been studied in detail and are commercially the most successful concept, are the benchmark system for new photovoltaics concepts. Therefore, their structure and conversion mechanism will be addressed in Section 2.2.

Second generation solar cell designs are driven by the attempt to lower the material cost by using thin films with high absorption cross sections as active layers. Prominent examples include cells based on amorphous Si [20], Cu(In,Ga)Se_2 [21], and CdTe [22]. All these concepts have reached competitive efficiencies and have recently been introduced to commercial application.

Third generation photovoltaics comprises several new approaches to fabricate cells from new materials, in particular organic [23, 24] and nanocrystalline materials [25], that have the potential for low cost production. These concepts require an engineering of

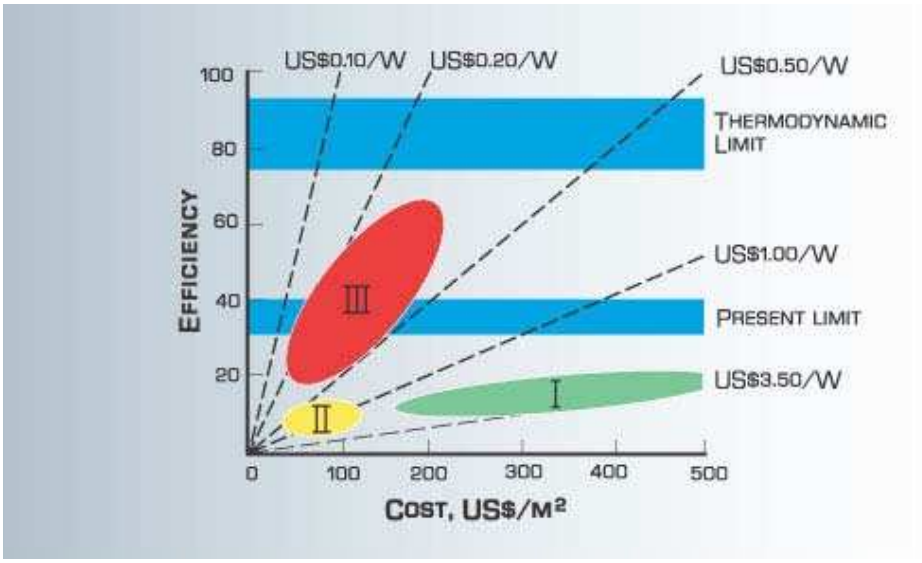

Figure 1.3: Three generations of solar cells (green, yellow and red areas labeled by I, II, and III) characterized by the production cost/area in USD/m^2 (x axis) and efficiency (y axis). Dashed lines indicate different price levels per watt output power. Taken from [19].

cell materials on the scale of nanometers in order to obtain tailored absorber properties [26] and cell structures [27].

The general idea of third generation concepts can be described as using different materials for the different tasks required for photovoltaic energy conversion, in contrast to, e.g., Si cells. With this approach, material properties can be tailored individually to fit one specific task. Furthermore, the combination of materials yields interface effects which can also be adjusted and utilized for conversion processes, typically for charge separation [28–30]. These functionalities open up new perspectives for cell design and reachable conversion efficiencies. For example, if one uses very small semiconductor crystals called 'quantum dots' as absorbers, one can exploit the recently reported multiplication of photogenerated charge carriers for increased efficiencies [31–33]. In principle, as indicated in Fig. 1.3, this effect allows for efficiencies beyond the fundamental single-junction limit of 31% [34], which are otherwise only achievable by using expensive multilayer systems [35, 36].

Examples of third generation cells include hybrid organic / inorganic cells [37], purely organic cells [29], dye-sensitized cells [28], and quantum dot cells [26]. Several concepts, in particular organic cells, are expected to reach the stage of commercial applicability soon. Nevertheless, many important issues concerning the choice of materials, the cell processing, and the relations between structure and function of third generation cells remain open and require further basic research into the field.

The large variety of available organic and inorganic cell components raises the question of which materials are best suited and how they can be optimized for photovoltaic power conversion. The interfaces formed between materials and the cell structure play a crucial role for the efficiency, but the exact criteria for efficient structures remain subject to debate and need to be clarified for the development of better cell designs.

The realization of novel designs and the use of tailored materials also require advanced fabrication methods which allow the handling of the developed substances and a precise control of the cell structure on the nanometer scale, as we will explain in the following chapter. The research presented in this dissertation focuses on a recently introduced thin film fabrication method, which offers the required structure control and the opportunity to combine a range of materials with useful optical and electronic properties. The aim of our work is the production of new cell types and an analysis of the influence of the cell structure on performance.

1.4 Scope of the present work

The present work is dedicated to new photovoltaic cell types belonging to the third cell generation described above. We were not only looking for high conversion efficiencies, but also for long term device stability under realistic conditions. Therefore, we focus on photostable materials and solid state device concepts.

Our cell design is based on reports of hybrid cells consisting of polymers and inorganic nanoparticles, which showed high stability in ambient conditions as well as convenient processing of the constituent materials [38, 39]. Other reports describing the unique properties of quantum dots as light absorbers [30, 31] encouraged us to include these particles in our hybrid cell design.

The recently introduced layer-by-layer self-assembly, a solution based method to grow hybrid organic/inorganic thin films, provides structure control for the integration of light-absorbing and semiconducting materials on the scale of nanometers, which is necessary for the fabrication of efficient cell structures, as mentioned above [40, 41]. As reported in the literature, the process has already been used to fabricate nanostructured titanium dioxide electrodes for dye-sensitized solar cells [42, 43].

We extend the range of materials that can be handled with the layer-by-layer self-assembly process to quantum dots and light-absorbing polymers. For the first time, nanostructured thin films containing both light-absorbers and charge transport materials are fabricated with this method and used as active layers in hybrid photovoltaic cells.

We analyze the film structures and properties on the one hand and cell performances on the other hand, so that conclusions with respect to the relevant structure-property relationships can be drawn.

In Chapter 2, the concepts of photovoltaic energy conversion and the method of layer-by-layer self-assembly will be presented as an introduction to the scientific background of the field. The operating principle of heterojunction devices will be discussed in detail and compared to Si based *p*-*n* homojunction devices, in order to highlight the differences in material requirements and cell structure. Further, we will explain the mechanism of the electrostatic layer-by-layer self-assembly process and its applicability to building hybrid nanostructures.

Chapter 3 describes the organic and inorganic materials and the experimental methods we employed for the manufacture and for the analysis of hybrid photovoltaic cells. The subsequent Chapters 4, 5, and 6 contain the results of structural and electronic characterization experiments of our devices. Chapter 4 reports on structural analyses of different types of composite thin films which were grown layer by layer from titanium dioxide nanoparticles and polymers. These films were used as a basis for two types of hybrid photovoltaic devices. The first type is based on TiO_2 nanoparticle films sensitized with light-absorbing polymers. Structural and electronic analyses which describe the relationship between structure and performance of these devices are the subject of Chapter 5. The second type of devices contains quantum dots as light absorbers. It is characterized by experiments described in Chapter 6, with a focus on structure-property relations and also on absorber functionality. Finally, Chapter 7 presents conclusions from the achieved cell characteristics with respect to the potential of the employed cell designs and fabrication methods.

Chapter 2

Scientific background

2.1 Outline

This chapter introduces the operating principle of photovoltaic cells, and the concept of electrostatic layer-by-layer self-assembly, the method we used to fabricate such devices.

In Section 2.2, we will compare conventional *p*-*n* homojunction devices with excitonic heterojunction devices. The differences between the concepts will be explained and theoretical models describing the cell operation will be presented. Conclusions with respect to the structural requirements for efficient excitonic cells, which are in the focus of this work, will be drawn.

Section 2.3 presents several types of nanostructured cell designs which have been developed to meet the structural requirements for excitonic cells during recent years, including organic cells, dye sensitized, hybrid organic / inorganic, and quantum dot sensitized cells. The latter three types will be in the focus of the experiments and results presented in the subsequent chapters.

Layer-by-layer self-assembly, the method used in this work for the fabrication of nanostructured organic / inorganic electrodes for excitonic cells, is described in Section 2.4. The potential of the method for producing efficient and stable excitonic photovoltaic cells is highlighted.

2.2 Conventional vs. excitonic solar cells

We use the term 'conventional' to refer to photovoltaic cells which separate charges at a *p*-*n* homojunction, because this cell type includes Si cells which have been dominating solar cell research for decades. A *p*-*n* homojunction is an interface between two semiconductors with the same band gap energy, but different doping levels. The migration of free charge carriers across that interface leads to electron-hole recombination and to the formation of a space charge layer, which induces an electric field and a bending of the semiconductor bands. Photogenerated excitons in these systems are only weakly bound, so that they can be separated by the electric field created by the space charges.

The term 'excitonic cells', on the other hand, is used for devices where photogenerated excitons are tightly bound so that they require a heterojunction, i.e., an interface between semiconductors with different energy gaps, for separation [44]. Significant band bending is usually not observed, since the density of free charge carriers is small. The devices discussed in the experimental part of this work are all excitonic cells. In the Section 2.2.2, general features of this cell design such as the band structure, the cell operation and the resulting current / voltage characteristics will be discussed.

Both conventional and excitonic photovoltaic device types have in common that incident photons are converted into an electric current in three basic steps. In the first step, one bound electron / hole pair, called exciton, is created by the absorption of one photon with an energy higher than a certain minimum energy required by the absorber material. This threshold energy is defined by the band gap in semiconductors and by the gap between the highest occupied (HOMO) and the lowest unoccupied molecular orbital (LUMO) in molecules. In the second step, the exciton is separated into a free electron and a free hole. The third step is the transport of the free electrons and holes through the device and their collection at the anode and the cathode, respectively. The individual processes are distinct in conventional and excitonic cells and will be the subject of the following Sections 2.2.1 on *p*-*n* homojunction cells and 2.2.2 on excitonic cells.

2.2.1 Conventional *p*-*n* homojunction cells

In this section, we describe the structure of a *p*-*n* homojunction, the operating principle of homojunction cells and the results of theoretical calculations of the current / voltage behaviour. For the latter, we largely follow the treatment given by Sze [45]. The relevant quantities to describe and compare cell efficiencies will be introduced. These quantities and the results of the calculations will be useful in the interpretation of our

experimental results concerning excitonic cells, presented in the Chapters 5 and 6.

The *p*-*n* junction

Since crystalline Si is a typical semiconductor, the energetic distribution of electronic states is characterized by an energy region with a vanishing density of states, called the band gap, which separates a band with predominantly occupied states, the valence band (VB), from a band with mostly unoccupied states, the conduction band (CB).

The equilibrium distribution of electrons over the available states at a temperature T is described by the Fermi-Dirac distribution which gives the occupation number $F(E)$ of an electronic state with an energy E:

$$F(E) = \frac{1}{1 + \exp\left(\frac{E-E_F}{kT}\right)} \tag{2.1}$$

At room temperature, $kT \approx 25\,\mathrm{meV}$, where k is Boltzmann's constant. The Fermi energy E_F is the energy where an electronic state has the occupation number 1/2. Its position in an intrinsic, i.e., undoped, semiconductor is close to the middle of the band gap, and will be specified for the doped case below. The total concentration of free electrons n is given by

$$n = \int_{\mathrm{CB}} N(E)F(E)dE, \tag{2.2}$$

where $N(E)$ is the density of electronic states, which follows

$$N(E) \propto (E - E_{\mathrm{CB}})^{1/2} \tag{2.3}$$

close to E_{CB}, the minimum of the CB. In the Boltzmann limit, when the distance between E_{CB} and E_F is several kT, the integration in equation (2.2) yields

$$n = N_{\mathrm{CB}} \exp\left(-\frac{E_{\mathrm{CB}} - E_F}{kT}\right), \tag{2.4}$$

where N_{CB}, called the effective density of states in the CB, is proportional to $(kT)^{3/2}$ since with rising temperature, the tails of the Fermi-Dirac distribution reach deeper into the CB so that more CB states are effectively accessible. One obtains equivalent relations for the hole concentration p and the effective density of states N_{VB} in the VB. Since the position of E_F determines the number of both electrons and holes, it is defined by the condition of charge neutrality in a semiconductor crystal. In an intrinsic semiconductor, $n_i = p_i$, where n_i and p_i are n and p in the intrinsic case.

The intrinsic charge carrier density of Si crystals can be changed by many orders of magnitude by doping the crystal lattice with impurities in relative concentrations from 10^{-8} to 10^{-5}. When phosphorus atoms, which have five valence electrons, are incorporated into the Si diamond structure as donors in a spatial concentration of N_{D}, they each release one electron to the CB. This process called n-doping creates free electrons in a concentration n, which is close to the donor density at room temperature [45]:

$$n \approx N_{\mathrm{D}} \tag{2.5}$$

The thermal excitation and annihilation reactions of electrons and holes bring about that the following law of mass action holds for their concentrations:

$$np = n_i p_i = N_{\mathrm{CB}} N_{\mathrm{VB}} \exp\left(-\frac{E_{\mathrm{gap}}}{kT}\right) \tag{2.6}$$

It states that np is a constant independent of the doping level, which is equal to the product of the carrier concentrations n_i and p_i in the intrinsic case. Since $n_i = p_i$, the density of free holes p in the n-doping case is approximately

$$p \approx n_i^2 / N_{\mathrm{D}}. \tag{2.7}$$

Boron atoms, with three valence electrons, act as electron acceptors and withdraw one electron from the VB, which is called p-doping. The resulting density of free holes p is then close to the concentration of acceptors N_{A}:

$$p \approx N_{\mathrm{A}} \tag{2.8}$$

The generated charge carriers can move freely through the crystal, leaving behind one immobile lattice impurity of opposite charge [45–47]. Figure 2.1 shows a schematic representation of two Si crystals, one n-doped and one p-doped.

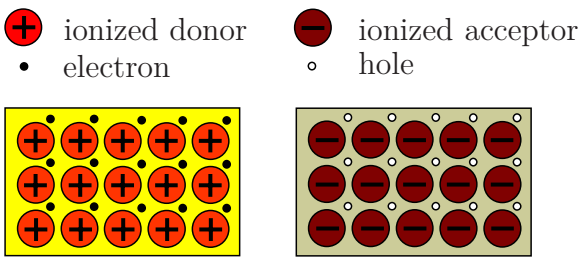

Figure 2.1: Mobile charges and lattice impurities created by n-doping (left) and p-doping (right).

For intrinsic Si, E_F is close to the middle of the band gap. When the crystal is doped by donors or acceptors, the condition of charge neutrality becomes

$$n + N_\mathrm{A} = p + N_\mathrm{D} \tag{2.9}$$

and hence the position of E_F changes. The band structure of available states remains unchanged, and the occupation by charge carriers is still determined by the Fermi-Dirac equation (2.1). The Fermi energy E_F is raised by n-doping and lowered by p-doping. In the Boltzmann limit, one obtains for the position of the Fermi level in the n-doping case

$$E_\mathrm{CB} - E_F = kT \ln\left(\frac{N_\mathrm{CB}}{N_\mathrm{D}}\right), \tag{2.10}$$

and in the p-doping case [45, 47, 48]

$$E_F - E_\mathrm{VB} = kT \ln\left(\frac{N_\mathrm{VB}}{N_\mathrm{A}}\right). \tag{2.11}$$

Figure 2.2 displays the situation for two oppositely doped Si crystals with E_F shifted, but remaining within the band gap.

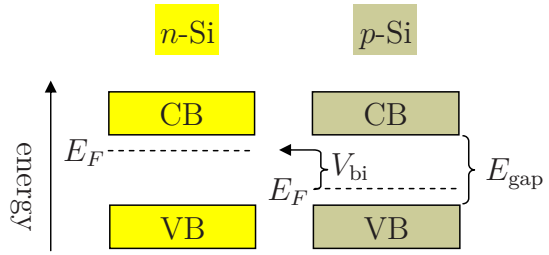

Figure 2.2: Energy level structure of an n-doped (left) and a p-doped Si crystal (right) relative to a uniform vacuum level (not shown). CB: conduction band, VB: valence band, E_F: Fermi energy, E_gap: band gap energy, V_bi: built-in voltage.

If n-doped and p-doped Si crystals are brought into contact, the free electrons and holes will diffuse across the interface, while the ionized impurities remain fixed at their positions in the crystal lattice. Mutual annihilation of electrons and holes by recombination creates a depletion zone without any mobile charges around the interface, reaching the distance x_n into the n-type region and x_p into the p-type region. Since the net charge created on either side is equal, the extensions satisfy

$$N_\mathrm{D} x_n = N_\mathrm{A} x_p. \tag{2.12}$$

The net charges of ionized impurities on both sides of the interface form a space charge

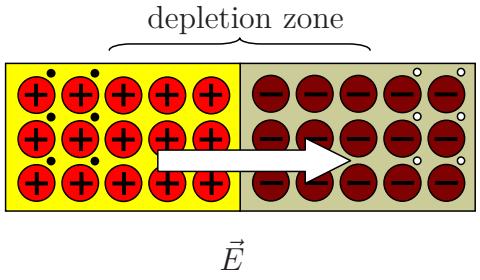

Figure 2.3: Space charge region and electric field $\vec{E}$ of a p-n homojunction.

layer described by the charge density ϱ. An electric field $\vec{E}$ in the interface area described by Gauss' law

$$\vec{\nabla} \cdot \vec{E} = \varrho/\varepsilon \tag{2.13}$$

emerges, as depicted in Fig. 2.3. Here, ϱ is the space charge density, $\vec{\nabla}$ is the nabla operator, and ε is the dielectric constant of the material.

Electron and hole currents $\vec{I}_n$ and $\vec{I}_p$ now consist of drift currents caused by the electric field and diffusive currents driven by density gradients: [45, 47, 48].

$$\vec{I}_n = q\mu_n n\vec{E} + qD_n\vec{\nabla}n \tag{2.14}$$

$$\vec{I}_p = q\mu_n p\vec{E} - qD_p\vec{\nabla}p \tag{2.15}$$

Here, q is the elementary charge, and μ_n, D_n, μ_p and D_p are the mobilities and diffusion constants of electrons and holes, respectively. They are connected by the Einstein relation for electrons

$$D_n = \left(\frac{kT}{q}\right)\mu_n, \tag{2.16}$$

and an equivalent relation for holes. One finds that the currents follow the gradient of the Fermi level, according to

$$\vec{I}_n = \mu_n n\vec{\nabla}E_F \tag{2.17}$$

and an analogue for holes. In equilibrium, $\vec{I}_n$ and $\vec{I}_p$ vanish, the drift and diffusion currents are balanced, and E_F is uniform throughout the device. The Fermi levels on both sides of the junction, which were at different positions relative to the band levels before contact was made, see Fig. 2.2, are aligned. Since the recombination of carriers only affects the interface area, outside of the depletion zone the distribution remains unchanged and the position of E_F relative to CB and VB is given by the equations (2.10) and (2.11) [45, 47]. The resulting situation in the device is shown in Fig. 2.4: E_F is now uniform, and its position relative to CB and VB outside of the depletion zone is

the same as in Fig. 2.2.

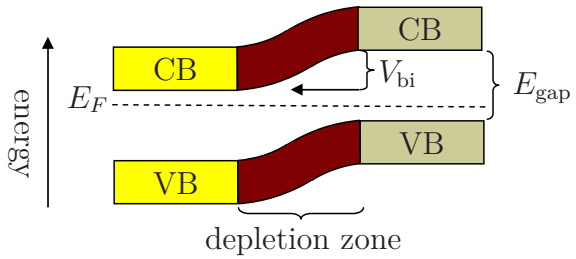

Figure 2.4: Band structure and Fermi level E_F of a p-n homojunction.

Accordingly, both the VB and the CB are bent inside the depletion zone. The band bending is given by the definition of an electrostatic potential Φ [45, 47, 48]:

$$\vec{E} = -\vec{\nabla}\Phi \tag{2.18}$$

Using the equations (2.13) and (2.18), one obtains the Poisson equation

$$\Delta V = -\frac{\varrho}{\varepsilon}, \quad \text{where } \Delta = \nabla^2. \tag{2.19}$$

We examine the one-dimensional case where the x-direction is the normal of the interface plane. In the approximation of an abrupt junction, the charge density is created by ionized impurity atoms, so that $\varrho = qN_{\mathrm{D}}$ or $\varrho = -qN_{\mathrm{A}}$ inside the depletion zone, and $\varrho = 0$ outside the depletion zone. One obtains for the n-doped region of the depletion zone

$$-\frac{\partial^2 V}{\partial x^2} = \frac{q}{\varepsilon} N_{\mathrm{D}}, \tag{2.20}$$

for the p-type region of the depletion zone

$$-\frac{\partial^2 V}{\partial x^2} = \frac{-q}{\varepsilon} N_{\mathrm{A}}, \tag{2.21}$$

and $\partial^2 V/\partial x^2 = 0$ outside of the depletion zone.

Integration yields the following relation between the total width of the depletion layer and the total band offset called the built-in voltage V_{bi}:

$$x_p + x_n = \sqrt{\frac{2\varepsilon}{q}\left(\frac{N_{\mathrm{A}} + N_{\mathrm{D}}}{N_{\mathrm{A}} N_{\mathrm{D}}}\right) V_{\mathrm{bi}}} \tag{2.22}$$

V_{bi}, as displayed in the Figs. 2.2 and 2.4, is defined as the difference of the Fermi levels

given by the equations (2.10) and (2.11). One obtains

$$V_{\mathrm{bi}} = \frac{kT}{q} \ln\left(\frac{N_{\mathrm{A}} N_{\mathrm{D}}}{n_i^2}\right). \tag{2.23}$$

From the relations (2.22) and (2.23), the total width of the depletion layer can be calculated. For typical doping levels, one obtains widths on the order of 1 μm [46].

Cell operation

An interface with the band structure described above is called a p-n junction. The electric field present in the space charge region drives positive and negative charges in opposite directions. In equilibrium, as mentioned before, the resulting drift currents are balanced by diffusion currents.

When photons with energies equal to or larger than the band gap energy E_{gap} enter the device, excitons are created both inside the space charge layer and outside, as displayed in Fig. 2.5. Owing to the large dielectric constant ε of Si, these excitons are only weakly bound, so that the electric field inside the space charge region is sufficient to separate them into electrons and holes.

Excitons created outside the space charge region can reach it by diffusion, if their diffusion length is long enough. The diffusion length is determined by the quality and purity of the crystal, because recombination of the excitons is greatly enhanced at grain boundaries and other defects. In crystalline Si cells with a very low defect concentration, generally all excitons reach the space charge layer [48], where they are separated into free electrons and holes by the electric field.

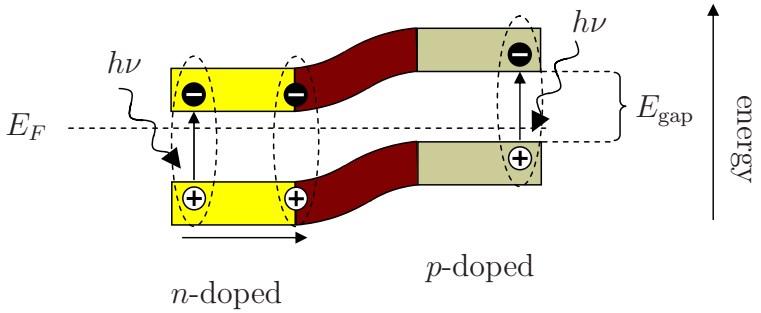

Figure 2.5: Exciton generation by photon absorption. E_F is the equilibrium Fermi level in the dark.

When the exciton has been split, the free electrons and holes are affected individually by the electric field. They are driven out of the space charge region in opposite directions,

so that they accumulate in the n-doped and the p-doped region, respectively. During illumination, or when the device is biased by an external voltage, the density of charge carriers is no longer in equilibrium and a uniform E_F does not exist any more. New electron and hole densities n and p establish in the two doping regions. One defines two different 'quasi-Fermi levels' E_{Fn} and E_{Fp} which would give the new density of electrons and holes, respectively, according to equation (2.4) and the corresponding relation for holes. Non-vanishing electron and hole currents result, which are, in analogy to equation (2.17), described by

$$I_n = \mu_n n \frac{\partial}{\partial x} E_{Fn} \text{ and} \tag{2.24}$$

$$I_p = \mu_p p \frac{\partial}{\partial x} E_{Fp}. \tag{2.25}$$

When both doping regions are connected through an external load, the drift currents of separated electrons and holes will not be balanced by an internal diffusion current, but drive an external current instead. The difference between the quasi-Fermi levels E_{Fn} in the n-type region and E_{Fp} in the p-type region is the operating voltage V of the device,

$$V = \frac{E_{Fp} - E_{Fn}}{q} \tag{2.26}$$

as shown in Fig. 2.6 [45]. Owing to the band bending, V is smaller than E_{gap}/q. The external current $I(V)$ is determined by both the light intensity and the I/V characteristics of the p-n junction described by the Shockley equation discussed below. Hence, this mechanism converts absorbed photon energy into electric power given by $P_{\text{el}} = -VI$.

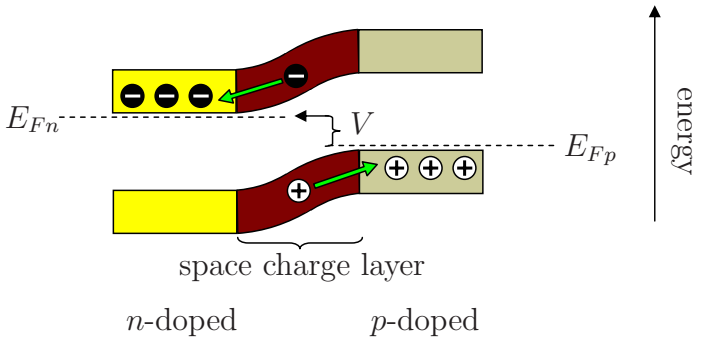

Figure 2.6: Separation of the quasi-Fermi levels E_{Fn} and E_{Fp} caused by carrier accumulation.

I / V characteristics

Taking into account continuity equations for the charges

$$\frac{\partial n}{\partial t} = -\beta + \frac{1}{q}\frac{\partial}{\partial x} I, \tag{2.27}$$

where β is the recombination rate of electrons and holes, the external current $I(V)$ of a device in the dark can be calculated from the relations (2.24), (2.25), and (2.26). It is the sum of electron and hole currents, which dominate in the n-type and the p-type region, respectively. One obtains the Shockley diode equation

$$I(V) = I_p + I_n = I_0 \left[\exp\left(\frac{qV}{kT}\right) - 1\right], \tag{2.28}$$

which describes a strongly rectifying behaviour. I_0 is the saturation current for large negative voltages. The equation is in good agreement with experimental results, as long as the devices do not show photogeneration of charge carriers [45]. For light-sensitive diodes, a diode ideality factor n is introduced into the exponential term of that equation to achieve better fits of calculated curves to experimental data [49]. It usually takes values between 1 and 2, with 1 being the ideal case of equation (2.28) [45, 47, 50]:

$$I(V) = I_0 \left[\exp\left(\frac{qV}{nkT}\right) - 1\right] \tag{2.29}$$

Real conventional solar cells can be modeled by the equivalent circuit shown in Fig. 2.7. It consists of a photocurrent source I_{ph}, which delivers a current independent of the applied voltage, but depending on the illumination intensity, in parallel to a diode described by the equation (2.29). Further, a shunt resistance R_{sh} in parallel to the diode and a serial resistance R_{s} are added to describe the real behaviour of the device. The ideal values for the resistances in terms of device performance would be $R_{\mathrm{s}} = 0$ and $R_{\mathrm{sh}} = \infty$ [51, 52]. One obtains the following relationship between $I(V)$ and V:

$$I(V) = I_0 \left\{\exp\left[\frac{q}{nkT}\left(V - I(V)R_{\mathrm{s}}\right)\right] - 1\right\} + \frac{V - I(V)R_{\mathrm{s}}}{R_{\mathrm{sh}}} - I_{\mathrm{ph}} \tag{2.30}$$

Analytically, only ideal cases of equation (2.30) when $R_{\mathrm{s}} = 0$ or $R_{\mathrm{sh}} = \infty$ can be solved for either $I(V)$ or V. The general case can be solved numerically using mathematical software. E.g., the package MATHEMATICA gives a solution for $I(V)$ in closed form using the numerical solutions to the transcendental equation $z = w\exp(w)$, contained in the function `ProductLog`.

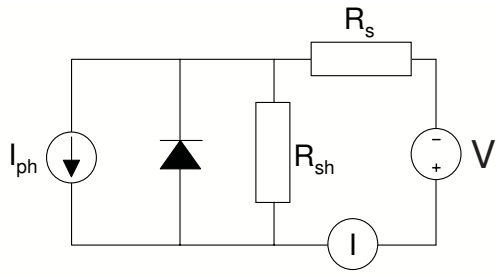

Figure 2.7: Equivalent circuit of a real solar cell [24, 52].

In order to give an impression of the influence of the individual parameters shown in Fig. 2.7 on the device behaviour, we simulated I/V curves for different values of the photocurrent I_{ph}, the serial resistance R_{s}, and the shunt resistance R_{sh}. We used the closed solution of equation (2.30) and kept the diode parameters I_0 and n fixed. Variations of the diode parameters showed that they determine the shape of the I/V curve, namely the voltage where the current slope increases, i.e., the on-voltage, and the width of the transition region. The variation of these diode parameters is not shown in Fig. 2.8, where we focus on the effects of the other circuit components. The figure displays a series of graphs, each for a different level of the photocurrent I_{ph}, with I/V curves calculated for various values of the internal resistances R_{s} and R_{sh}.

The solid curves in Fig. 2.8 were simulated to represent a laboratory cell with nearly ideal properties in terms of the resistances, with a low serial resistance of $R_{\mathrm{s}} = 0.5\,\Omega\mathrm{cm}^2$ and a high shunt resistance of $R_{\mathrm{sh}} = 1\,\mathrm{M}\Omega\mathrm{cm}^2$ [48]. The other curves were simulated with non-ideal resistances, namely a higher serial resistance of $R_{\mathrm{s}} = 3\,\mathrm{k}\Omega\mathrm{cm}^2$ (short dashed), a lower shunt resistance of $R_{\mathrm{sh}} = 25\,\mathrm{k}\Omega\mathrm{cm}^2$ (long dashed), or both (dot-dashed). We display simulations with different levels of photocurrents I_{ph} because the influence of the resistance on the curve shape depends on the relative magnitude of the resistances and I_{ph}. Note the different current scales in Fig. 2.8.

For the lowest photocurrent level of $I_{\mathrm{ph}} = 0.06\,\mathrm{mA/cm}^2$ (top image in Fig. 2.8), the respective effects of R_{s} and R_{sh} on the I/V curve shape are obvious. R_{s} determines the curve slope in forward bias, when the largest part of the voltage drops across the serial resistance. Low values of R_{sh} create a slope in the region of zero voltage, where voltage changes do not affect the diode current, but the current through the parallel shunt resistance. Both resistance values can be estimated from measured curve slopes directly. The parameter I_{ph} determines the current offset for $V = 0$.

The current at $V = 0$ is slightly reduced compared to the ideal case (solid curve), when R_{s} is increased and R_{sh} decreased (dot-dashed curve). This effect becomes most pronounced for higher photocurrents of $I_{\mathrm{ph}} = 0.6\,\mathrm{mA/cm}^2$ and $I_{\mathrm{ph}} = 6\,\mathrm{mA/cm}^2$ (middle

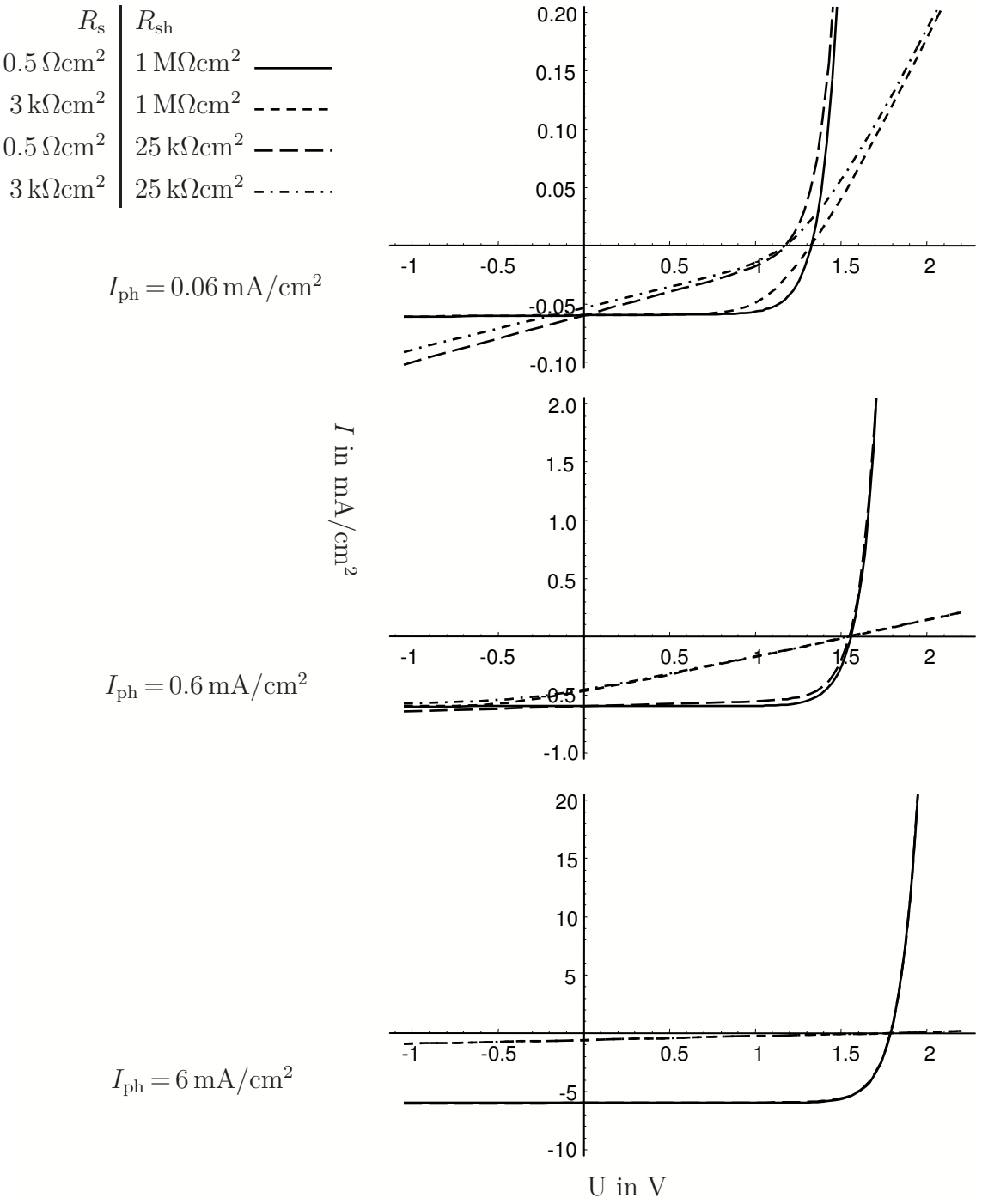

Figure 2.8: I/V curves simulated with different parameters. The serial resistances R_s determine the curve slope in forward bias, and the shunt resistances R_{sh} determine it close to $V = 0$. See text for details on the influence of the photocurrents I_{ph}.

and bottom image in Fig. 2.8), where the same pairs of the resistance values were used. It is apparently the value of R_{s} which dominates the behaviour of the cells, reducing the current for zero voltage by almost one order of magnitude in the bottom image (short dashed and dot-dashed lines). A decrease in R_{sh} (long dashed line), which yielded a recognizable effect for low photocurrents, only influences the curve shapes of higher currents to a minor degree.

Electric power output

The electric power output P_{el} of a power generating device connected to an external load is given by the product $P_{\mathrm{el}} = -VI$, where $-V$ is the voltage dropping across the load, and I is the current flowing through it. The maximum electric power output $P_{\mathrm{el}}^{\mathrm{max}}$ of photovoltaic cells depends on the shape and position of the I/V curve. Geometrically, $P_{\mathrm{el}}^{\mathrm{max}} = (-VI)^{\mathrm{max}}$ corresponds to the largest rectangle that can be fitted between the origin and the curve in the range of negative current and positive voltage, see Fig. 2.14 for an example. In order to characterize the I/V curve and hence the performance of the cells, one uses the following three quantities: The open circuit voltage or photovoltage U_{oc}, the short circuit current I_{sc}, called photocurrent in the following, and the fill factor FF. The photovoltage and photocurrent are given by the position of the I/V curve and are defined by the following equations:

$$I_{\mathrm{sc}} = -I(V=0) \tag{2.31}$$

$$I(U_{\mathrm{oc}}) = 0 \tag{2.32}$$

The FF describes the shape of the I/V curve and is defined as the following ratio:

$$\mathrm{FF} = \frac{P_{\mathrm{el}}^{\mathrm{max}}}{I_{\mathrm{sc}} U_{\mathrm{oc}}} \tag{2.33}$$

Here, $I_{\mathrm{sc}}U_{\mathrm{oc}}$ is geometrically the area of the rectangle formed by the origin and I_{sc} and U_{oc} on their respective scales. $P_{\mathrm{el}}^{\mathrm{max}}$ is the area of the largest rectangle fitting between the origin and the curve, as described above. Therefore, the more concave the I/V curve is to the origin, the higher are the FF and the power output. Using the equations (1.1) and (2.33), the power conversion efficiency of a photovoltaic cell can be written as

$$\eta = \frac{I_{\mathrm{sc}} U_{\mathrm{oc}} \mathrm{FF}}{P_{\mathrm{rad}}}, \tag{2.34}$$

where P_{rad} is the radiative power incident on the cell surface.

When a non-monochromatic light source such as sunlight is used, two important loss mechanisms limit the conversion efficiency η. Photons with an energy $h\nu < E_{\mathrm{gap}}$ do not create excitons and are lost. Photons with an energy $h\nu > E_{\mathrm{gap}}$, on the other hand, create 'hot' excitons with excess kinetic energy. In bulk materials, these hot excitons quickly thermalize towards the band edges, so that the excess energy is lost as heat. The magnitudes of these two losses depend on the band gap energy, but they cannot be minimized simultaneously if a device with a single junction is used. Moving the band gap to lower energies will reduce the losses on the low energy side, but increase thermalization losses, and vice versa. Figure 2.9 illustrates this situation. It results in an upper limit for the conversion efficiency of solar power of $\eta = 31\%$ for conventional single junction cells, which has been derived from thermodynamic principles by Shockley and Queisser [34]. The perspective to overcome this limit by using semiconductor quantum dots as absorbers will be discussed in Section 2.3.4 [33].

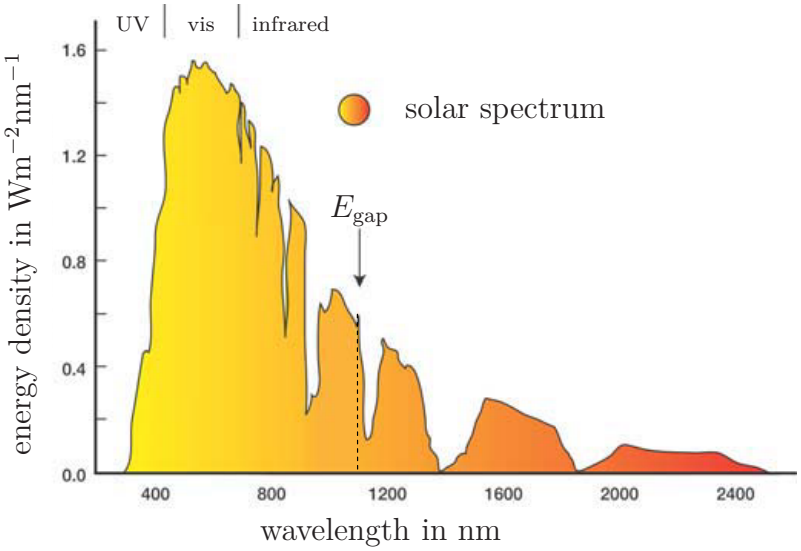

Figure 2.9: Spectral energy density of solar radiation at the surface of the earth. Dashed line: band gap energy E_{gap} of an absorber separating the solar spectrum into a high energy (short wavelengths) and a low energy (long wavelengths) region.

The model presented in this section describes solar cells based on p-n homojunctions. An equivalent treatment has been applied to cells based on heterojunctions, i.e., contacts formed by semiconductors with different band gaps and band positions [46, 53]. The result of these calculations is that the I/V curves of heterojunction cells are described by diode equations of the same form as the equations (2.29) and (2.30) derived for homojunctions. We will use equation (2.30) to model the behaviour of the heterojunction devices investigated in this work in the Chapters 5 and 6 using the shunt and series resistances as fit parameters.

The mechanism of photocurrent generation in heterojunction cells is different from p-n homojunction devices, because the band offsets at the interface determine the separation of excitons. We present a detailed operational model of heterojunction cells based on materials with high exciton binding energies, often referred to as excitonic heterojunction cells, in the following section.

2.2.2 Excitonic heterojunction cells

The excitonic cell concept is the basis of a large class of recently developed photovoltaic devices. Materials with low dielectric constants, where the binding energies of photogenerated excitons are much higher than in Si [54], are used as absorbers, so that electrostatic potentials sufficient to separate the excitons can only be created by the band offsets at a heterojunction interface [44, 54]. Barker et al. [55] have proposed a model for excitonic heterojunction cells which we will use in the following to derive the operating principle and the I/V characteristics of these devices.

Cell model

The cell model consists of two phases of semiconducting materials, one n-type and one p-type, with dissimilar band structures. Excitons are photogenerated in one of the two phases or in both, depending on the size of the respective band gaps. The excitons can reach the interface by diffusion, where the two phases form a heterojunction. There, by a mechanism described below, excitons are split into a free electron in the n-type phase and a free hole in the p-type phase. Also by diffusion, the spatially separated carriers are transported through the semiconductor phases to metal electrodes, where they pass ohmic contacts and contribute to the current through an external load. The heterojunction cell structure and operation are displayed in Fig. 2.10.

The cell materials are not doped, so that the density of mobile charge carriers is low. As a consequence and characteristic difference to p-n homojunction cells, carrier diffusion across the interface and the formation of space charges is very low. Electric fields and the resulting band bending are therefore negligible in comparison to the intrinsic band offsets at the interface [44].

In certain types of excitonic cells, such as dye-sensitized solar cells, no exciton creation occurs in either one of the n-type and p-type transport phases. Instead, a monolayer of absorbers, where all excitons are generated, is introduced at the interface between the phases [56]. Charge carriers are created by separation of the excitons at this interface,

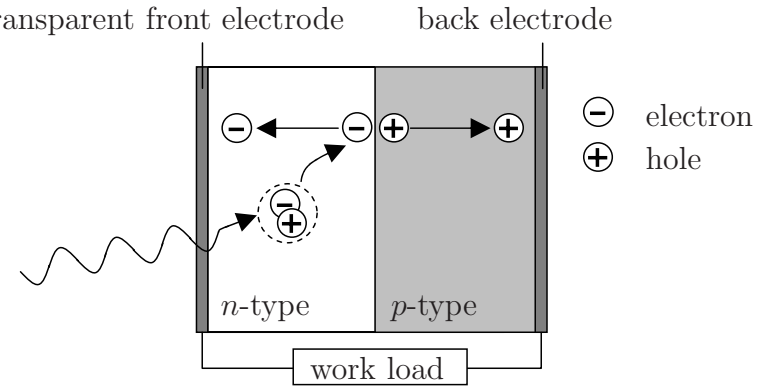

Figure 2.10: Exciton creation and separation in an excitonic solar cell.

and they are transported by the transport phases, not by the sensitizer interlayer. Therefore, the operating principle of these sensitized cells can be described by the bilayer model displayed in Fig. 2.10 [57, 58].

As mentioned before, the excitonic cell design relies on absorber materials with high exciton binding energies which require the band offsets at a heterojunction for exciton separation. Figure 2.11 displays the band alignment necessary to separate the excitons and prevent the separated charge carriers from diffusing back across the interface. The position of the VB in the n-type phase has to be below the VB in the p-type phase, and the position of the CB in the n-type phase has to be inside the band gap of the p-type phase. Such an alignment is called a 'type II heterojunction'.

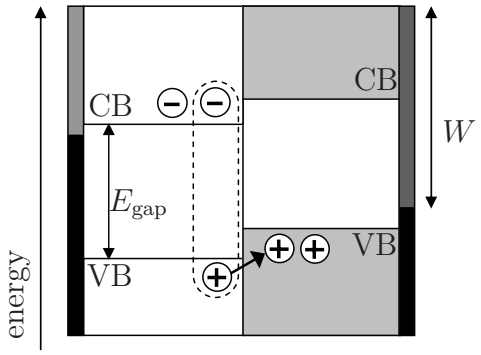

Figure 2.11: Electronic band structure of an excitonic heterojunction cell, W: metal electrode work function.

As an exciton approaches the heterojunction from the n-type side, the hole, which tends to travel 'upward' on the energy scale for electrons, 'sees' energetically allowed states in the p-type region, while the electron, limited to traveling 'downward', does not (see Fig. 2.11). Additionally, the transfer of charges across the interface is only allowed, if the

gained energy by the 'vertical' movement of the charge carriers is sufficient to break the exciton binding forces. If an exciton approaches from the *p*-type side, a mirror process transfers the electron across the interface, and creates a pair of free charge carriers likewise.

Since electric fields are absent, the free carriers move through the transport phases by diffusion, but they cannot diffuse back across the interface due to the absence of allowed states on the other side, see Fig. 2.11. A net current of carriers towards the metal electrodes establishes, as soon as a concentration gradient of carriers is built up by the carrier generation at the interface.

I / *V* characteristics

We use the bilayer model to describe the current / voltage characteristics of excitonic devices, following the intuitive description by Barker et al. [55]. Their treatment is simple and gives convincing results, including interesting clues to much debated questions such as the origin of photovoltages in these cells [59]. The obtained I/V curves are similar to the diode curves simulated using the modified Shockley equation (2.30).

Figure 2.12 displays band diagrams of a type II heterojunction device under different biases applied to the metal electrodes. The semiconductor phases are represented by their respective VB and CB edges, and the metal electrodes by the electronic states filled up to the respective Fermi energies (black rectangles). When charge carriers are generated at the heterojunction interface, currents driven by electric fields and by concentration gradients will flow, as indicated by arrows in Fig. 2.12.

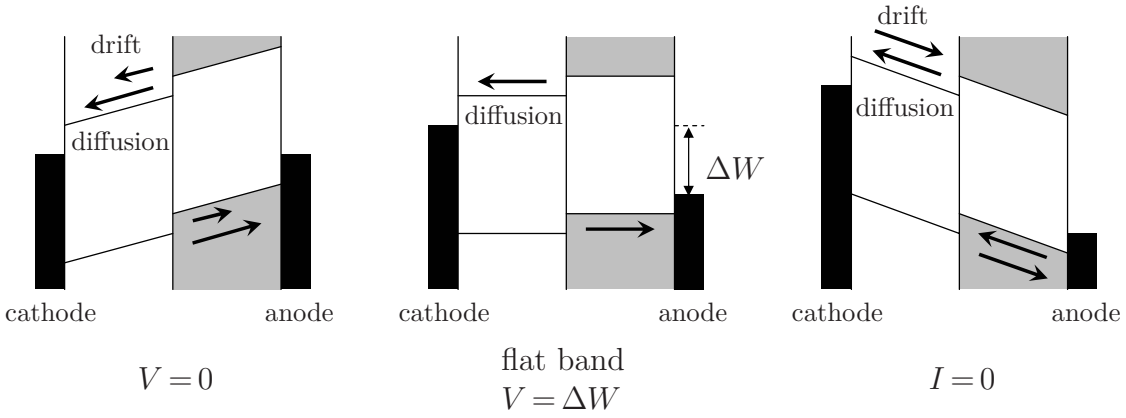

Figure 2.12: Excitonic devices under different external biases, with carrier generation at the heterojunction interface. Reproduced from [55].

The center image in Fig. 2.12 shows the device when a voltage equal to the work function difference of the metal electrodes ΔW is applied. This situation is called the 'flat band condition', because the semiconductor bands are not tilted on the energy scale. Charge carriers in the device see no electric field, even though an external bias is applied. Nevertheless a negative current, i.e., opposed to the applied bias, is flowing, induced by the carrier generation at the interface and the resulting concentration gradient.

In the left image in Fig. 2.12, the voltage is reduced to $V = 0$ and the device is in short circuit condition. The current flowing in this situation is, by definition, the short circuit current I_{sc}. It is higher than the current in flat band condition, because the generated charge carriers are exposed to an electric field due to band tilts induced by the voltage change. An additional drift current emerges, which increases the negative diffusion current flowing in flat band condition. Correspondingly, the current will vanish when the voltage is sufficiently increased relative to the flat band condition, as shown in the right image of Fig. 2.12. The drift current caused by the band tilt is then opposite to the diffusion current, and the two cancel each other.

When illumination is switched off and carrier generation at the interface stops, different device currents result from the voltages applied before. This situation is illustrated in Fig. 2.13. Obviously, no current is flowing in either flat band or short circuit conditions. At voltages higher than the work function difference ΔW, however, carriers can pass the potential barriers at the interfaces by thermal activation or tunneling. The resulting current is indicated by arrows in the left image for electrons in CB states.

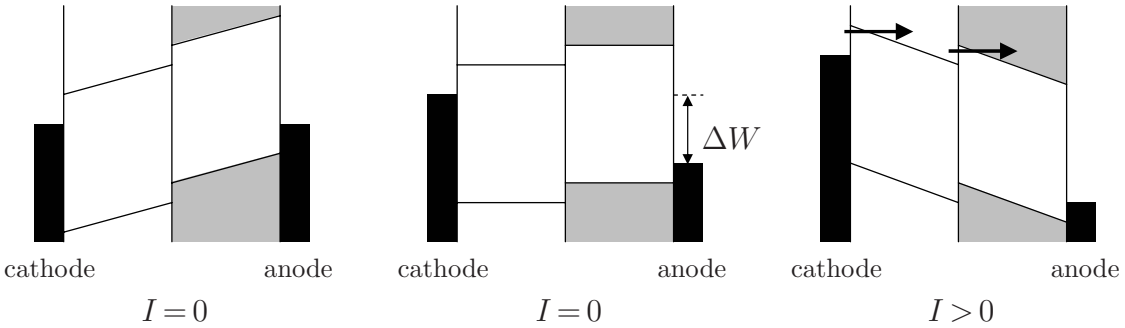

Figure 2.13: Excitonic devices without carrier generation under different external biases. Adapted from [55].

The previous considerations of excitonic cells under different biases combined yield the qualitative current / voltage curves shown in Fig. 2.14. Each diamond (light curve) and triangle symbol (dark curve) in the graph corresponds to a current / voltage state displayed in one of the images in the Figs. 2.12 and 2.13 above. Both curves show a

diode type behaviour. For the device in light, the curve is offset by the photocurrent I_{sc}, but similar in shape to the dark curve. The photovoltage U_{oc} and the maximum power output P_{el}^{max} are indicated in Fig. 2.14 also.

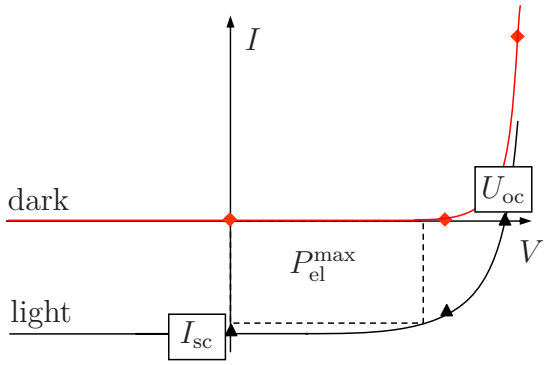

Figure 2.14: Qualitative I/V curves obtained from an excitonic cell model. Adapted from [55].

Working principle of excitonic solar cells

The diode behaviour of an excitonic heterojunction cell derived above is similar to the characteristics that one obtains from modeling a *p*-*n* homojunction device, as described in Section 2.2.1 and simulated in Fig. 2.8. The physical properties leading to the diode behaviour, however, are different. It is band offsets, that lead to the diode behaviour in the case of excitonic cells, and space charge zones in the case of *p*-*n* junctions.

Simple conclusions regarding the influence of material parameters on the characteristics of excitonic cells may be drawn from the modeled I/V curves. In the literature, it has been concluded from a metal-insulator-metal model that the work function difference of the electrode materials ΔW is equal to the open circuit voltage U_{oc} of the cells [59]. From the model presented above, however, we expect that U_{oc} should be *larger* than ΔW. Rather, an upper limit of U_{oc} is given by the difference between the edges of the CB in the *n*-type phase and the VB in the *p*-type phase, the so called effective band gap [44]. This difference is the potential energy of the separated electron and hole after separation and thermalization.

For certain excitonic cell types, diffusion currents driven by concentration gradients are commonly considered as the only significant contribution of energy conversion [25, 60]. In the model presented here, in contrast, also drift currents in bands tilted by internal electric fields contribute to the resulting photocurrent. However, the internal electric fields only drive the photocurrent when the device is close to the short circuit condition,

depicted in the left image in Fig. 2.12, where only very low power output can be generated. Close to the open circuit condition, electric fields are instead opposing the photocurrent, and they are at best insignificant at the maximum power position. We expect the maximum power to be available close to the flat band condition shown in the center image in Fig. 2.12, where no significant drift currents flow. According to the description presented here, the power generating current is driven by a concentration gradient and not by an internal electric field.

2.2.3 Consequences for excitonic cell designs

Carrier recombination and diffusion lengths

Recombination of electrons and holes presents a major loss mechanism in photovoltaic devices. The rate of recombination is enhanced at impurity sites with electronic states inside the band gap of the host material. Charge carriers can be trapped in these states, which act as a pathway for electron-hole annihilation. If a majority carrier, i.e., an electron in the n-type phase or a hole in the p-type phase, is trapped, it will depend on the spatial concentration and mobility of minority holes and electrons whether recombination or de-trapping will take place.

If the minority carrier concentration is sufficiently small, then even a high density of defects will not decrease the diffusion length of majority carriers substantially. This length is the distance that a charge carrier or exciton can travel in a material before recombination occurs. If the minority carrier concentration is high, recombination at defect sites is fast and a very low trap density is required to achieve diffusion lengths long enough for the carriers to reach the electrodes. Tightly bound electron-hole pairs, so called Frenkel excitons, are most sensitive to traps, since the distance between the charge carriers is small. Their wavefunctions partially overlap and recombination occurs quickly.

Excitonic cell materials and structure requirements

As explained in Section 2.2, both electron and hole currents are present in Si cells. The resulting high concentration of minority carriers requires a high crystal quality with a very low density of defects in order to avoid recombination and to achieve efficient cell operation.

In excitonic cells, in contrast, only majority carriers, i.e., electrons created on the n-type side of the interface and holes on the p-type side, are present in either phase. The density of minority carriers in both phases is very low [44]. The potential losses by recombination are therefore negligible, and the requirements for material purity and for the absence of defects are greatly relaxed compared to Si cells. This robustness opens up new classes of materials that can be used for photovoltaic power conversion in excitonic cells: Multi-crystalline including nanocrystalline solids, both organic and inorganic, and even amorphous phases of, e.g., polymers, with high densities of bulk defects, grain boundaries, and interfaces become usable.

As a consequence of the higher defect concentration, the *exciton* diffusion lengths in organic and nanocrystalline materials are much lower than the ones in Si cells, as explained above. Therefore, while free electrons and holes can travel long distances, excitons can only travel very short distances. The typical diffusion length of excitons in, e.g., organic semiconductors, is on the order of 20 nm. Excitons created at greater distances from the interface will recombine before reaching it and will thus not contribute to the photocurrent [61].

Hence, in a device with a planar junction as shown in Fig. 2.10, only excitons created in a layer with a thickness on the order of the diffusion length will contribute to the photocurrent. If this active layer is only a few tens of nanometers thick, sufficient optical densities to harvest a large portion of the incident light can hardly be achieved. Therefore, various kinds of alternative geometries for excitonic cells have been developed in order to generate higher photocurrents. Evidently, the structures of excitonic cells using materials with low exciton diffusion lengths need to be controlled on the nanometer scale in order to achieve high conversion efficiencies. In the following section, several heterojunction cell designs based on nanostructured geometries will be described.

2.3 Nanostructured excitonic cell designs

The photovoltaic cell concepts addressed in this section employ various cell structures to ensure that photogenerated excitons reach a charge separating interface before recombination. We will describe the cell designs, the operating principle, the materials and methods used for the fabrication as well as advantages and limitations of the concepts.

2.3.1 Nanostructured organic cells

The use of organic materials in photovoltaic devices has received much attention ever since organic heterojunctions were shown to yield considerable conversion efficiencies [62]. In the following, we describe a cell design based on interpenetrating organic phases which utilizes the concept of bulk heterojunctions.

Organic bulk heterojunctions

A heterojunction between interpenetrating n-type and p-type phases which both extend through the whole absorber layer, as shown in Fig. 2.15, is called a bulk heterojunction. If the length scale of the interpenetrating patterns is equal to or below the exciton diffusion lengths, all excitons photogenerated in that area will reach the interface and yield a pair of free charge carriers. The two phases are contacted individually by metal electrodes to collect the charges. The front electrode consists of a transparent material such as glass coated with a transparent conducting oxide (TCO) [24, 61, 63].

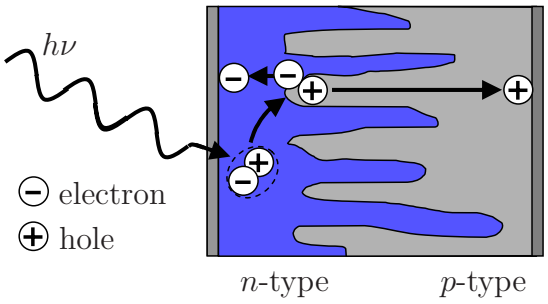

Figure 2.15: Organic photovoltaic cell with interpenetrating phases forming a bulk heterojunction. Adapted from [61].

As explained in the previous section, the created majority carriers are confined to their respective phases and have large diffusion lengths due to the absence of minority carriers. Internal electric fields are expected to be insignificant for driving the currents, so that diffusion induced by a concentration gradient predominantly generates the currents. Obviously, the transport of charge carriers will be most efficient, if a direct continuous path which does not cross interfaces exists to the collecting metal electrodes. It is therefore required that the charge transport phases both form connected networks. If, e.g., the n-type phase forms islands surrounded completely by p-type material, then electrons generated at the interface of an island will be trapped inside, since their path to the anode is obstructed by interfacial band offsets. An efficient bulk heterojunction

must hence consist of bi-continuous interpenetrating phases, as indicated by the network shown in Fig. 2.15.

Cell materials and fabrication

Organic heterojunctions are formed by bulk phases of molecules with different electron affinities and ionization energies. Molecules with high electron affinities, called acceptor molecules, form the n-conducting phase, and molecules with low ionization energies, called donor molecules, form the p-conducting phase. The molecules are usually chosen such that the HOMO-LUMO gap allows light absorption in both materials.

Organic molecules can be processed by various techniques including evaporation from a heated source in ultrahigh vacuum (UHV), and solution based methods such as spin-coating, dip-coating, or drop-casting. Small organic molecules are usually evaporated, while polymers and functionalized macromolecules are processed from solution [23, 63]. Bulk heterojunctions can be fabricated by either simultaneous or sequential deposition of the n-type and p-type materials: Following the first approach, two types of molecules can be simultaneously co-evaporated or deposited from a blended solution. In the second approach, evaporation or solution processing is executed sequentially for the two phases.

The structure requirements for the thin films include (i) separated phases of n-type and p-type molecules (i.e., no mixing on a molecular level), (ii) a high degree of molecular ordering within the phases for high carrier mobilities, and (iii) an interpenetration of the phases on the nanometer scale. With both simultaneous and sequential deposition of molecules, it is difficult to meet these requirements. When deposited simultaneously, molecules tend to either mix on a molecular scale or de-mix completely, creating large domains with little interpenetration [61, 62]. When deposited sequentially, it is necessary that the phase deposited first forms structures which allow the penetration of the second layer. E.g., an array of nanometer spaced columns formed by p-type molecules can form a bulk heterojunction structure, if the voids are filled by a phase of n-type molecules [64, 65]. Further problems of organic cells are created by the stability limitations that the cells often face, caused by the tendency of the n-conducting phase to oxidize quickly in air [66, 67].

The problems associated with the fabrication of an organic bulk heterojunction structure and also with low molecular stability can be addressed by replacing the n-type organic phase with a stable inorganic n-conductor. The p-type organic phase can be retained, along with its advantages such as good p-conductivity and processing flexibility. New structures can be created, since the morphology and the surface properties

of organic and inorganic materials are different, leading to effective phase separation. This approach will be important for the cell concepts described in the following sections, especially in the Sections 2.3.3 and 2.3.4.

2.3.2 Dye-sensitized solar cells

Structure and operating principle

The first cell type that combined organic material with an inorganic n-type phase was the dye-sensitized solar cell (DSSC) presented by O'Regan and Grätzel in 1991 [28]. The n-type phase of the cell is a network of TiO_2 nanocrystals in the anatase crystal phase. TiO_2 is a very stable metal oxide which can be characterized as a wide gap n-type semiconductor with a band gap energy $E_{\mathrm{gap}} = 3.2\,\mathrm{eV}$. The hole transport in the devices is not provided by a solid state semiconductor, but by a couple of mobile I^- and I_3^- iodine ions in a liquid electrolyte that fills the pores of the TiO_2 network. Thus, the two phases form a bicontinuous network and a liquid-solid heterojunction, but neither of them absorbs light in the visible, as mentioned before. The interface is therefore covered with a monolayer of sensitizing dye molecules, which absorb light and inject electrons into TiO_2 from their excited state.

A large interface area is necessary in order to ensure that a large amount of molecules can be adsorbed and high absorption can be achieved. Multilayers of dye cannot be used since electron injection into TiO_2 requires direct contact [56]. Interfaces with a large area are created by either porous structures of nanoparticles [42] or by arrays of nanowires [68]. Additionally, the microstructure of the TiO_2 phase can include scattering centers which raise the cell performance by light backscattering resulting in increased absorption [69, 70]. All materials involved have the potential to be produced at a far lower cost than crystalline Si.

The principle of operation of a DSSC is depicted in Fig. 2.16. A photon with an energy larger than the HOMO-LUMO gap of the dye enters the cell through a TCO window and excites a dye molecule attached to TiO_2. The photogenerated exciton is then separated by the injection of an electron into the CB of TiO_2. An I^- ion in the electrolyte regenerates the ionized dye molecule by transferring an electron. After this transfer, two of the neutralized iodine atoms and one I^- ion form an I_3^- complex, corresponding to the gross reaction

$$2\,\mathrm{dye}^+ + 3\,\mathrm{I}^- \longrightarrow \mathrm{I}_3^- + 2\,\mathrm{dye}\,(\text{ground state}). \tag{2.35}$$

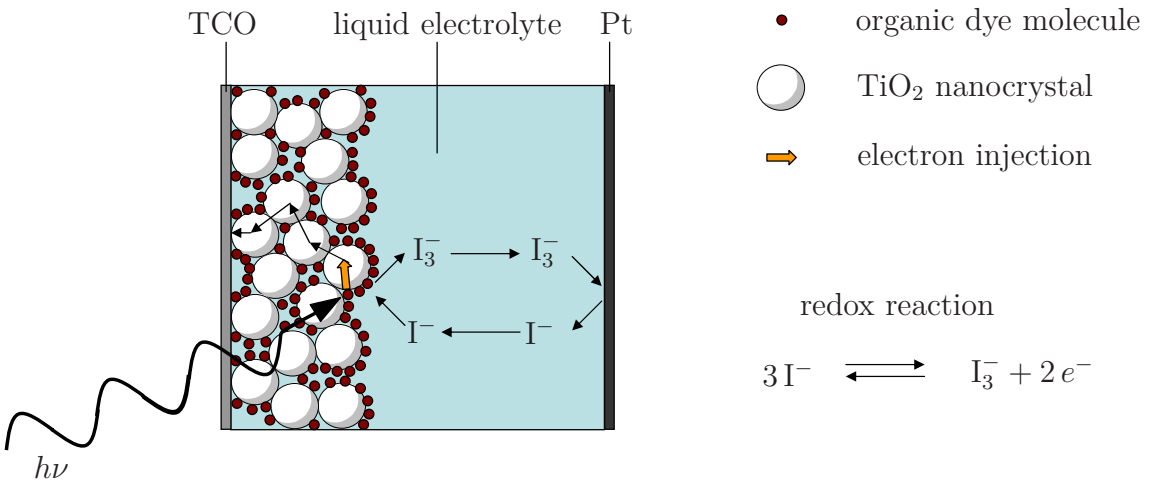

Figure 2.16: Cell structure and operating principle of a DSSC.

These reactions produce an excess amount of the I_3^- complex at the dye coated interface, which extends through the whole TiO_2 network. The resulting concentration gradient drives a current of I_3^- towards the Pt cathode. There, the I_3^- complex is reduced with Pt as a catalyst and I^- ions are produced:

$$I_3^- + 2\,e^- \xrightarrow{Pt} 3\,I^- \tag{2.36}$$

A diffusion current of I^- ions from the Pt cathode to the dye-sensitized anode is established by a concentration gradient. The free electrons in the TiO_2 CB are transported to the TCO electrode also by diffusion, so that the circuit of electric currents is closed. Electric fields are not significant for the transport because of charge shielding in the porous structure of interpenetrating n-type and p-type phases [56, 60].

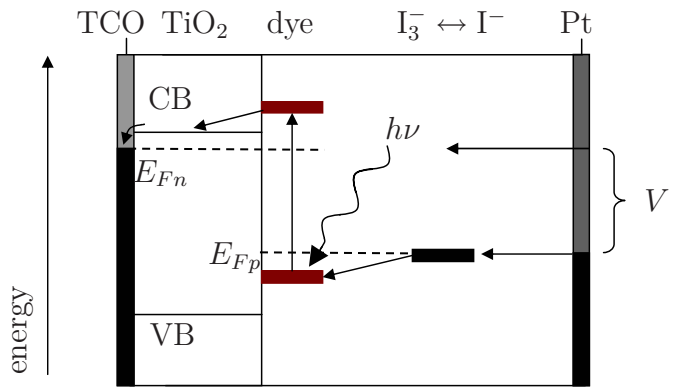

Figure 2.17: Schematic of the electronic structure and the charge transfer reactions in a DSSC.

Figure 2.17 displays the energy level structure of a DSSC and the individual charge transfer reactions. The absorption of photons in the cell is determined by the gap between the HOMO and the LUMO of the dye (dark red squares). The absolute position of these levels on the energy scale determines the electron transfer processes: The LUMO must be above the TiO_2 CB edge at 4.2–4.3 eV below the vacuum level [59, 71], and the HOMO must be below the redox potential of the I^-/I_3^- redox couple.

In an operating cell, as described in Section 2.2 for *p*-*n* junction cells, two quasi-Fermi levels can be defined. In a DSSC, electrons in the LUMO state of the dye are in equilibrium with injected electrons in the TiO_2 CB, but not with the 'holes' in the HOMO of the dye. E_{Fn} is the quasi-Fermi level of these electrons and is used to describe their spatial concentration in the *n*-conducting TiO_2 phase [57]. E_{Fp} is the quasi-Fermi level of the holes in the dye molecules in equilibrium with the redox couple. It is hence equal to the redox potential [72].

The efficiency of charge separation at the interface is crucial for the DSSC performance. Electron injection into the TiO_2 CB competes with recombination reactions, i.e., the relaxation of an excited electron in the dye LUMO back to the HOMO, or the transfer of an injected electron back to an empty HOMO state of a dye molecule. The transfer of electrons in heterogeneous systems has been described with non-adiabatic electron transfer theory based on the Fermi golden rule. In this context, the term non-adiabatic means that the transfer is assumed to occur too fast for the involved species to adjust continuously to the change of the potential surface of nuclear motion. It predicts that the time scales of the injection reaction are governed by the spatial overlap of the donor state and the acceptor state, i.e. the coupling strength, their energetic match, and also on the density of acceptor states [73, 74].

For several metal complex dyes, timescales for the electron injection into TiO_2 on the order of femtoseconds have been observed. This ultrafast injection has been explained by the high density of acceptor states available in the TiO_2 CB, and by the dye LUMO being concentrated on the hydroxyl or carboxyl anchor groups of the dyes. The spatial distribution of the dye HOMO, in contrast, is often dominated by atomic orbitals of the central metal atom. The spatial overlap between the HOMO and the TiO_2 CB states is therefore much smaller, so that the back reaction is much slower than the electron injection and the subsequent electron transport in the TiO_2 CB [75]. The high density of electron trap states at the TiO_2 surface also plays an important role, since it increases the presence of electrons close to the surface [76].

DSSC fabrication and performance

The manufacture of DSSCs includes a sequence of production steps, the first of which is the fabrication of the porous TiO_2 structure. For the standard method, a highly viscous paste consisting of TiO_2 nanoparticles and organic additives is distributed as a film on a transparent conductive substrate. The sample is then annealed at 400–450°C to burn out all organic material and enhance particle contact. The obtained porous film is sensitized by immersion into a solution of organic dyes. The back electrode is suspended above the sensitized front electrode by spacers, so that the created void can be filled with the liquid electrolyte by capillary forces [56].

Power conversion efficiencies above $\eta = 10\%$ have been reported for DSSCs, making these devices the most efficient excitonic cells so far [28, 56, 77]. The efficient charge injection process described above is an important prerequisite for this performance. Long term stability, however, is too low for commercial application where lifetimes of at least 15 years are required. One reason is that all organic dyes used in DSSCs have a finite probability of being permanently damaged by photodegradation in each redox cycle. In long term operation on the order of years, the cells therefore show decreasing efficiency. Another stability problem is created by leakage of the liquid electrolyte in the cell, resulting in immediate power loss and the spill of harmful liquids into the environment. Sealing the cells tightly is difficult due to the large mechanical strain caused by high temperature differences between daily irradiation and nightly cooldown.

It has been attempted to replace the liquid electrolyte by solid phases of organic [78, 79] or inorganic p-conducting materials [80], but these cells have shown lower efficiencies than the liquid electrolyte DSSCs and have not solved the problems associated with dye degeneration. This issue is solved in hybrid cells and quantum dot sensitized cells described in the following Sections 2.3.3 and 2.3.4, where the dye molecules are additionally replaced by more stable materials. Apart from the replacement of the organic dye and the liquid electrolyte, they are, like DSSCs, based on porous inorganic n-type semiconductors.

2.3.3 Hybrid organic / inorganic cells

Structure and operating principle

The term hybrid organic / inorganic cell technically covers a wide range of cell types, including, e.g., the DSSCs described in the last section. However, we will only use

it for solid state excitonic cells with a transparent inorganic n-type semiconductor in contact with a light-absorbing organic p-type semiconductor [81, 82]. The system we will describe here features a porous network of TiO_2 nanoparticles, known as an electron conductor from DSSCs, as well as a light sensitive polymer used as an absorber and hole conductor [38, 39, 83].

The structure and operating principle of TiO_2 based hybrid cells are shown in Fig. 2.18. The pores of the TiO_2 structure are filled with light-absorbing polymer, so that a bulk heterojunction with continuous carrier paths to the metal electrodes is formed. Photons enter the cell through a transparent TCO window and generate excitons throughout the bulk of the polymer phase, especially inside the filled pores of the TiO_2 structure. The band structure of the two phases forms a type II heterojunction, as shown in Fig. 2.19, so that excitons are separated into free electrons in the n-type and holes in the p-type phase. As in purely organic cells, excitons have to reach the interface by diffusion in order to contribute to the photocurrent. The use of nanoparticles with a diameter on the order of the exciton diffusion length in the polymer material will create pores of similar dimensions, so that excitons created inside them can reach the interface.

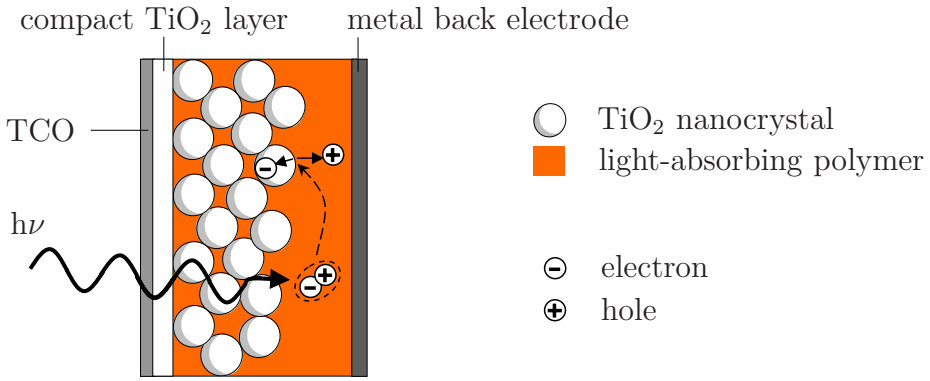

Figure 2.18: Device structure and exciton separation in a hybrid organic/inorganic photovoltaic cell.

Free electrons generated at the organic / inorganic interface will be transported along continuous paths in the TiO_2 network, and the free holes along continuous paths in the polymer, towards the metal electrodes. By structural arrangements, the metal electrodes must be prevented from acting as electron-hole recombination channels: If both the electron and the hole transport phase are in contact with the same metal electrode, electrons and holes can recombine in the metal where they are no longer separated by a band of forbidden states [84]. One can ensure that each transport phase is in contact with only one metallic electrode by fabricating homogeneous electrode contacts, as shown in Fig. 2.18: A compact TiO_2 layer is deposited on top of the front

electrode in order to block holes in the polymer phase [85]. At the back electrode, the polymer film is made thick enough to cover the TiO_2 nanocrystals completely, so that electrons in the TiO_2 are blocked.

Figure 2.19 shows the energy level structure of a hybrid device with a type II heterojunction inducing charge separation at the organic / inorganic interface. Transparent conductive fluorine-doped tin oxide (FTO) is used as a front electrode. The FTO work function ($W_{\mathrm{FTO}} = 4.4\,\mathrm{eV}$ [59]) closely matches the TiO_2 Fermi energy, so that an ohmic contact is formed [45, 53].

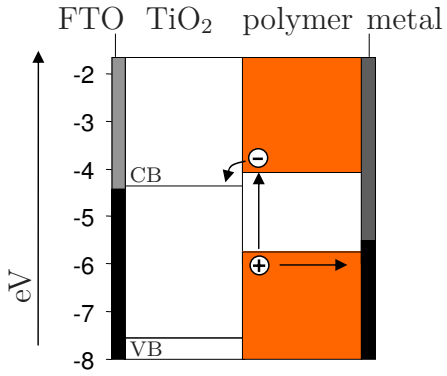

Figure 2.19: Heterojunction structure in a hybrid photovoltaic cell.

The requirements for the energetic structure of the polymer as displayed in Fig. 2.19 include the following: (i) The polymer LUMO has to be above the TiO_2 CB at 4.2–4.3 eV below the vacuum level to enable electron injection. (ii) The polymer HOMO has to be below the TiO_2 CB to prevent recombination. (iii) The difference between the polymer HOMO and the TiO_2 CB defines the effective gap of the cell and sets an upper limit for the expected photovoltages. Since high voltages are important for energy supply applications, the polymer band positions should be such that the largest part of the band gap of the polymer is available for the effective gap of the device. The work function of the back electrode should be close to the Fermi level of the polymer, so that an ohmic contact is formed at the polymer / metal interface.

Fabrication methods

The device concept of the hybrid cells described in this section is comparable to purely organic polymer / fullerene cells. However, the introduction of inorganic materials offers additional means to control the cell morphology in terms of phase separation and network formation by, e.g., adjusting particle sizes or processing methods. Various

fabrication methods including sequential spin-coating [38] and solution processing at varying relative concentrations of the species in a mixed solution [83, 86] have been applied to cell production. These methods offer incomplete structure control on the nanometer scale, resulting in insufficient mixing and a bilayer cell structure in the case of sequential fabrication, and random structures without connected networks of the respective phases in the case of simultaneous deposition. Thermal treatments were necessary to sinter the devices and increase phase interpenetration and phase cohesion [39, 87]. In this work, we will introduce layer-by-layer self-assembly as a fabrication method for hybrid cells, with the aim of better structure control.

2.3.4 Quantum dot photovoltaic cells

Semiconductor nanocrystals called quantum dots (QDs)[88] are a new class of materials that has received much attention in optoelectronics [89], biological sensing [90] and quantum information processing [91] in recent years. In this section, we briefly describe the unique optical and electronic properties of QDs and their application as absorbers in photovoltaic cells.

Quantum dot properties and synthesis

We use the term QD for nanocrystals of inorganic compounds which show semiconducting behaviour as bulk solids. If the crystallite size is smaller than the exciton radius of the material, confinement effects will change the electronic level structure observed for bulk crystals. In very small dots, which will not be considered or used in this work, the band type electronic structure from the bulk is split up into discrete levels. We will use the terms VB and CB when referring to the electronic levels of QDs, in spite of the spatial confinement of charge carriers. The position of the CB is raised by the confinement, and the position of the VB is lowered, resulting in an increased band gap energy [92–94]. The effective mass approximation (EMA) predicts this increase ΔE_{gap} as [95]

$$\Delta E_{\text{gap}} = \frac{\hbar^2 \pi^2}{2R^2} \left(\frac{1}{m_e^*} + \frac{1}{m_h^*} \right), \tag{2.37}$$

where R is the particle radius, and m_e^* and m_h^* are the effective masses of electrons in the CB and holes in the VB, respectively. The optical properties of the QDs can hence be adjusted by controlling their sizes. This feature makes them very attractive as absorbers in photovoltaic applications, as we will discuss below.

QDs can be grown either on crystalline substrates by epitaxial methods [96] or as colloids in solutions containing complexes of the constituent atoms [97, 98]. Figure 2.20 shows a cartoon of the latter type. It consists of the semiconductor nanocrystal and an organic capping layer which controls the growth process and solubilizes the dots in different solvents. The QD shown in Fig. 2.20 has a capping of trioctylphosphine oxide (TOPO) which is commonly used to grow, e.g., cadmium selenide QDs in organic solvents [99, 100].

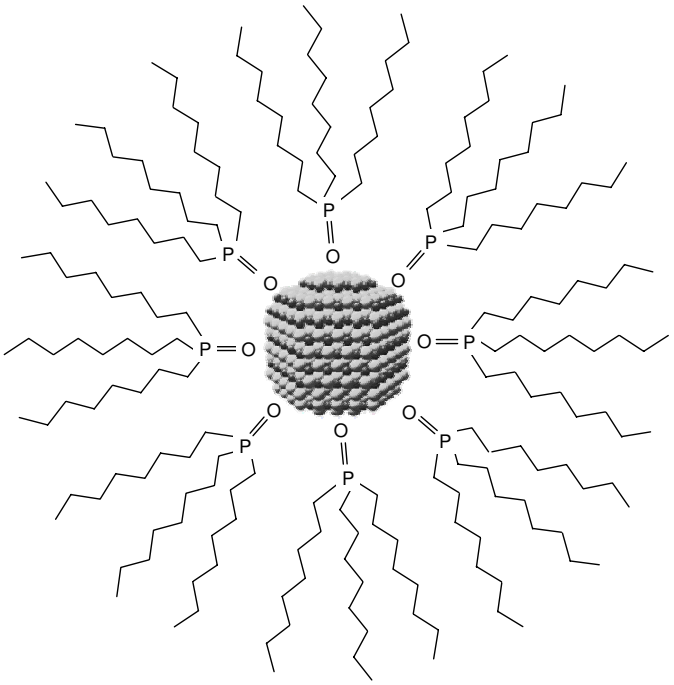

Figure 2.20: Quantum dot capped with trioctylphosphine oxide (TOPO)

QDs in third generation photovoltaic cells

Several features of QDs make them a very interesting material for applications in photovoltaics. Apart from unique optical properties, they have a remarkable stability against photodegradation, much higher than organic dyes used as absorbers in DSSCs and molecular organic cells [30]. This advantage is significant, considering the requirement of at least 15 years of stable operation for commercially useful solar cells, which we have mentioned above.

A range of compounds with very different band gaps and band positions can be grown as colloidal QDs [31, 33, 101, 102]. Further, the size can be controlled precisely, so that the band structure can be tuned effectively for each compound by the confinement effects

[98]. These effects and the wide range of materials allow to match the band positions of the QDs with other materials, e.g., to obtain effective heterojunctions. Further, the efficiency of QDs as absorbers covering the solar spectrum can be maximized by an adjustment of the band gap.

When electric energy is generated from the solar spectrum by photovoltaic cells, energy losses are incurred by missing photons on the low energy side of the absorber band gap and by thermalization on the high energy side, as explained in Section 2.2.1. The losses cannot be minimized simultaneously on both sides by moving the band gap. It has been shown by Klimov and Schaller [31] that QDs have a unique non-linear optical property that could utilize the excess energy of hot excitons generated by high energy photons for an increased conversion efficiency: Since the boundary conditions imposed on nuclear vibrations by the crystal surface become more important with decreasing size of the crystal, the density of states of phonons is reduced in QDs. This density determines the efficiency of exciton-phonon scattering and hence the time scales of thermal relaxation. The reduced density of states of phonons creates a 'phonon bottleneck' which does not exist in bulk crystals and which increases the lifetime of hot excitons [103, 104]. The conversion of single hot excitons into multi-excitons, which is an Auger-type process that is not affected by the phonon density, is hence favored over thermal relaxation and has been shown to occur with high efficiencies [32, 33]. Figure 2.21 shows the gross reaction of a high energy photon creating a biexciton. Since the thermalization losses on the high energy side of the band gap are reduced by this effect, the band gap can be shifted to lower energies in order to reduce the losses incurred by missing low energy photons [31].

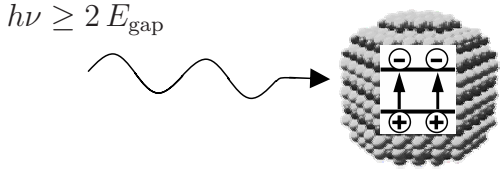

Figure 2.21: Single photon with high energy creating a biexciton in a QD.

Owing to these outstanding features, colloidal QDs have recently attracted attention in photovoltaics research [105]. Various heterojunction cell concepts using QDs have been proposed in the literature [26]. The proposed materials include CdSe QDs chemically linked to TiO_2 nanoparticles [106], as well as bulk layers of CdSe and CdTe QDs [30]. Conceptually, QDs have also been proposed as absorbers for intermediate band photovoltaics, which follows the concept of photon up-conversion [107]: A partially filled intermediate band inside the band gap will allow two sequentially absorbed low energy

photons to create one high energy exciton in an up-conversion process, leading to high photovoltages while avoiding losses in the low energy region of the solar spectrum. This process is the opposite of multi-exciton generation, which relies on down-conversion of photons, and has not been experimentally verified.

QD sensitized hybrid photovoltaic cells

In order to extract free charges from excited QDs, the dots can be placed at the surface of a semiconductor material with an appropriate band structure, so that a type II heterojunction is formed and single or even multiple excitons can be separated. A cell design similar to a DSSC with TiO_2 nanoparticles as electron acceptors is shown in Fig. 2.22. Instead of a liquid electrolyte, however, a transparent *p*-type polymer phase is used as a hole acceptor and for hole transport, resulting in higher stability. Efficient hole transfer from QDs to conjugated polymers, which is required in this cell design, has been demonstrated by fluorescence quenching in blends of two such materials [108]. This QD sensitized cell concept is similar to the hybrid cells described in the previous section. However, no light-sensitive polymers are used here to ensure that all excitons are created in the QDs. Since the QD monolayer is placed directly at the charge separating interface formed by TiO_2 and the polymer, all excitons can instantly be separated without diffusive transport and possible loss [26, 101, 109].

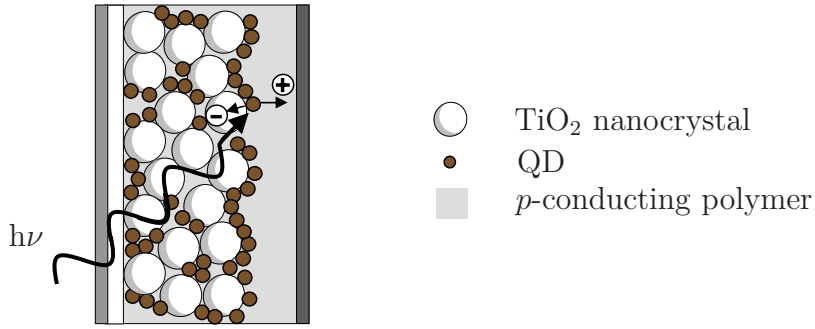

Figure 2.22: Structure of a QD sensitized hybrid photovoltaic device.

The energy level positions required for a directional transfer of charges in hybrid QD sensitized cells are comparable to the structures of the other excitonic cells described in this section. The CB edges of TiO_2, of the QD, and of the polymer must form ascending 'stairs', so that electron injection is possible *only* into TiO_2, and not into the polymer. An equivalent ascending structure is required for the VB edges, so that a transfer of the hole created by electron excitation and transfer is possible only to the polymer, and not to TiO_2. These requirements are met by the band structure sketched in Fig. 2.23,

to which we will refer as a double-heterojunction. Note the large polymer band gap to avoid light absorption. The effective gap which determines the photovoltage of this cell is the difference between the edges of the TiO_2 CB and the polymer VB, as for the hybrid cells described in the preceding section.

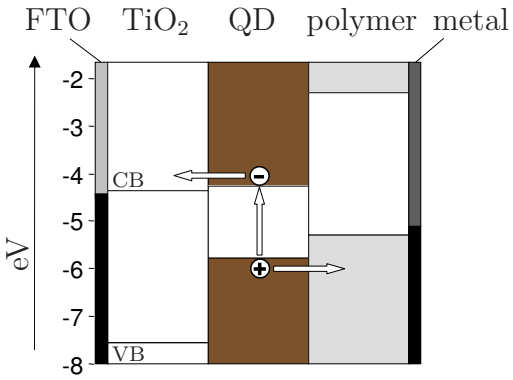

Figure 2.23: Energy level structure of a QD sensitized hybrid photovoltaic device.

The QD cell design presented here is similar to extremely thin absorber cells [110, 111]. These cells consist of a nanostructured heterojunction of transparent inorganic materials, which are separated by a thin absorber film. The low absorber thickness ensures that excitons created in the absorber layer quickly reach the interface for separation. A high total area of the interlayer is necessary to achieve sufficient absorption.

QD sensitized TiO_2 films have already been used as electrodes in electrochemical cells based on liquid electrolytes. The QDs were attached to TiO_2 by different methods including nucleated growth [109], physisorption [101], and chemical linking [106]. The layer-by-layer self-assembly method, which we used in this work, has not been applied to the attachment so far. The cell design displayed in Fig. 2.22, which combines solution processable materials, colloidal QDs as absorbers and polymers as hole conductors, in a solid state configuration, has not been realized so far, either.

2.4 Layer-by-layer self-assembly of nanostructured thin films

The designs of hybrid photovoltaic devices described in the Sections 2.3.3 and 2.3.4 require the fabrication of organic / inorganic thin films which are structured on the nanometer scale. The layer-by-layer self-assembly method provides both the required structure control and a means to combine organic and inorganic materials. The basic

mechanism of this process, which was used for device manufacture in this work, and the properties of several types of self-assembled thin films are introduced in this section.

2.4.1 Self-assembly by electrostatic interaction

Alternating polyion adsorption

In 1992, Decher, Hong and Schmitt [112] reported on the fabrication of thin films by alternating adsorption of anionic and cationic polyions on charged surfaces. They measured the film thicknesses by small angle X-ray scattering and UV/vis absorption spectroscopy and observed linear increases of the thickness with the number of deposition cycles.

This method called layer-by-layer self-assembly relies on electrostatic attraction between a charged surface and oppositely charged particles in solution. The adsorption of monolayers of highly charged species like strong polyions on a charged surface leads to a reversal of the surface charge. The aggregation of more than a monolayer of a dissolved species on the surface is prevented by electrostatic repulsion. If the samples are alternatingly dipped into solutions with species of opposite charge, electrostatic attraction enables the sequential adsorption of multilayers of these charged species. Strong polyions are very effective, since all counterions are removed from their ionic groups in aqueous solution, leaving behind a high net charge on the molecule. Figure 2.24 shows the chemical structure of the anionic poly(sodium styrene sulfonate) (PSS) and the cationic poly(diallyldimethyl ammonium chloride) (PDAC), which have both been used for this process [40, 112–114].

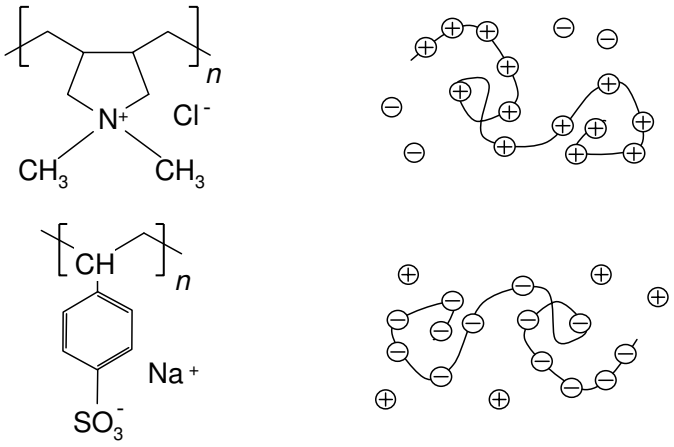

Figure 2.24: Chemical structures (left) and sketches of the charge distribution in solution (right) of PDAC (top) and PSS (bottom).

The layer-by-layer self-assembly method is applicable to a wide range of materials, as we will discuss below, and not restricted with respect to substrate size and morphology, since electrostatic interaction has the least steric demand of all chemical bonds [40, 41]. The complete process used for the sequential deposition of polyion layers is illustrated in Fig. 2.25. In the first step, a sample with a positively charged surface is immersed into a solution of negatively charged polyions, where it is left for some time to allow for a monolayer of polyions to form and to reverse the surface charge. The sample is then withdrawn and washed in pure water to remove excess solution. This step is necessary to avoid the contamination of subsequently visited baths. Then, the substrate is dipped into a solution of polyions with positive charge, where another layer forms and the charge is reversed again. After another washing step, the whole cycle can be repeated many times to fabricate films of arbitrary thickness [112].

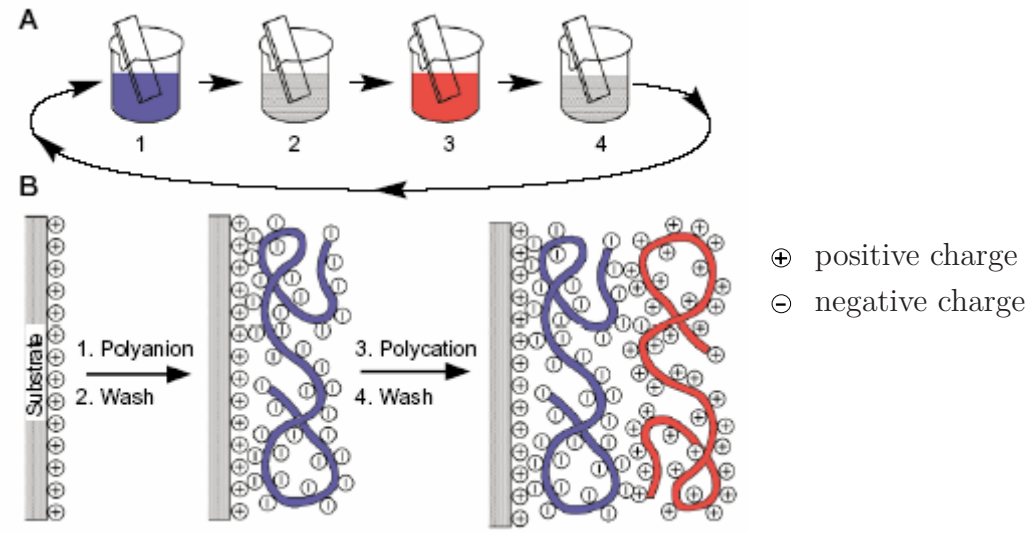

Figure 2.25: Solution based layer-by-layer self-assembly of oppositely charged polyions. Image taken from [40].

One should note that the excess charges of the polyions will be neutralized by adsorbed counterions from the solution after the substrate is withdrawn from the bath and also after the washing step, as indicated in the right images in Fig. 2.24. Otherwise, considerable electrostatic charge would be present on the sample. As soon as the sample is immersed into the next polyion solution, the counterions are dissolved and removed from the surface, forming a diffuse ion layer. Then, the exposed immobile charges of the deposited polyion layer are available to attract polyions of opposite charge by electrostatic forces.

Hybrid nanoparticle / polyion films

When certain metal oxide particles are put into acidic solutions, positive charges are induced on the particle surface. In basic solutions, the surface charge is negative [43]. Particles which show this behaviour are called amphoteric. Figure 2.26 displays amphoteric TiO_2 particles in aqueous solution at two different pH values.

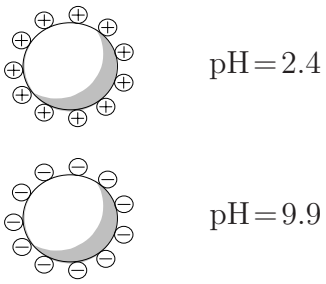

Figure 2.26: Amphoteric behaviour of TiO_2 particles in aqueous solution [43, 115].

Charges induced by amphoteric behaviour solubilize the particles in solution and lead to electrostatic interaction with charged surfaces. This effect enables the inclusion of SiO_2, TiO_2, and CeO_2 nanoparticles in layer-by-layer self-assembly processes [41]. Alternating deposition of charged nanoparticles and oppositely charged polyions produces multilayer structures consisting of both materials. The mass deposited during each cycle is higher for nanoparticles than for polyions, since they have a higher specific mass per amount of charge. Further, the material deposition depends on the degree of charge reversal induced by the preceding coating step, which is lower for charged nanoparticles than for polyions [40]. Coverages close to particle monolayers were observed, resulting in a film thickness control on the order of the particle diameters, i.e., of nanometers [40, 41, 43].

Schulze and Kirstein [115] monitored the film growth of TiO_2 nanoparticle / PSS films by measuring the absorption spectra of the individual layers by UV/vis transmission spectroscopy. They found spectral contributions from both PSS and the nanoparticles after the first deposition cycle, as well as a constant increase of the TiO_2 signal by additional nanoparticle / polyion dipping cycles. With respect to film composition, these findings indicate that both materials are incorporated into the films during the first cycle. The incorporation of polyions into thicker films, however, remained unclear.

The colloidal QDs described in Section 2.3.4 also carry charges, if the organic capping layer contains ionic groups. Therefore, they can be included in electrostatic self-assembly processes. Negatively charged cadmium sulfide and lead sulfide QDs with acidic cappings were shown to self-assemble into thin films with polycations as counter-

charges. The QDs preserved their unique optical properties [114], so that these hybrid films offer the opportunity to use QDs in optically functional coatings.

2.4.2 Applications

Functional coatings

It has been reported in the literature that layer-by-layer self-assembly was used to coat a variety of surfaces with different materials to obtain tailored functionalities for biological, medical, chemical and optical applications.

Proteins and DNA were incorporated into polyion multilayers, which may be applied as biosensors or in biotechnology [40]. Different kinds of surfaces have been functionalized by self-assembled hydrophilic nanoparticle / polyion films [116] and by biocompatible amino acid / polyion films [117], opening further opportunities for biological and also chemical applications.

In addition to flat surfaces, polyions were deposited layer by layer on spherical latex particles [118] and platelets [119]. These size tailored particles could be used as tunable light scattering materials or, in combination with bioactive materials, as microcarriers for target drug delivery.

Composite QD / polyion films were shown to yield optically functional coatings with tunable absorption [114] and photoluminescence properties [120] on transparent substrates. These self-assembled structures may be used as filters or light converters in optical applications.

Optoelectronic devices

Composite self-assembled films contacted by transparent electrodes can serve as active layers of optoelectronic devices. By incorporation of novel organic and inorganic light emitters and absorbers, the tailored optical properties of these materials can be accessed for device applications. Following this approach, composite films of CdTe QDs / polyions [121] and J-aggregates / conductive polymers [122] were grown using layer-by-layer self-assembly. The unique electroluminescence properties of the constituent materials produced light-emitting diodes with new characteristics.

Photovoltaic devices which were based on films grown with the layer-by-layer process have been fabricated recently. Agrios et al. [42] and He et al. [43] used self-assembled

TiO_2 nanoparticle / polyion films as nanoporous structures for DSSCs. Scattering layers grown on top as well as sintering to improve particle connectivity were shown to increase efficiency, which, however, remained below the best DSSCs reported so far. Films grown with negatively charged TiO_2 particles and PDAC were more efficient than films with positively charged TiO_2 and PSS. Light-absorbing species were not incorporated into the films directly during the layer-by-layer growth, therefore, the TiO_2 structure was sensitized with dye after the self-assembly process.

In the present work, we fabricate films with extended functionalities by incorporating different types of organic and inorganic sensitizer materials during the film growth. We analyze the structural properties of the hybrid films and use them as active layers in excitonic photovoltaic cells. Chapter 3 contains the materials and methods we used for the experiments. The results of structural and electronic characterizations will be described in the Chapters 4, 5, and 6.

Chapter 3

Materials and methods

3.1 Materials

This section describes the materials which were used for the fabrication and characterization of thin films and hybrid electronic devices. It includes the results of size distribution measurements of TiO_2 nanoparticles which we carried out with transmission electron microscopy.

3.1.1 Sample substrate types

The substrates we used in this work were glass slides, either bare or precoated with transparent conductive oxide (TCO) layers. They were cleaned using cleaning procedures described in Section 3.2.1. The uncoated slides were standard microscope glass slides or fused silica slides transparent in the UV obtained from Präzisions Glas & Optik GmbH, Iserlohn. Glass slides coated with indium tin oxide (ITO) were also obtained from Präzisions Glas & Optik, glass slides coated with fluorine-doped tin oxide (FTO) were a donation from Nippon Sheet Glass, Tokyo. All slides had been cut to dimensions of 12 mm × 35–40 mm and were 1–3 mm thick, so that they fit into our automated dipping machine described in Section 3.2.2.

3.1.2 Molecules and nanoparticles

Polymers, organic dyes and colloidal nanoparticles

All polymers and dye molecules were obtained from commercial suppliers and used without further treatment. Colloidal QDs were obtained from collaboration partners and also used without any further treatment. The Tables 3.1 and 3.2 list the chemical structures, names, and sources of polymers, organic dye molecules, and inorganic colloidal nanoparticles we used for thin film self-assembly, for characterization experiments, and for device fabrication.

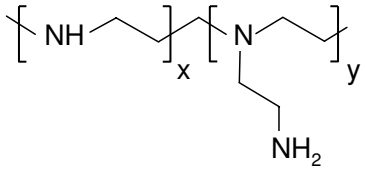	poly(ethylene imine) (PEI) Aldrich m.w. 55K
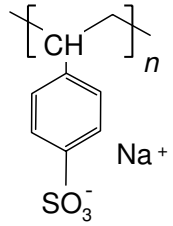	poly(sodium styrene sulfonate) (PSS) Aldrich m.w. 70K
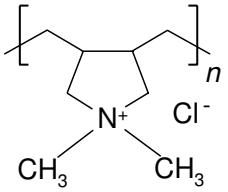	poly(diallyldimethyl ammonium chloride) (PDAC) Aldrich m.w. 400K–500K
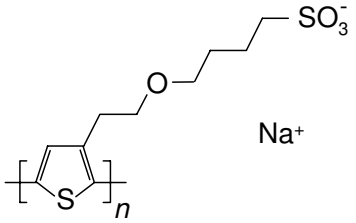	poly(2-(3-thienyl)-ethoxy-4-butylsulfonate) sodium salt (PTEBS) American Dye Source m.w. 100K–1000K
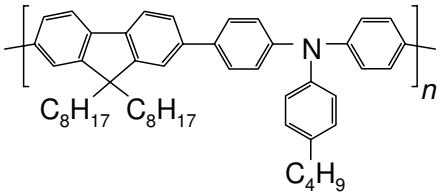	poly(9,9'-dioctylfluorene-*co*-*N*-(4-butylphenyl) diphenylamine) (TFB) American Dye Source m.w. 50K–100K

Table 3.1: Chemical structure of polymers used in thin films and devices.

In the following, we describe the processing of the polymers listed in Table 3.1. Aqueous solutions of the polyions PEI, PSS, and PDAC were prepared using de-ionized water

with a resistance of 18 MΩ (DI-water). The solutions with a concentration of 10^{-2} M were used in the self-assembly process described in the next section. Further, we prepared acidic buffer solutions with pH = 2.0 from DI-water and small amounts of citrate received from Dechant, also for the self-assembly process.

We dissolved the conjugated polyion PTEBS in DI-water at a concentration of 1.0 wt. %. The solubility of PTEBS in water is greatly enhanced by the addition of ammonium hydroxide, probably because the solution pH and the degree of ionization of the sulfonate groups is affected by this additive [83]. Dimethylformamide reportedly also has this effect [38]. We found that an addition of 3 wt. % ammonia to the solution slightly changed its color to a darker red, indicating better dissolution. Solutions with added ammonia were used in the self-assembly process and for drop-casting solid PTEBS films on top of nanoparticulate TiO_2 films, as described in Section 5.2.2. PTEBS solutions with ammonia concentrations below 3 wt. % did not yield good device characteristics in terms of measured photocurrents and photovoltage. Therefore, PTEBS solutions with 3 wt. % ammonia were used for the experiments, which we report in Chapter 5. There, a comprehensive description of the optical and electronic properties of the molecule is given.

The copolymer TFB was processed from a tetrahydrofurane (THF) solution with a concentration of 1.0 wt. %. We used the solution to drop-cast solid TFB films on top of sensitized TiO_2 films. The electronic properties of this hole conducting polymer are described in Chapter 6.

We used various dyes listed in Table 3.2 for surface adsorption experiments. We processed them from solutions with the following solvents and concentrations. The anionic dye fluorescein was dissolved at a concentration of 1 mM in an aqueous solution with a pH of 9.9, containing 0.5 mM of both Na_2CO_3 and $NaHCO_3$, which we obtained from Aldrich. The metal complex dye Ru535 was dissolved in ethanol at a concentration of 0.24 mM, and the cationic dye Rhod6G was dissolved in isopropanol at a concentration of 1 mM.

Colloidal QDs with II-VI semiconductor crystal cores (CdSe or CdTe) and a TGA capping, which are also listed in Table 3.2, were incorporated into thin films as sensitizers. TGA, in contrast to the TOPO capping shown in Fig. 2.20, binds covalently to Cd on the crystal surface. The carboxyl end group of TGA is charged negative in aqueous solution, so that the QDs could be used in the self-assembly process which is based on electrostatic interactions. The dots were synthesized by collaboration partners at Max Planck Institute of Colloids and Interfaces, Potsdam, using wet chemical routes [123–126]. We processed them from aqueous solutions with particle concentrations of

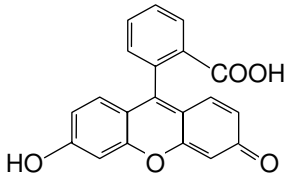	fluorescein Aldrich
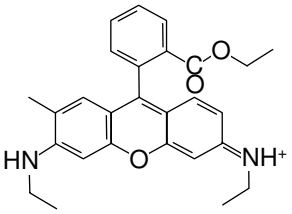	rhodamine 6G (Rhod6G) Aldrich
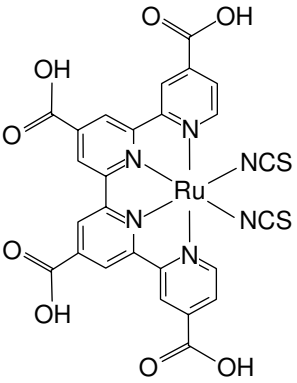	*cis*-bis(isothiocyanato)- bis(2,2'-bipyridyl-4,4'-dicarboxylato)- ruthenium(II) (Ru535) Solaronix
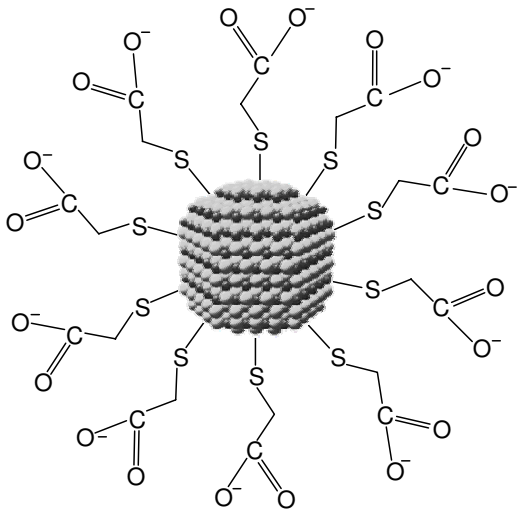	CdX nanocrystals (X=Se with ∅ 3.0 nm, X=Te with ∅ 3.8 nm), with thioglycolic acid (TGA) capping Max Planck Institute of Colloids and Interfaces

Table 3.2: Chemical structures of organic dyes and colloidal nanocrystals.

approximately 8×10^{-5} M (CdSe) and 5×10^{-5} M (CdTe). The electronic properties of the dots will be discussed in Chapter 6.

TiO_2 nanoparticles

The TiO_2 nanoparticles used in this work were obtained from Alfa Aesar as a white powder. The manufacturer gives a mean diameter of 40 nm, a specific surface area of 38 m^2/g and claims 99.9% anatase crystal phase. The amphoteric behaviour of the particles results in stable aqueous suspensions in acidic and in basic solution. Particles were added in a concentration of 2 g/l either to aqueous solutions containing 0.5 mM of both Na_2CO_3 and $NaHCO_3$ with a resulting pH of 9.9, or they were added to DI-water and the pH adjusted to 2.4 by titration with hydrochloric acid (25% in water). Basic and acidic suspensions were used in the layer-by-layer self-assembly process.

We deposited individual TiO_2 nanoparticles from a basic suspension on a copper mesh coated with Formvar, so that we could image them with a transmission electron microscope (TEM). Figure 3.1 displays two images we obtained from these measurements, showing exclusively spherical particles. The finding of this shape confirms the predominantly anatase crystal phase of the particles.

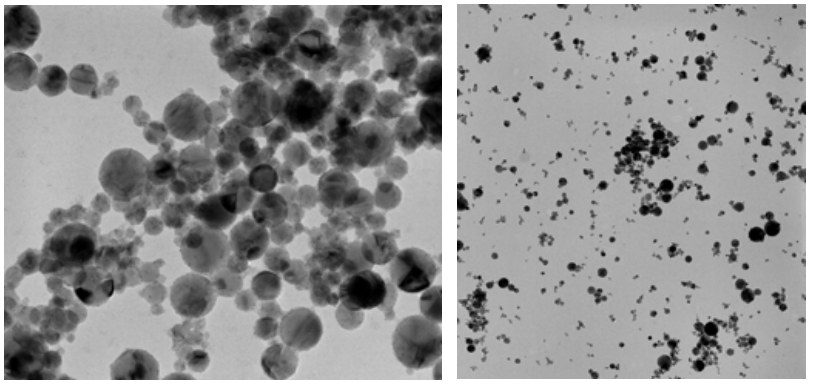

Figure 3.1: TEM images of TiO_2 nanoparticles at different magnifications.

2407 detectable particles in the images in Fig. 3.1 were measured individually and included in an analysis of the distribution of particle diameters. The measured diameters were grouped into 1 nm wide classes and yielded a very broad and highly asymmetric size distribution with a median diameter of 14.8 nm, as displayed in Fig. 3.2. The arithmetic mean of the measured diameters was 19.9 nm, while the average measured volume corresponded to a diameter of 31.3 nm.

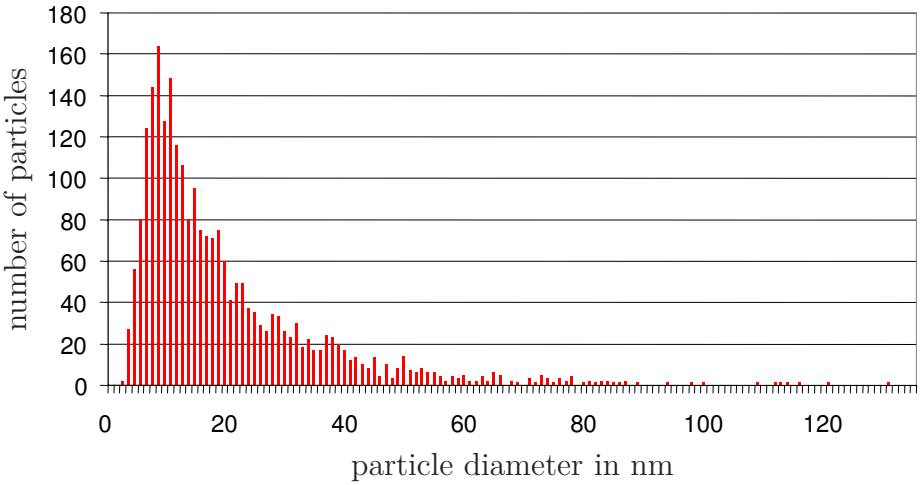

Figure 3.2: Size distribution of TiO_2 particles obtained from the images in Fig. 3.1.

Very few particles with diameters less than 4 nm were found. The size of the smallest particles is an important feature of the distribution, since they determine the pore size in a porous assembly.[1] It cannot be ruled out that some of the smallest particles were missed because they could not be detected visually, however, we assume that their number is small. We expect that the pore sizes in a porous assembly are determined by particles with diameters of 8–10 nm, owing to the small fraction of particles with smaller sizes.

3.2 Methods

In this section, the methods and instruments we used for the fabrication and characterization of thin films and electronic devices are described. Special methods used for device processing, such as polymer capping layer and top electrode fabrication, are described in the Chapters 5 and 6.

3.2.1 Substrate cleaning and compact TiO_2 coatings

Cleaning procedures

The cleaning procedure is designed to remove all surface contaminants and to create surface charges on the substrates, which are required to initiate the self-assembly process. The procedure consists of manual cleaning and two chemical cleaning steps, the

[1] Pores formed by big particles can be filled by small particles and thus reduced in size.

latter of which induces surface charges. All faces of the slides were cleaned to make sure that they do not contaminate the solutions used in the dipping process. Such contamination would result in the precipitation of the dissolved content, stopping the layer-by-layer build-up process. DI-water was used throughout the cleaning procedure.

At first, all slides were manually cleaned by thoroughly rubbing them in a water bath with dishwashing detergent using Nitril gloves, and subsequently rinsing them in DI-water. The manual cleaning proved to be a critical step: When manual cleaning failed to produce sufficiently clean surfaces, the following chemical cleaning was futile and no functional substrates were obtained.

The chemical cleaning was different for TCO coated and uncoated substrates owing to the tendency of TCO coatings to dissolve in acidic baths. Bare glass or fused silica slides were left overnight in a mixture of sulfuric acid and hydrogen peroxide (volume ration 1:1, 'piranha solution'). This extremely acidic solution quickly dissolved any oxide coatings, so that TCO coated substrates had to be cleaned in a sequence of less aggressive organic baths. Dried TCO coated substrates were immersed for 3 min in six subsequent baths, two each of chloroform, acetone, and 2-propanol. The baths were heated to 60°C and placed in an ultrasonicator to intensify the dissolution of dirt. After this cleaning step, the substrates were rinsed in DI-water. When the substrates were stored therein, they remained clean for several weeks.

The third and surface charge inducing step had to be executed within 48 hrs before the start of the self-assembly process. It was identical for all substrate types and is referred to as the 'RCA method' in the literature [127]. Samples were immersed in a mixture of DI-water, ammonium hydroxide (30 wt. % ammonia in water), and hydrogen peroxide (30 wt. % in water) in a volume ratio of 5:1:1. First, DI-water and ammonium hydroxide were mixed and heated to 80°C in a water bath, then the substrates and cooled hydrogen peroxide were added so that a temperature of 72–75°C established. Samples remained immersed for 10 min while the temperature was kept constant. Gas bubbles forming on the surfaces were shaken off repeatedly to ensure continuous exposure of the samples to the bath. After the RCA cleaning procedure, the substrates were thoroughly rinsed with DI-water once again and stored therein until they were processed further. The successful creation of surface charges resulted in highly hydrophilic surfaces.

Fabrication of compact TiO_2 coatings

We used a sol-gel dip-coating process described by Fan et al. to fabricate compact TiO_2 thin films on FTO coated substrates [85]. Methods based on spin-coating [128, 129]

did not yield the desired results, as SEM images revealed that the substrates were not homogeneously covered. We prepared a sol by mixing titanium isopropoxide (99.5% purity) with ethanol (99.9% purity) and acetic acid (99.9% purity) while vigorously stirring with a magnetic stirrer. All chemicals were obtained from Aldrich and used as received. Cleaned FTO substrates were dipped into the sol using a dipping robot from Riegler&Kirstein GmbH, Potsdam, and withdrawn slowly so that a gel film formed. Using the robot offered precise control of the withdrawal speed, which turned out to be crucial for the quality of the films and was set at 20 mm/min. The samples were dried in a nitrogen flow after the dip. The whole process was repeated one time in order to ensure a complete coverage.

The samples were then annealed at 550°C to obtain a TiO_2 film with an anatase crystal structure. A slow ramping of the temperature during heating and cooling is essential to allow the forming TiO_2 film to adapt to the mechanical stress induced by the temperature change without producing cracks, which destroy the functionality of the film [85, 129]. We increased the temperature at a rate of 1°C/min, kept the temperature constant at 550°C for 30 min, and then decreased it at a rate of 0.5°C/min. For a precise stabilization and control of the temperature, an oxidation oven with a quartz glass chamber surrounded by a heater coil was equipped with a thermocouple connected to a Model 6100 PID temperature controller by West Instruments. The device featured automated adjustment to the system inertia parameters and produced highly stable temperatures inside the chamber. We observed no substantial reduction of the conductivity of the underlying FTO by the annealing.

In order to contact the front electrode of the device, it is necessary to leave parts of the FTO layer uncovered of TiO_2. Such a structure was achieved by covering areas of FTO with a protective foil during the dip-coating process. We used a foil which could be removed easily without any residues. We also attempted to remove parts of the TiO_2 film *after* completing the sol-gel process by etching. The RCA bath described above was employed as an etchant, and areas which had to remain covered with TiO_2 were protected by adhesive tape. This latter method, however, proved less practical because the cleaning process had to be repeated after removing the adhesive tape. Samples coated with compact TiO_2 showed good hydrophilicity after annealing and were only briefly immersed into the RCA bath to enhance this property for the subsequent self-assembly process while leaving the compact TiO_2 film intact.

3.2.2 Layer-by-layer self-assembly

Production equipment

Layer-by-layer self-assembly processes can be induced by sequences of dips of a hydrophilic substrate into aqueous solutions of charged particles and polymers, as described in Section 2.4. We executed these processes in a cleanroom environment using a dipping system based on a Riegler&Kirstein robot, the workbench of which is shown in Fig. 3.3. The system was equipped with a rinse cascade with a controlled DI-water supply (1 in Fig. 3.3) and a drying stage with a nitrogen supply (2). Several containers with solutions of QDs or polymers (3) as well as a TiO_2 suspension placed in an ultrasonic bath (4) were used for dip-coating. During self-assembly processes, the ultrasonic bath was switched on for 1 min in regular intervals in order to avoid particle precipitation. It remained switched off while samples were immersed in the TiO_2 suspension. Glass slides were held by teflon sample holders (5) and positioned in solutions, rinsed, and dried by moving the robot arm in three dimensions with stepping motors. Sequences of movements with controlled dipping speeds, withdrawal speeds, and immersion times were programmed using the robot software running on a MS-DOS PC and repeated an arbitrary number of times.

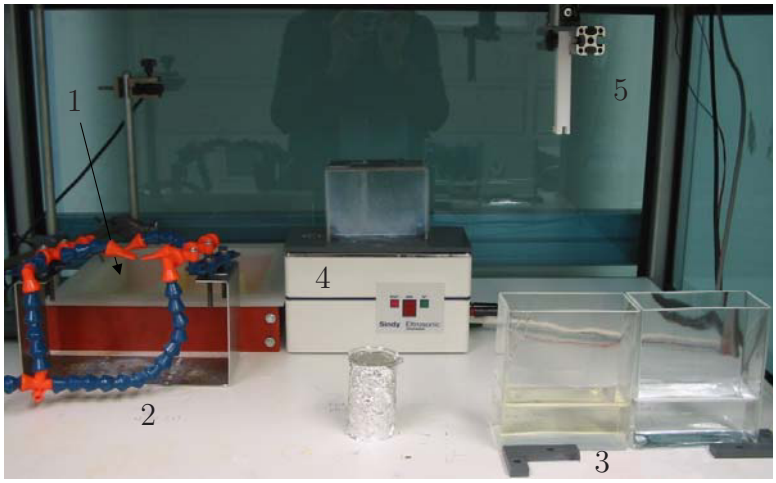

Figure 3.3: Work bench of the robotic dipping system. (1) rinsing stage, (2) drying stage, (3) polymer solution containers, (4) ultrasonic bath, and (5) sample holder.

It turned out during our experiments that the quality of the grown films crucially depends on the completeness and speed of the drying process. The drying method and hardware were designed to quickly blow off remaining water from the faces of the slide. This approach proved more appropriate than slowly blowing the samples dry by enhancing solvent evaporation. The advantage of the former method is that dissolved

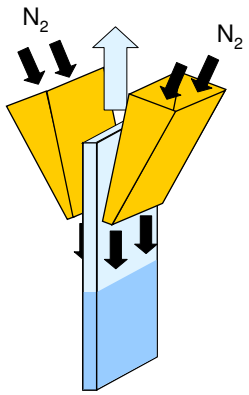

Figure 3.4: N_2 stream (black arrows) through plastic nozzles (top left and right) used for rapid drying of sample slides (middle, blue arrow: sample movement during drying).

particles and molecules will be removed instead of settling down on the sample surface as the solvent evaporates.

Figure 3.4 schematically shows two nozzles (yellow, top left and right) obtained from Lockwood Products, Lake Oswego (OR), that were used for drying the samples with a stream of nitrogen. With the N_2 supply off, a glass sample (light blue, middle) was inserted between the two nozzles until the wet part of the sample was below the nozzles. Then, the N_2 supply was turned on and the slide was moved upwards through the gap, so that all water was blown off the slide faces. The process was repeated three times to ensure a complete drying. The actual angle between the sample surface and the nozzles, see (2) in Fig. 3.3, was larger than the one shown in the sketch in Fig. 3.4.

Basic process sequence and coating protocols

The layer-by-layer self-assembly processes used for this work followed a protocol reported in the literature [43, 115]. All layers were prepared by dipping charged samples into solutions containing oppositely charged species. The first two or three dips were for longer times to ensure a complete coverage. After that, shorter dips into baths containing species with opposite charge were repeated alternatingly until the desired layer thickness was achieved. Unless noted otherwise, every dip was followed by rinsing in DI-water and drying in a flow of nitrogen, using the equipment and methods described above.

The amphoteric behaviour of TiO_2 particles allows to grow composite films in combination with polyions charged either positive or negative, and also the use of charge reversing solutions. After hydrophilization, all substrates were first dipped into a

solution of PEI polymer for 5 min. The next steps were alternating dips into a TiO_2 nanoparticle suspension and either an acidic buffer solution (sample type A described below), PSS polyanion (sample type B) or PDAC polycation (sample type C). All dips before and including the first dip into the nanoparticle suspension were for 5 min in order to ensure the formation of complete monolayers. For all subsequent dips, the dipping time was reduced to 1 min, so that the time necessary to produce thick films was decreased by a factor of 5–10 compared to the times reported in other publications [41, 43, 115]. Three types of samples using different material combinations are described in the following:

Sample type A was grown by alternate dipping into a basic suspension of TiO_2 particles, with negative charges, and a buffer solution with $pH = 2$, which reversed the charges of the TiO_2 particles to positive. The first dip after PEI was into the TiO_2 suspension for 5 min, all subsequent dips were for 1 min.

Sample type B was grown using an acidic TiO_2 suspension inducing positive charges and a PSS solution. The first dips after PEI were into PSS and then into the TiO_2 suspension, both for 5 min. All subsequent dips were for 1 min.

Sample type C was fabricated with a protocol which is equivalent to the sample type A protocol, but instead of the buffer solution we used a solution of PDAC.

The structural characterization of these three types of samples will be described in Chapter 4. Samples containing light sensitive materials were grown using variations of the above protocols and will be characterized in the subsequent Chapters 5 and 6:

PTEBS samples were grown with a protocol equivalent to the type B protocol. The dips into PSS solutions were replaced by dips into PTEBS solutions. All other dips remained unchanged.

QD sensitized samples were fabricated using a variation of the type C protocol. After dipping into a basic TiO_2 suspension and into PDAC, samples were dipped into a QD solution for 1 min, which contained either CdSe or CdTe QDs with negatively charged capping layers. Subsequently they were dipped again into PDAC, so that the process sequence was $TiO_2 \rightarrow$ PDAC $\rightarrow$ QDs $\rightarrow$ PDAC $\rightarrow \ldots$ After every dipping step, the samples were rinsed in water and then dried, except for the QD solution, after which samples were dried first, then rinsed, and then dried again.

Attempts to grow films without polyions using negatively charged QDs and positively charged TiO_2 nanoparticles in acidic solution were not successful.

In the following, one 'dipping cycle' refers to the process sequence which includes one dip into TiO_2. For all sample types, samples were grown with different thicknesses by repeating the dipping cycles a different number of times, with a maximum of 120 cycles.

3.2.3 Structure characterization

X-ray photoelectron spectroscopy

We analyzed the surface composition of layer-by-layer grown films with X-ray photoelectron spectroscopy (XPS). We introduced the samples in an Omicron UHV chamber with a base pressure of 2×10^{-11} mbar where they were irradiated with Al and Mg $K_{\alpha 1/2}$ radiation. The kinetic energy spectra of emitted photoelectrons were recorded with a hemispherical analyzer (PHOIBOS 100) at a pass energy of 20 eV. No sample charging or beam damage was observed.

The kinetic energy E_{kin} of a photoelectron emitted upon X-ray excitation is given by $E_{\text{kin}} = h\nu - E_{\text{bind}}$, where $h\nu$ is the energy of the X-ray source and E_{bind} is the binding energy of the electron. E_{bind} is specific for atomic levels and experiences slight shifts by the chemical environment of the emitting atom. Therefore, one can determine the atomic and chemical composition of a surface irradiated by a monochromatic X-ray source from the spectrum of the kinetic energies of the emitted photoelectrons [130]. XPS is surface sensitive because the depths from where photoelectrons can escape without losing kinetic energy by inelastic scattering are generally on the order of 0.5–2.0 nm in metals and less than 10 nm in organic matter for typical kinetic energies [131]. When photoelectrons lose kinetic energy by scattering, their source can no longer be identified.

Scanning electron microscopy, atomic force microscopy and profilometry

We investigated the morphology of sample surfaces using scanning electron microscopy (SEM) and atomic force microscopy (AFM). One-dimensional height profiles and film thicknesses were determined by AFM and with a profilometer.

For SEM, samples are introduced into a vacuum chamber and a focused beam of high energy electrons is scanned across the sample surface. The beam leads to the emission of secondary electrons, with the magnitude of the current depending on the surface morphology. The current is recorded for each scanning spot and converted into an image of the sample surface. The SEM instruments we used were a JEOL JSM-840A at 30 kV electrode voltage and a JEOL JSM-T300 at 20 kV.

The AFM system we used consisted of a Veeco Instruments Multimode AFM with a Nanoscope IV controller operating in tapping mode. In this setup, a vibrating tip with a typical radius of 20 nm is positioned within the range of atomic forces above the surface of a sample. When it is scanned across the surface, the height profile of the sample determines the distance between tip and surface and thus the forces acting upon the tip. These forces dampen the tip vibration and can thus be measured, so that a two-dimensional surface height profile can be recorded. Vertical positioning and lateral scanning is performed by piezoelectric elements.

We used an Ambios XP-1 stylus profilometer for one-dimensional surface profile measurements. This instrument presses a stylus onto a sample with a weak force on the order of 10^{-6} N and scans the stylus along a straight line. The stylus follows the surface morphology so that a one-dimensional height profile can be recorded. This technique is not well suited for samples with very soft or fragile surfaces.

3.2.4 Optical and electronic characterization

Absorption in solution

Absorption spectra were recorded using a Shimadzu UV-2101 PC spectral photometer at 1 nm slit width. The solutions and the clean solvent were filled into two separate 10 mm wide quartz cuvettes. These were placed in two parallel light beams, so that optical absorption by the solvent and the cuvettes was eliminated from the recorded absorption signal.

I/V curve measurements

For the measurements of I/V curves, samples were placed in test fixtures, contacted with gold wires, and illuminated with white light through the transparent front electrode. We used voltmeters and combined ammeter/voltage source units which were controlled by PCs running LabView under Microsoft Windows. The measurements were conducted with two different setups at the Institute of Physics at Humboldt University (HU) in Berlin and at the Energy Conversion Systems Lab at Virginia Commonwealth University (VCU) in Richmond (VA). The LabView software was written specifically for these measurements and allowed for time-resolved current and voltage recordings with a resolution on the order of 1 sec.

We used a Keithley 487 picoammeter/voltage source and an additional Keithley 2000

multimeter with a resistance of 10 MΩ for independent four point voltage measurements at HU, see Fig. 3.5. The samples were held by a test fixture with the back electrodes facing up. The back electrode and exposed parts of the front electrode could be contacted by micrometer screw adjusted gold wires from the top. Underneath the sample we placed a standard mirror at a 45° angle, so that the sample could be illuminated by a light source placed to its left. For the illumination, we used Solux bulbs with modulated color temperatures of 4700K. We measured their intensity with a photometer and placed them at a distance of 40 cm, so that the power density incident on the sample surface was 100 mW/cm^2. The right image in Fig. 3.6 shows the test fixture with a contacted sample.

Figure 3.5: HU measurement setup with (from left to right) picoammeter/voltage source and multimeter, sample fixture, PC control unit.

Most photoelectronic measurements were conducted at VCU, where we used a Spectra-Physics Solar Simulator equipped with a fiber optic as a light-source. A home-built positioning fixture was adapted to our sample sizes and held these upright, so that they could be illuminated from one side through the front electrode while the back electrode was contacted from the other side. The front electrode was contacted using metal clamps in a way that no shadow was cast on the devices. For back electrode contact, the setup was equipped with a gold wire spring which could compensate the vibrations of the setup mechanically. The setup kept the wire spring contact and the defocused light beam from the fiber optic in a fixed position. Using two positioning knobs of the fixture, the sample was moved relative to that position, so that the devices could be contacted individually without disassembling the setup. After intensity calibration using a photometer, the fiber optic was positioned in such a way that the power density illuminating the devices was 100 mW/cm^2. The left image in Fig. 3.6 shows the positioning fixture with an

acrylic glass sample holder holding one sample. Behind the sample, the exit lens of the fiber optic is visible. In front of the sample, an adjustable arm holds the wire spring contact.

Figure 3.6: Left: VCU sample fixture with fiber optic illuminator, right: HU sample fixture with illumination mirror underneath the sample.

Spectral photocurrent measurements

We used a Perkin Elmer LS 50 scanning fluorescence spectrometer equipped with a xenon lamp as a monochromatic light source to analyze the spectral behaviour of our cells. The spectral light intensity was determined with a Hamamatsu S1226-BQ UV photodiode. The photocurrent of the cells was measured in open circuit condition while the cells were held and contacted by the fixture shown in the right image of Fig. 3.6.

Chapter 4

Structure of self-assembled TiO_2 / polyion heterofilms

4.1 Outline

Nanostructured thin films are grown from suspensions of TiO_2 nanoparticles in combination with polyion solutions or charge reversing baths, using the layer-by-layer self-assembly method described in the preceding chapter. We report the results of the structural characterization of type A, B, and C samples with respect to morphology, composition, and internal structure. The focus of these characterizations is on the application of the self-assembled films as active electrodes in hybrid photovoltaic devices. A discussion of our findings with respect to device applications will conclude this chapter.

4.2 Characterization results and discussion

4.2.1 Film morphology and thickness

Macroscopic film quality

From all three dip-coating protocols A, B, and C defined in Section 3.2.2, we obtained samples which were uniformly coated on a macroscopic level. The results did not depend on which of the substrate types listed in Section 3.1.1 was used, as long as the cleaning process described in Section 3.2.1 was successful. Different sample types displayed very

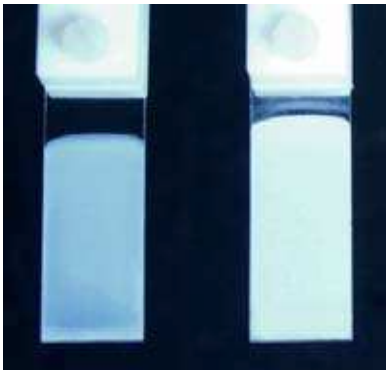

Figure 4.1: Samples coated with 60 dipping cycles using PSS (type B, left) and PDAC (type C, right).

different opacities after the coating process, with type C samples being the most opaque, followed by the types B and A. As an example, Fig. 4.1 shows one sample of type B and one of type C, each of which has been coated by 60 dipping cycles on both faces.

Film surface structures

We investigated the thickness of the coatings and the surface morphology, both of which are important features of photovoltaic cells, using SEM and AFM. Figure 4.2 shows the SEM images, which reveal that the surface structures differ in such a way that the different opacities mentioned above can be explained by the light scattering properties of the films.

Sample type A (top images in Fig. 4.2) has the smoothest surface structure, with a small number of aggregates larger than 100 nm on a rather flat surface. The surface of sample type B (middle) is rougher, with a higher density of aggregates with larger size. Sample type C looks much different, it is entirely composed of aggregates of sizes in the range of one micrometer. This size makes them efficient scattering centers for visible light [70]. As noted in Chapter 2, this is an important finding, since it has been shown that scattering centers can increase the performance of nanocrystalline solar cells [69, 70]. Further, He et al. [43] investigated DSSCs with layer-by-layer grown electrodes and found higher efficiencies for electrodes fabricated with PDAC than for electrodes fabricated with PSS. This finding can be explained by the different morphologies and light scattering properties of the film surface.

We repeated the coating experiments with the same monomeric concentrations of PDAC and PSS in solution, but with different polymer molecular weights and with NaCl added in different concentrations from 1 M to 3 M. In this range, where electrostatic interac-

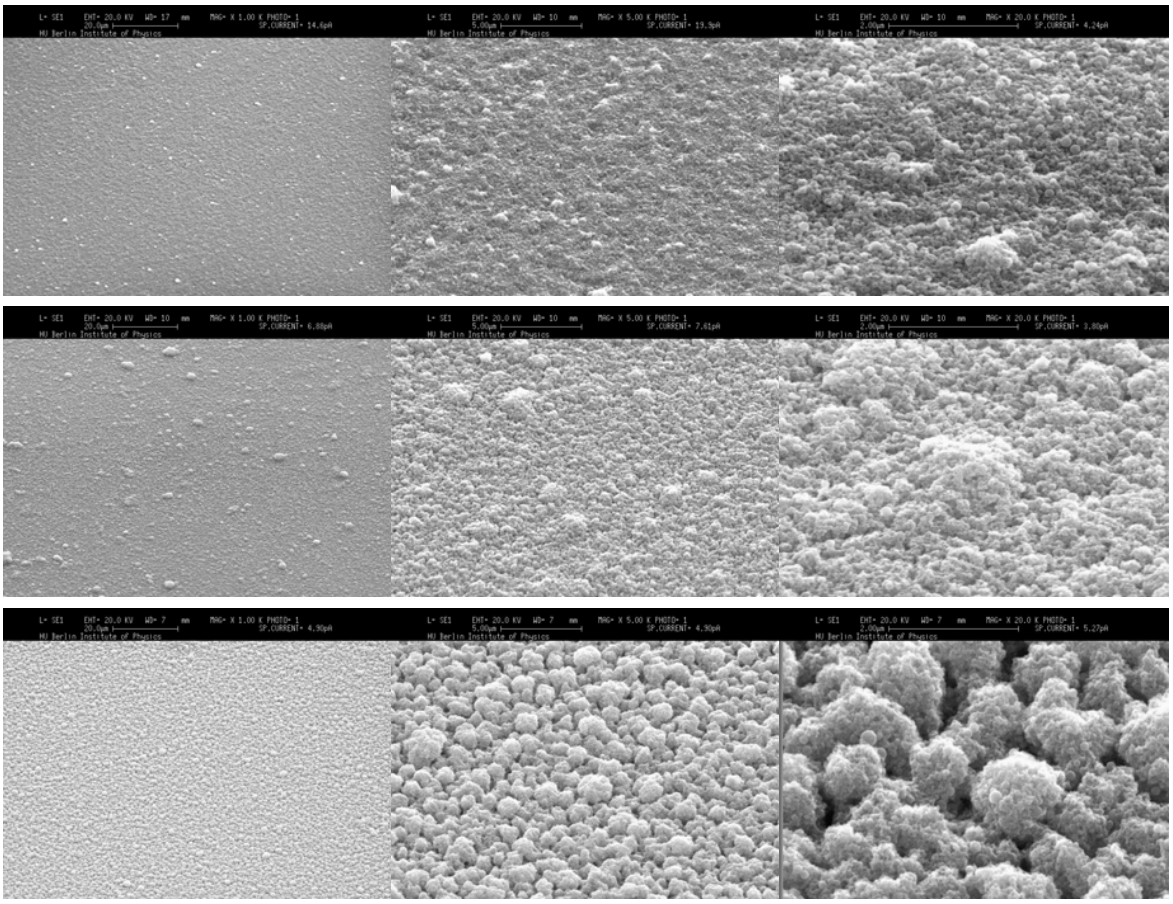

Figure 4.2: SEM images of samples of type A (top), type B (middle), and type C (bottom), revealing different surface structures. The scan areas are $120\,\mu\text{m} \times 80\,\mu\text{m}$ (left, 1k magnification), $24\,\mu\text{m} \times 16\,\mu\text{m}$ (middle, 5k), and $6\,\mu\text{m} \times 4\,\mu\text{m}$ (right, 20k).

tions are screened on the length scale of Na^+ ion radii, ionic strength has been shown to strongly affect the adsorption behaviour of polyions [132, 133]. Other contributions also reported a dependence of adsorption behaviour on ionic strength [40, 41, 117], but exceptions have also been found, see [134] and references therein. Since the chemical structure of the polyions affected the surface morphology of our layer-by-layer grown thin films, a change in conformation or adsorption behaviour was also expected to influence the film growth and yield different morphologies. The film morphologies we obtained, however, did not show any difference compared to the ones obtained without adding any salt. Different molecular weights gave no changes, either.

The origin of the aggregates found on type C samples could be aggregation of nanoparticles *in solution*. However, two results contradict that hypothesis. First, type A samples, which were prepared from the same TiO_2 nanoparticle solution, show a much smaller number of aggregates per area. Second, AFM images of type C samples coated with only one dip into the nanoparticle suspension display individual particles, as shown in

Fig. 4.3, but no aggregates. Therefore, we conclude that the aggregates grow layer-by-layer during the dip-coating process.

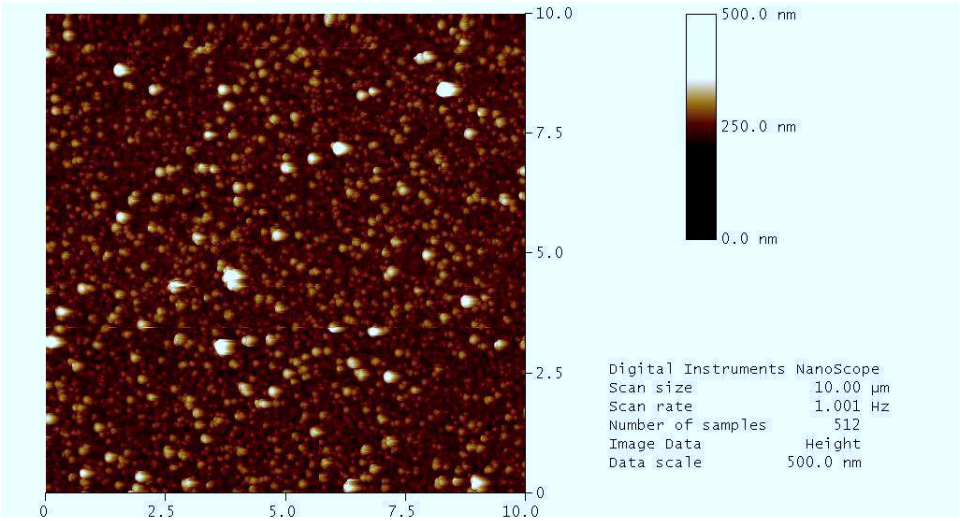

Figure 4.3: TiO_2 nanoparticles deposited on glass by dip-coating.

Film thickness measurements by AFM

The film thickness was determined by scratching off a thin line of the film with a razor blade or toothpick and recording the height image of the resulting step on a $100 \times 100\,\mu m^2$ area by AFM. Figure 4.4 shows the averaged AFM height profile perpendicular to the scratch and the height image of a $1.78\,\mu m$ thick type C sample as an example.

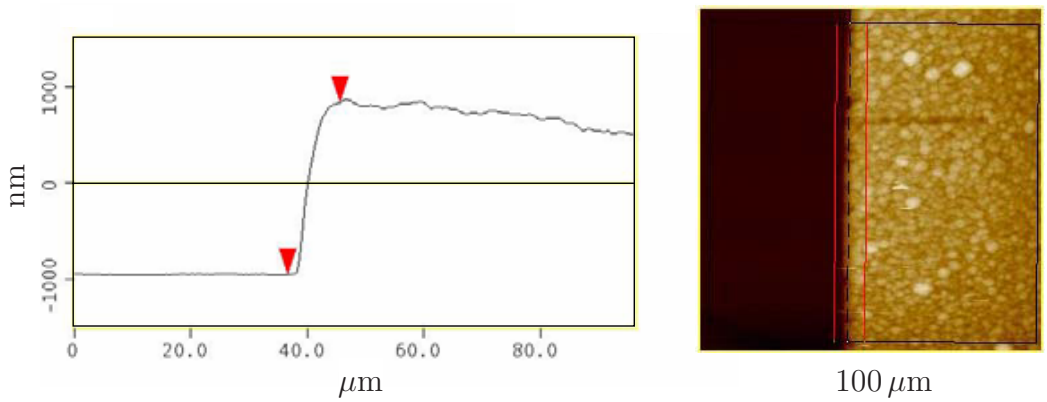

Figure 4.4: AFM averaged height profile (left) and image (right, black rectangle marks the averaging area) of a type C sample (60 dipping cycles) with a scratch exposing the glass substrate (left part of images).

We checked for scanning damages caused by the AFM tip by subsequent imaging of the height measurement site with an optical microscope and a CCD camera. We observed that for thick samples coated with more than 100 dipping cycles, the surface had frequently been scratched by the tip, even though no traces of such behaviour were visible in the recorded AFM image. Such measurements were excluded from the analysis. For the sample types B and C, we observed a linear growth of the film thickness with the number of dipping cycles, as has been reported elsewhere for these types of films [43, 115]. The growth rates were 24.0 nm/dipping cycle for type B, and 24.4 nm/dipping cycle for type C, which is on the order of the average TiO_2 particle diameter. For type A samples, no reproducible linear growth was observed. The typical thickness of a sample after 50 deposition cycles was 500 nm, corresponding to an increase of 10 nm/cycle, which is less than the nanoparticle diameter.

The more regular growth and the higher growth rates of the TiO_2 / polyion protocols compared to the buffer solution protocol indicate that the polyions play a crucial role in the layer-by-layer self-assembly process. Apparently, efficient charge reversal on the sample surface induced by the high charge density of adsorbing polyions is a prerequisite for a sustained regular layer-by-layer growth.

4.2.2 Film composition

Since the amount of polymer in the films cannot be determined with either of the microscopy methods described in the preceding section, we investigated the film composition with XPS.

We used sets of type B and C samples grown on ITO substrates. Each set contained seven samples coated by the first, the first two, up to the first seven steps of the corresponding protocol, as well as a pair of thick samples precoated with 60 cycles, one of them with one additional polyion coating. We took the XPS signal from the core levels of specific atoms to identify the source as either the polymer, TiO_2, or bare ITO substrate. The latter two were reliably detected by the signals of the Ti 2p core level (TiO_2) and In 3d core level (ITO substrate). The detection of PDAC polymer (type C samples) proved difficult, because the signals of carbon and nitrogen are both compromised by contaminations deposited on the sample surfaces in ambient air. The presence of these contaminations showed in significant carbon and nitrogen signals from samples which are not expected to contain these elements, like, e.g., bare ITO substrates. The detection of PSS in type B samples was more reliable because the S 2p signature can be measured without any interference from contaminations.

As explained in Section 3.2.3, only photoelectrons excited within the escape depth contribute to the XPS core level signals. Since the mean escape depth of TiO_2 is 2.1 nm, the recorded XPS signal stems from a surface layer which is a few nanometers wide [135]. Nevertheless, we consider XPS an appropriate method for the determination of the bulk composition of the thin films: Since the films are grown layer by layer, we expect the composition of deep lying parts of the film to be very similar to the composition close to the surface.

At certain kinetic energies E_i^{kin}, the recorded count rate of photoelectrons belongs to a core level of a specific atom i. Then,

$$E_i^{\mathrm{kin}} = h\nu - E_i^{\mathrm{bind}}, \tag{4.1}$$

where $h\nu$ is the energy of the X-ray source and E_i^{bind} is the electron binding energy of the core level. The recorded spectra showed count rate peaks at various core level binding energies and typical XPS background signals. The background signal was higher for lower kinetic energies, but it remained constant between individual core level peaks. This type of background has first been described by Shirley [136] and is attributed to inelastic photoelectron scattering in the solid. It can be derived using a scattering cross section function which depends on the magnitude of the energy loss of the scattered electron [137, 138]. Figure 4.5 shows a scan of the photoelectron spectrum of a type C sample coated with 30 dipping cycles. The most prominent peaks are assigned to core levels of oxygen, titanium, and carbon, and to an oxygen Auger conversion which also leads to electron emission.

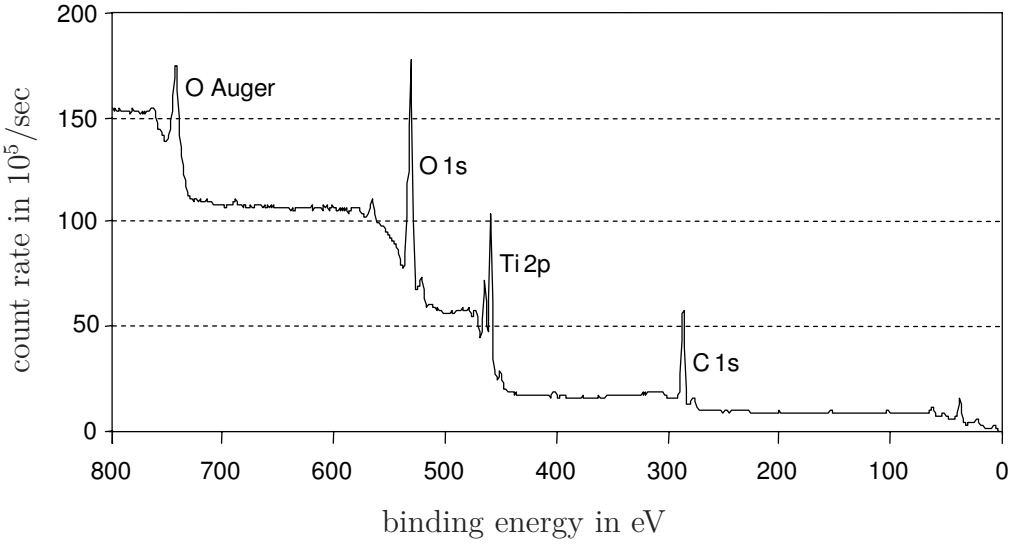

Figure 4.5: Photoelectron spectrum versus calculated binding energies with characteristic core level peaks and background signal.

Survey scans covering the entire accessible spectrum were used to identify the position of all individual XPS signals. After a complete assignment of all signals to elements present on the sample surface, individual peaks were scanned with higher resolution to determine the exact position and strength of the signal. Background subtraction from these higher resolution scans was performed manually, assuming a linear increase of the background signal across each peak.

Figure 4.6 displays detailed scans of two separate energy regions obtained from two type B samples, one after the first PSS coating step (black line) and and one after the subsequent first TiO_2 step (red line). The Ti 2p, In 3d, and S 2p peaks are doublets split by spin-orbit coupling (not resolved for S 2p) and represent signals from TiO_2, ITO substrate, and PSS, respectively. One observes from the graphs that after the first TiO_2 coating step a Ti 2p signal appears. Meanwhile, both the In 3d and the S 2p signal are reduced since ITO and PSS are now both partially covered with TiO_2 nanoparticles. For the quantitative analysis described in the following, the count rates of a peak doublet chosen to represent element i were integrated after background subtraction to give the total count rates f_i.

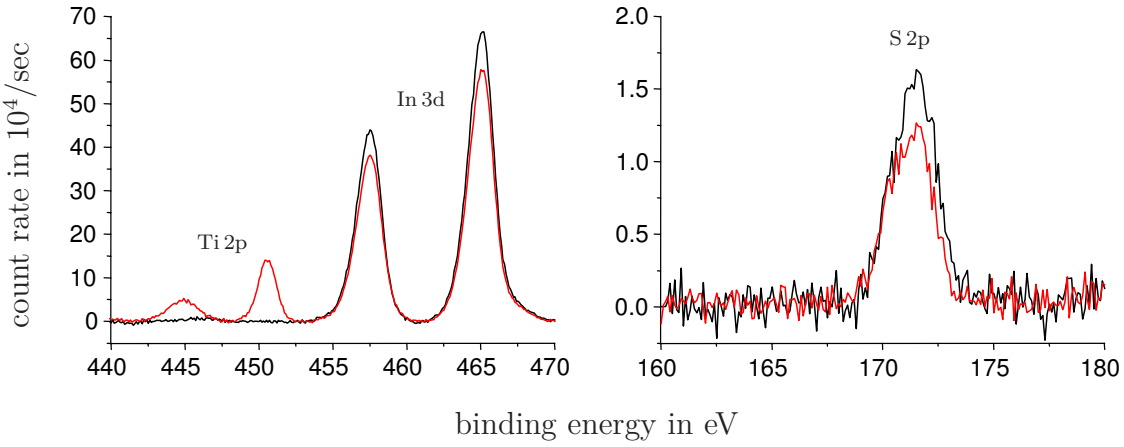

Figure 4.6: XPS core level signals before (black lines) and after (red lines) coating with TiO_2 nanoparticles (background signal removed).

The measured count rates f_i were used for the analysis of the composition of the photoemitting part of the samples. f_i is proportional to both the number of the specific atoms N_i^{atom} and the core level specific atomic sensitivity factor ASF_i:

$$f_i = k\, N_i^{\text{atom}}\, \text{ASF}_i \tag{4.2}$$

Here, k is a constant containing factors that are not element-specific, including the intensity of the X-ray source.

We assume a uniform maximum escape depth of photoelectrons d for all types of materials, such that for a certain domain of the sample only the material at the surface emits photoelectrons without energy losses. Then, the number of a specific type of signature atoms (e.g., sulfur) is proportional to both the area S_i that the corresponding material (e.g., PSS) covers and the volume density of signature atoms n_i^{atom} in that material.

$$N_i^{\mathrm{atom}} = S_i \, d \, n_i^{\mathrm{atom}} \tag{4.3}$$

Since each monomer of PSS contains one sulfur atom, the volume density of sulfur atoms equals the volume density of the monomer of PSS. The latter can be calculated from the mass density of pure PSS, which we took as $1.2\,\mathrm{g/cm^3}$, and the specific mass of the monomer of 183.2 u. Likewise, each titanium atom that contributes to the photoelectron signal corresponds to a group of one titanium and two oxygen atoms, which is the building block of TiO_2 crystals and has a mass of 79.9 u. The volume density of that group is defined by its mass and the mass density of TiO_2, taken as $4.26\,\mathrm{g/cm^3}$.

The ratio of indium to tin in the ITO samples we used was measured as 7.9:1 by comparing the XPS signals from the In 3d and the Sn 3d core levels from different samples. It follows that to each indium signature atom belong 0.127 tin atoms and 1.75 oxygen atoms. As before, the volume density of this fractional group can be calculated from its mass of 157.9 u and the mass density of ITO, which we took as $6.8\,\mathrm{g/cm^3}$.

We call these respective groups 'monomers' and use the equality of atom and monomer densities:

$$n_i^{\mathrm{atom}} = n_i^{\mathrm{mon}} \tag{4.4}$$

The monomer volume density n_i^{mon} can be calculated from its specific mass m_i^{mon} and the mass density of the respective material ρ_i, as explained above.

$$n_i^{\mathrm{mon}} = \frac{\rho_i}{m_i^{\mathrm{mon}}} \tag{4.5}$$

The quantities we are interested in are the relative sizes of the areas S_i covered with the material i, which can be calculated from equations (4.2) to (4.5):

$$S_i = \frac{f_i m_i^{\mathrm{mon}}}{k \, \mathrm{ASF}_i d \rho_i} \tag{4.6}$$

E.g., for the ratio of the areas covered with materials $i = \mathrm{PSS}$ and $j = TiO_2$ one obtains

$$\frac{S_i}{S_j} = \frac{f_i m_i^{\mathrm{mon}} \mathrm{ASF}_j \rho_j}{f_j m_j^{\mathrm{mon}} \mathrm{ASF}_i \rho_i}, \tag{4.7}$$

where f_i and f_j are the measured count rates and all other quantities are known constants.

Even though the absolute sizes of the individual areas cannot be determined, we can calculate the relative sizes of the uncovered surface area and the areas covered with either TiO_2 or PSS. We assume that the entire surface is composed of these three types of areas and normalize the data for each sample individually, so that their sum accounts for 100%. Figure 4.7 displays the relative contributions measured after each of the deposition steps described above. The data of the first two deposition steps was calculated from the XPS signals displayed in Fig. 4.6. After the very first PSS deposition step, 41% of the surface are covered with PSS, and 59% are left uncovered (no TiO_2 coverage is present). A TiO_2 coverage appears after the following step, when TiO_2 nanoparticles are deposited. The TiO_2 coverage jumps to 14%, while the contribution of both ITO and PSS are reduced, showing that these areas are being covered by nanoparticles. The reduction of PSS coverage, however, is much less than the reduction expected for a complete re-dissolution of the PSS polymer during the sample immersion in the TiO_2 bath. We can therefore reject the hypothesis that the polymer is re-dissolved and not incorporated into the films.

The third set of data in Fig. 4.7 displays the relative coverages after the second PSS deposition step. During this process, the uncovered area (ITO) is further reduced. So is the area covered with TiO_2, showing the deposition of PSS polymers on top of the nanoparticles. The PSS coverage increases roughly to the level before the TiO_2 deposition. During the fourth, fifth, and sixth deposition step, the relative coverages are changed in equivalent ways: Uncovered area is reduced continuously, and the PSS coverage fluctuates around 40%. The TiO_2 coverage is slightly reduced during PSS deposition, and increases sharply by 14-18% during deposition of TiO_2 nanoparticles.

The last two data sets correspond to one complete deposition cycle on top of a sample that had been precoated by 60 previous cycles. No indium signal was detected, indicating that the substrate is covered completely. Hence, a complete deposition cycle does not alter the surface composition at this stage. The data that is displayed was recorded after TiO_2 and after PSS deposition, respectively. It shows that the relative coverages are changed by the individual deposition steps. This finding confirms that additional amounts of both polymer and nanoparticles are deposited during the immersion of thick samples and that both materials are incorporated continuously during the whole coating process. The incorporation of TiO_2 nanoparticles was expected from the observed continuous linear increase of sample thickness. An incorporation of polymers, however, was not clear so far [115].

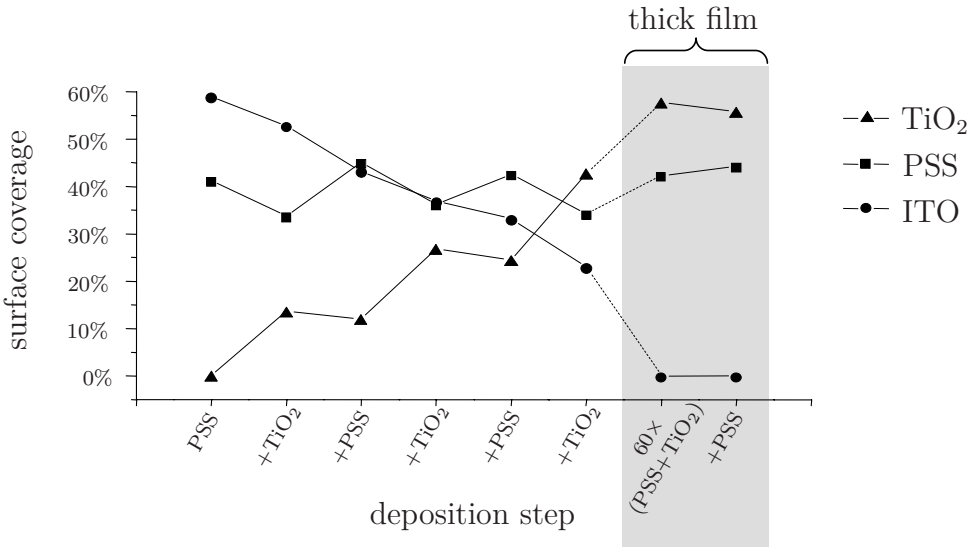

Figure 4.7: Fraction of sample surface covered with TiO_2 nanoparticles, PSS polymer, or uncovered (ITO), after a sequence of deposition steps.

4.2.3 Internal film structure

For the photovoltaic applications of thin composite TiO_2 / polymer films outlined in Chapter 2, the internal film morphology is crucial. The size of the specific internal surface restricts the amount of molecules that can be deposited for sensitization. The size and connectivity of the pores determine the accessibility of the internal surface from the outside by particle diffusion. These internal features cannot be reliably determined by surface sensitive techniques such as XPS or SEM.

We investigated the film penetration and adsorption of organic molecules directly. To that end, we immersed nanoporous films grown layer-by-layer into solutions of organic dye molecules. Sample batches of four samples coated with 30, 60, 90, and 120 dipping cycles were grown using the protocols A, B, and C, and left in the solutions until a significant coloration had occurred. All samples of one batch were immersed for the exact same time. We used the dyes fluorescein, Rhod6G and Ru535 listed in Table 3.2.

The metal complex dye **Ru535** is known to strongly bind to and sensitize TiO_2 surfaces [28, 56, 139]. Following the adsorption recipe provided by Solaronix, samples were heated to 70°C and the solution to 80°C before sample immersion. With the samples immersed, the solutions were kept at 70°C for another 2–3 hrs, and then allowed to cool down overnight. Then, samples were removed and dried in nitrogen. All sample types assumed a brown color. Desorption of the dye occurred in less than 15 min when samples were immersed in sodium hydroxide solution.

For **Rhod6G**, no elevated temperatures were applied during the adsorption process. After 55 min of immersion, dye adsorption had saturated and samples were removed and dried in nitrogen. The results were different for different sample types. While no significant coloration was observed for type A and C samples, type B samples, which were grown with polyanionic PSS, were intensely colored in dark pink. Desorption in ethanol took several days, and required the samples to be placed in fresh solvent several times. All desorbed dye was quantified for each sample using a method described below.

After 55 min of adsorption time in a solution of anionic **fluorescein**, we observed only a very light orange color for type A and C samples, and no coloration for type B samples. In any case, no sufficient desorption of dye could be detected even after several days of immersion in clean sodium carbonate solution.

The only batches where significant concentrations of dye could be detected in the desorption solutions were the sample types A, B, and C coated with Ru535, and type B coated with Rhod6G. The latter was colored more intensely than the Ru535 samples. The amount of dye in the solutions was determined by absorption spectroscopy. Figure 4.8 shows the absorption spectra of Ru535 and Rhod6G with the maxima at 309 nm and at 530 nm which we used for the quantitative analysis.

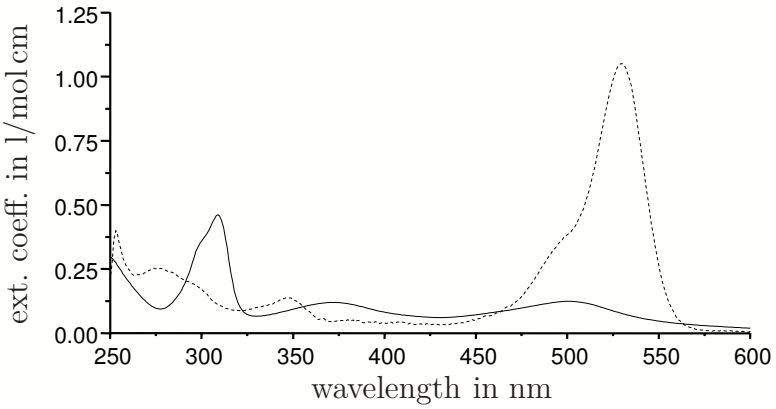

Figure 4.8: Extinction coefficients of Ru535 in sodium hydroxide solution (solid line) and Rhod6G in isopropanol (dashed line).

Figure 4.9 shows an image of a complete batch of type B samples of different thicknesses dyed with Rhod6G, as well as an image and the absorbance spectra of the desorption baths after dye desorption. Note that the bottom ends of the samples are bare, since irregular coatings at the bottom edges were removed manually. One observes that the thicker samples on the right are more intensely colored and also that the corresponding desorption baths apparently contain more dye.

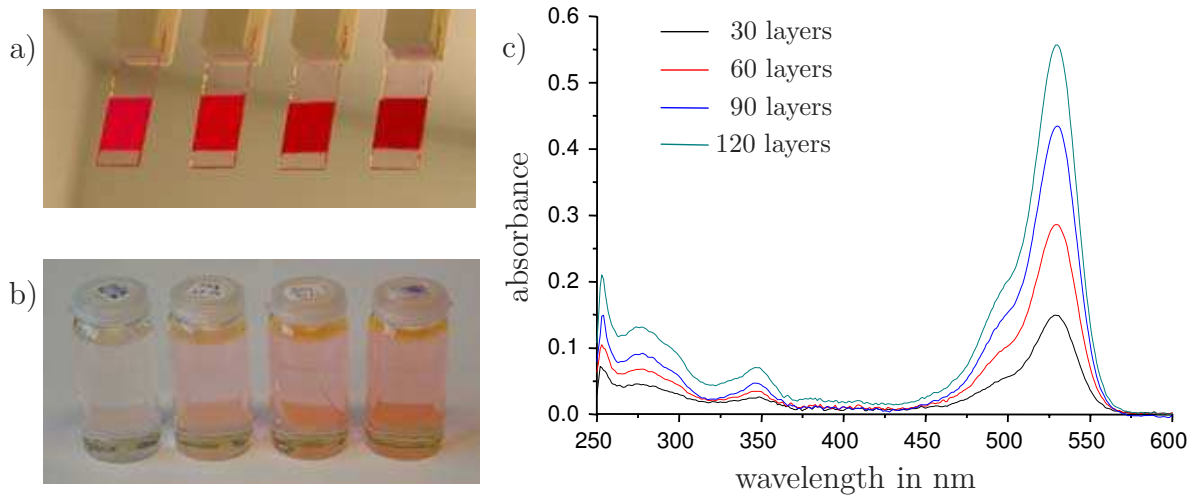

Figure 4.9: a) From left to right: type B samples coated with 30, 60, 90, and 120 layers after Rhod6G adsorption, b) desorption baths of each sample, c) bath absorbance in UV-Vis range.

The concentration c of the desorption solution was calculated from the measured absorbance A_λ at wavelength λ and the optical path length of the cell d using Beer's law:

$$A_\lambda = c\,\varepsilon_\lambda d \tag{4.8}$$

We used the following values of the molar extinction coefficients ε_λ: For Ru535 dissolved in sodium carbonate solution we measured $\varepsilon_\lambda = 4.6\,10^4\,\mathrm{l\,mol^{-1}cm^{-1}}$ at $\lambda = 309\,\mathrm{nm}$, and for Rhod6G dissolved in isopropanol we used $\varepsilon_\lambda = 1.05\,10^5\,\mathrm{l\,mol^{-1}cm^{-1}}$ at $\lambda = 530\,\mathrm{nm}$ [140].

From the concentration and the total volume of desorption solution one obtains n, the amount of desorbed dye molecules.

$$n = c\,V \tag{4.9}$$

Figure 4.10 displays the measured amount of dye molecules n per covered sample area S_{sample} against the sample thickness, which was determined by AFM, according to the method described in Section 4.2.1. The apparently linear relationship provides quantitative evidence that the internal surface increases linearly with the sample thickness, and that all of that area is accessible for dye molecules in solution. Each of the graphs is based on a series of desorption and spectroscopy experiments as displayed in Fig. 4.9.

Assuming that the molecules form a monolayer on the surface and that each molecule occupies an area of S_{dye} when adsorbed, one can calculate the ratio of the internal surface area covered with dye and the area of the projection plane S_{sample}. The ratio of

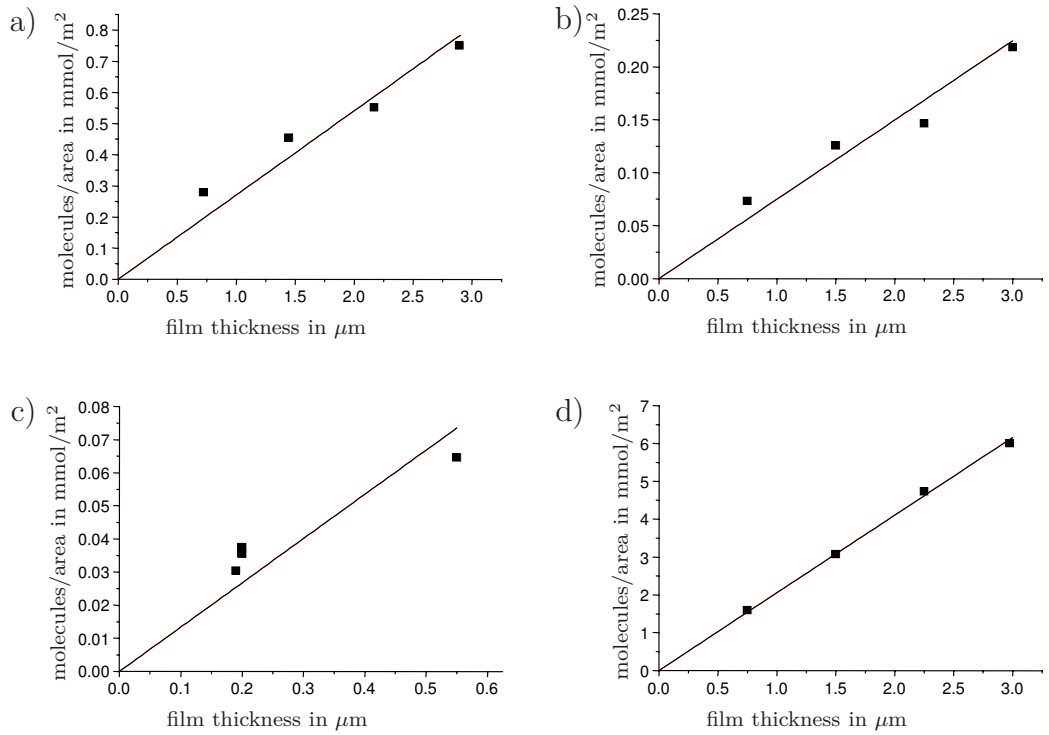

Figure 4.10: Amount of deposited dye (quantified by absorption spectroscopy) versus film thickness (measured by AFM): a) type C/Ru535, b) type B/Ru535, c) type A/Ru535, d) type B/Rhod6G.

the two areas is called the roughness factor (RF):

$$\mathrm{RF} = \frac{n S_{\mathrm{dye}}}{S_{\mathrm{sample}}} \tag{4.10}$$

Using the equations (4.8), (4.9), and (4.10), the RF can be calculated from known quantities:

$$\mathrm{RF} = \frac{A_\lambda V S_{\mathrm{dye}}}{\varepsilon_\lambda d\, S_{\mathrm{sample}}} \tag{4.11}$$

The following table gives the amounts of deposited molecules per film thickness calculated from the linear fit of the data in Fig. 4.10, as well as the corresponding RF for films with a thickness of 1 μm calculated using equation (4.11):

	sample	molecules/area in mmol/m$^2\mu$m	RF for 1 μm
a)	type C/Ru535	0.205	123
b)	type B/Ru535	0.075	45
c)	type A/Ru535	0.134	81
d)	type B/Rhod6G	2.053	1236

The RFs obtained for Ru535 coated samples are on the same order of magnitude as the value given in the literature (RF = 77) for 1 μm thick sintered thin films of TiO_2 nanoparticles (P25, Degussa) [141]. We therefore believe that indeed a coverage of roughly one monolayer of Ru535 forms and that the obtained values reflect the actual value of the surface area. Since the specific coverage of Rhod6G molecules is one order of magnitude larger, we believe that the coverage in this case is significantly higher than a monolayer and that the calculated value of the RF overestimates the real film property.

The film penetration of ionic dyes is apparently influenced by electrostatic interactions with the polyions incorporated into the layers. When negatively charged fluorescein dye was used, no dye adsorption was observed for sample type B containing the polyanion PSS, while type C samples containing the polycation PDAC were colored orange. The adsorption of positively charged Rhod6G was also selective: Films containing PSS showed strong adsorption of the dye, while films containing polycationic PDAC did not. The following table summarizes the degrees of coloration observed for the different sample types:

sample type	Ru535 (neutral)	Rhod6G (+)	fluorescein (–)
B (PSS, –)	moderate	strong	none
C (PDAC, +)	moderate	none	weak

Type A films that were grown using a buffer solution with pH = 2 in general behaved like type C samples, however, the difference compared to type B are less pronounced.

The results in this section demonstrate that small dye molecules in solution can penetrate the porous films and adsorb on the internal surface. The linear dependence of the deposited amount of molecules on sample thickness underlines that penetration is not limited to any depth of the films investigated. The films are therefore believed to have an interconnected system of pores large enough for molecule diffusion. The molecule coverage is apparently independent of film depth and uniform for all samples of the same type, indicating a uniform internal structure of the films.

4.3 Summary and conclusions

We conducted a characterization of thin films of TiO_2 nanoparticles and polyions grown with a layer-by-layer self-assembly process. We analyzed the growth mechanism, film composition, surface structure, and internal structure with a focus on utilization in

photovoltaic cells. We observed a linear growth for sample types B and C, which we grew using polyions, with a deposition rate close to a monolayer of TiO_2 particles during each dipping cycle. The growth of type A samples, in contrast, which did not involve any polyion solutions, was less regular, and the average deposited amount per dipping cycle was less than a monolayer. Apparently, the deposition of TiO_2 nanoparticles dominated the total increase of thickness and thus also mass during each dipping cycle. Apparently, polyions played a crucial role in the layer-by-layer process by inducing charge reversal on the surface.

We determined the surface composition of samples grown with polyion solutions and found a continuous incorporation of the polymers into the films. This finding led us to conclude that the films contain polymers in significant amounts. Hence, with respect to functionalized films, the incorporation of charged polymers with special optical or electronic properties into the thin films seems to be a feasible approach.

SEM images revealed that the surface structure varied between the sample types. Especially type C samples showed a distinct structure, with the surface completely covered by aggregates with sizes of a few micrometers. These features have the potential to increase the path length of light in the films significantly by light scattering. An increased efficiency of photovoltaic cells based on these films has been observed previously [43].

The internal structure was investigated by dye diffusion into the pores and adsorption on the internal surface. The experiments proved that the films feature a connected network of pores large enough for deep penetration of molecules. Electrostatic interactions between dye molecules in solution and polyions in the films had a significant influence on adsorption. These film properties are important for the sensitization of the TiO_2 nanoparticles with organic dyes for an application in DSSCs.

The results of structural characterizations presented in this chapter open up various strategies for the fabrication of hybrid organic / inorganic photovoltaic cells using the method of layer-by-layer self-assembly. Apart from sensitization with organic dyes after the film growth, the incorporation of light-absorbing species such as conjugated polymers or semiconductor QDs into the films during the growth process appears promising. This approach was pursued in the experiments presented in the following chapters.

Chapter 5

TiO_2 / polythiophene thin film devices

5.1 Outline

In this chapter, we report on the fabrication and characterization of hybrid bulk heterojunction photovoltaic cells, consisting of TiO_2 nanoparticles as an n-conductive phase and the polythiophene derivative PTEBS, described in Section 3.1, as a p-conductive and additionally light-absorbing phase. Based on the results of the preceding chapter, we introduce PTEBS as a negatively charged polymer to the layer-by-layer self-assembly method and grow composite films by combining PTEBS with positively charged TiO_2 particles. We chose the layer-by-layer method for the fabrication of the films to achieve an intimate contact with a large interface area between the two phases.

In order to obtain functional photovoltaic devices, we grow the films on conductive substrates and carry out further processing. We coat them with additional PTEBS material to fabricate a homogeneous sample surface. Since the self-assembled composite films are expected to be porous, according to the results in the preceding chapter, the intention of the coating is also a filling of the pores to increase light absorption in the films. On the polymer surface, we evaporate gold layers as ohmic back contacts.

We focus on well defined cell structures and reliable device performance, so that relationships between structure and performance can be investigated. Section 5.3 contains the results of structural and electronic characterization experiments which we conducted with these devices.

5.2 Device fabrication and electronic structure

5.2.1 Electronic material properties

As mentioned above, we use PTEBS as an absorber and hole transport phase [38, 83]. The chemical structure of the compound, shown in Table 3.1, exhibits two features that are relevant for the application intended here: Each monomer carries a negatively charged sulfonate group which solubilizes the molecule in water and receives the electrostatic forces acting during the self-assembly process [83]. Further, the conjugated polythiophene type backbone of the polymer features delocalized electrons, inducing semiconducting behaviour and a broad absorption band in the visible range. The sulfonate group is reported to induce self-doping of the polymer, creating charges on the polymer backbone and contributing to its p-type behaviour [142]. Figure 5.1 displays the absorption of PTEBS compared to PSS, which does not feature delocalized electrons along the backbone and hence no absorption in the visible.

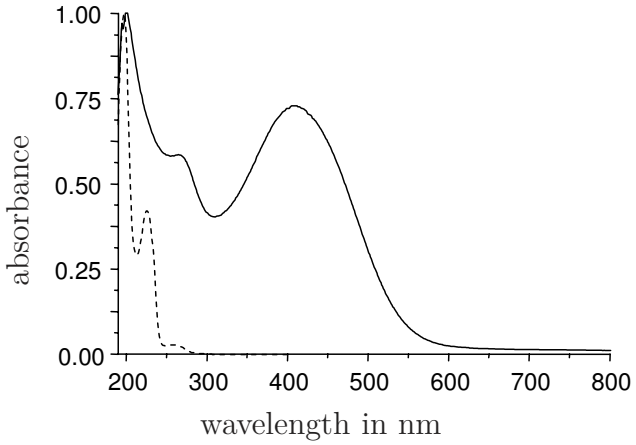

Figure 5.1: Normalized absorption of PTEBS (solid line) and PSS (dashed line).

The energy gap of PTEBS is $E_{\mathrm{gap}} = 2.2\,\mathrm{eV}$, and the energy positions of the LUMO and the HOMO are estimated as 2.8–3.1 eV and 5.0–5.3 eV below the vacuum level, respectively [83]. The transparent and quasi-metallic FTO with a work function of $W_{\mathrm{FTO}} = 4.4\,\mathrm{eV}$ will be used as the front electrode, and Au with a work function of $W_{\mathrm{Au}} = 5.2\,\mathrm{eV}$ as the back electrode [59]. The energy level structure of these materials shown in Fig. 5.2 meets the requirements for photovoltaic operation, as outlined in Section 2.3.3. We processed PTEBS from aqueous solutions with a concentration of 1.0 wt. % and an ammonium hydroxide content of 3 wt. %. Details on the processing are given in the following section.

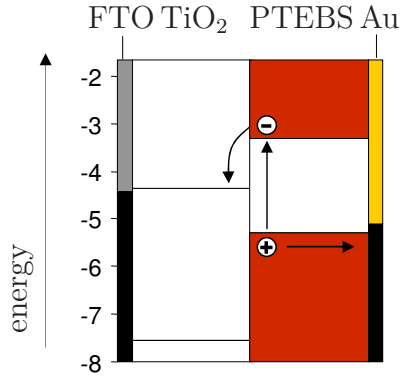

Figure 5.2: Heterojunction structure of a TiO_2 / PTEBS cell.

5.2.2 Cell fabrication

Substrate preparation and thin film self-assembly

We used FTO coated glass slides from Nippon Sheet Glass as substrates. The cleaning procedures which we employed are described in Section 3.1. The cleaned and hydrophilized samples were either used for the self-assembly process without further processing, or they were coated with a thin film of compact anatase TiO_2 before, as described in Section 3.2.1. The function of this layer is to prevent contact between the hole transport phase PTEBS and the FTO anode [143].

The samples, both with a compact TiO_2 layer and without, were coated with the layer-by-layer self-assembly process, using TiO_2 nanoparticles in an acidic solution and PTEBS in aqueous solution. The coating protocol described in Section 3.2.2 was repeated either 30, 60, 90, or 120 times. We also used type C samples grown with PDAC which we annealed at 400°C for 60 min in order to improve contact between the TiO_2 particles.

Macroscopically homogeneous films were obtained. Figure 5.3 shows samples grown using PSS and PTEBS as polyions. The bright red color of the PTEBS sample demonstrates that polymers were incorporated in significant amounts and that the light-absorbing properties were retained.

Polymer top layer fabrication

The structure of the PTEBS phase is crucial for hybrid device performance in several aspects. First, it should penetrate the porous TiO_2 film as a continuous phase for efficient hole transport. This penetration has been observed for other types of poly-

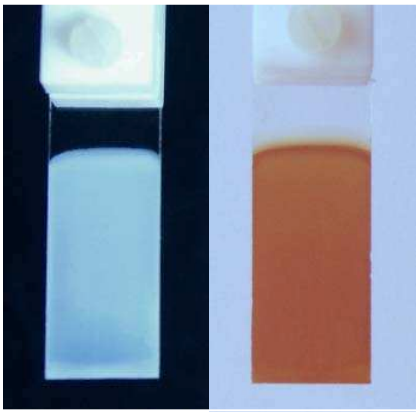

Figure 5.3: Samples grown with PSS (left) and PTEBS (right).

thiophene derivatives upon brief sintering [39, 87], but was not found by Qiao and McLeskey for PTEBS [38]. Second, the top layer should be thick enough to cover the TiO_2 completely, in order to fabricate homogeneous contacts at the back electrode and prevent the formation of recombination channels. Third, it should not be exceedingly thick to avoid a high internal resistance limiting the photocurrents. A thin coating with a uniform thickness is hence desirable.

When we employed conventional methods such as spin-coating, drop-casting, or the doctor blading method [38] with aqueous PTEBS solutions, the requirements outlined above were not met on a macroscopic scale. The samples showed areas colored both dark and light, indicating inhomogeneous PTEBS film thicknesses.

Spin-coating (spinning speeds 800–1200 rpm), apart from wasting most of the applied material, proved unsuitable for fabricating the top layer. PTEBS solution inevitably accumulated at the edges during spinning, creating a gradient of coverage from the slide center to the edges. This effect was aggravated when we used elongate slides. Increasing the spinning speeds resulted in not enough material being deposited.

Drop-casting the top layer showed the opposite effect of too much material being deposited in the sample center. After dropping and an initial manual distribution, the solution wetted the TiO_2 film completely. During the evaporation process, however, it showed a tendency to dewet and contract toward the center. Figure 5.4 a) displays a sample where almost all polymer material was deposited in one central spot approximately 1 cm wide.

As a variation of the doctor blading technique, it was attempted to continuously redistribute the solution during the drying and contracting process using plastic pipette tips. Little improvement with respect to film homogeneity was achieved, because, as

the viscosity of the solution increased, the tip application itself created spots. Such a deficient film quality renders reproducible characterization of electronic devices impossible. Devices fabricated in areas of thin coverage had either shorts or very low photovoltages, and devices in areas with thick coverage had higher photovoltages but very low currents. Figure 5.4 b) shows one of the best attempts at making films by dropping and manually re-distributing the PTEBS solution.

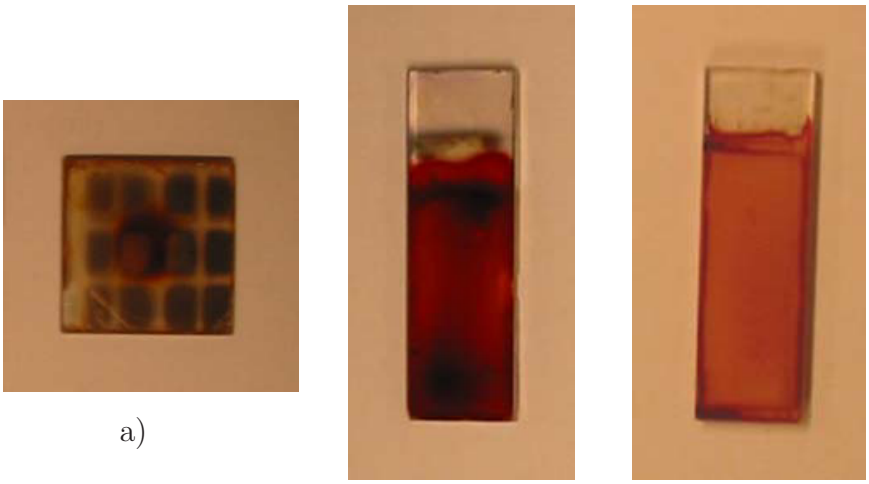

a) b) c)

Figure 5.4: Drop-cast PTEBS films: a) material concentrated in one central spot (on a sample with an array of Au electrodes), b) inhomogeneous film fabricated by manual re-distribution, c) homogeneous film fabricated using a wire frame.

We developed a variation of the drop-casting technique that utilizes the surface tension of the PTEBS solution for the formation of a homogeneous film. A mask holding a set of four crossed copper wires was built, which could be placed on top of a sample so that the wires formed a frame around the area which had to be coated. The left image in Fig. 5.5 shows the mask fitted with the four wires.

After dropping the solution, we spread it out between the wires so that the liquid was in touch with them on all sides. The right image in Fig. 5.5 shows a sample on a heating plate with the PTEBS solution spread between the wires. The solution strongly wetted the wires at the edges of the sample surface, and it did not withdraw during the drying process. Figure 5.6 shows a schematic of the setup. We will refer to this method as 'frame assisted drop-casting'.

The forces resulting from the wetting of the wires ensured that the solution remained spread out until all solvent had evaporated. The surface tension induced a very uniform thickness of the solution film during this process. The thickness of the remaining solid

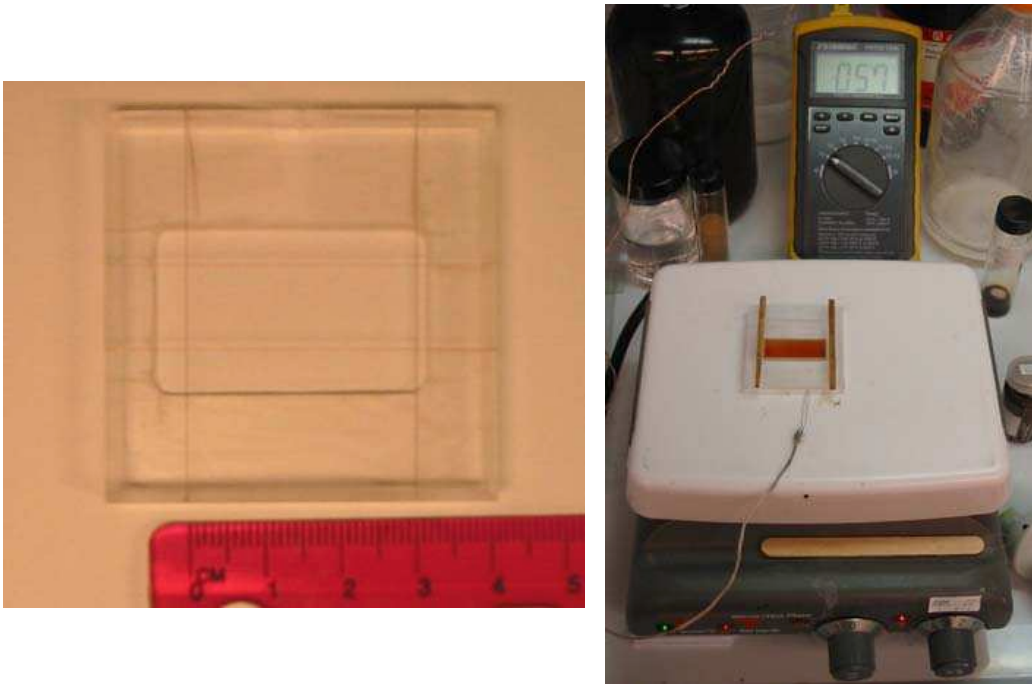

Figure 5.5: Left: frame formed by four crossed metal wires used for drop-casting, right: PTEBS coating procedure using the wire frame on a heating plate.

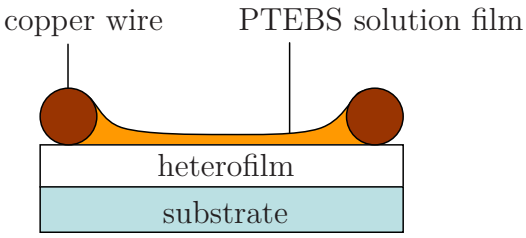

Figure 5.6: Cross sectional schematic of the wire frame setup used for drop-casting.

PTEBS film was also very uniform on a macroscopic scale, based on observations of color and light transmission of the films. Around the wires, small menisci of the solution formed locally between the wires and the sample surface, so that more material was deposited. This effect is displayed in Fig. 5.6. The width of the meniscus was less than 1 mm, so that the formation of large homogeneously coated areas between the wires was not obstructed and the amount of additionally depositited material is small compared to the total amount. A sample coated with our frame assisted method is displayed in Fig. 5.4 c), showing the superior film quality compared to other coating methods.

The wire frame can be filled with different volumes of solution. This feature allowed us to adjust the thickness of the top layer, simply by varying the solution amount. The frame assisted method was used with elevated temperatures in order to accelerate evaporation and increase polymer mobility and pore penetration.

Cell layout and contacting

For all layer-by-layer coated samples we used FTO slides with dimensions $40 \times 12\,\mathrm{mm}^2$. After all required coating steps, we made devices by fabricating 120 nm thick gold back electrodes with dimensions $3 \times 6\,\mathrm{mm}^2$ on top of the PTEBS films. Au was deposited in vacuum with a sputter coater or by metal vapor deposition. Figure 5.7 displays a finished sample with five Au back electrodes defining five devices.

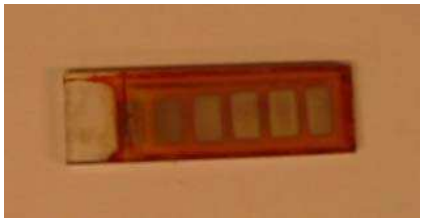

Figure 5.7: TiO_2 / PTEBS sample with five $3 \times 6\,\mathrm{mm}^2$ Au electrodes.

In order to contact the FTO front electrode, the substrate was locally exposed by removing the top layers. Next to the back electrodes, the film was scratched off on a 3 mm wide strip at the long edge of the slides. The coating of this strip with compact TiO_2 had been avoided by attaching an adhesive foil, as described in Section 3.2.1, since the compact layer cannot be mechanically removed.

5.3 Results and discussion

5.3.1 Film structure

Self-assembled porous layer

We investigated the surface structure of layer-by-layer self-assembled TiO_2 / PTEBS films with SEM. The resolution we obtained was lower than for the images shown in Fig. 4.2, owing to a higher level of mechanical vibration. Figure 5.8 shows images of a sample coated with 60 dipping cycles at different magnifications. The structure of the TiO_2 / PTEBS films resembles the structure of type B films, when the surface roughness and the density of nanoparticle aggregates are compared. These two samples were both grown with TiO_2 nanoparticles in an acidic bath and with negatively charged polyions, namely PSS and PTEBS. Hence, we believe that the structure of TiO_2 / PTEBS films is similar to type B samples investigated in the preceding chapter.

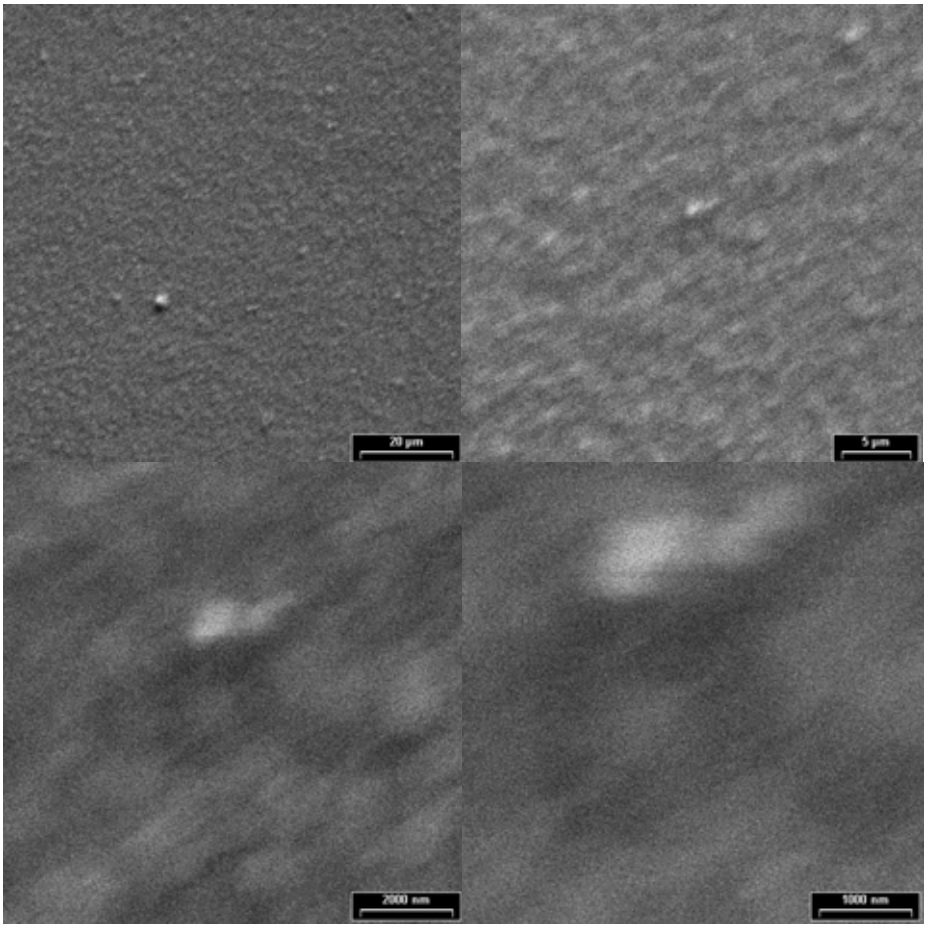

Figure 5.8: SEM images of a layer-by-layer grown TiO_2 / PTEBS film at different magnifications. Width of the scanned area: 100 μm (top left), 33 μm (top right), 10 μm (bottom left), 5 μm (bottom right).

The thickness of the films was measured by scratching off a thin line from samples coated with 30, 60, 90, and 120 dipping cycles and measuring the resulting step height with a profilometer. We observed linear growth and obtained a growth rate of 20.2 nm/dipping cycle, which is similar to the type B growth rate reported in Section 4.2.1.

The films' light scattering properties and the surface structure observed with SEM indicate that the films contain TiO_2 nanoparticles in significant amounts. The PTEBS content shows in the intense red color, as mentioned before. The film porosity was analyzed by investigating the penetration of PTEBS polymer, as described in the following.

PTEBS top layer

A direct method to determine the penetration of PTEBS into the porous films is to measure the overall thickness of composite films after a PTEBS top layer has been fabricated on top of a porous layer. The higher the penetration, the lower will be the total thickness.

We coated four samples with 2.4 μm thick porous TiO_2 / PTEBS films covering an area of 3.0 cm^2. Then, we fabricated PTEBS top layers with the frame assisted drop-casting method described above, using different amounts of solution. We scratched off thin lines of the films and measured the resulting step height with a profilometer at three different locations. Figure 5.9 displays the mean and standard deviation of these measurements, showing a linear increase in thickness, as well as a constant offset of 2.2 μm. The linear increase shows that the thickness increase per volume of solution was 0.0105 μm/μl.

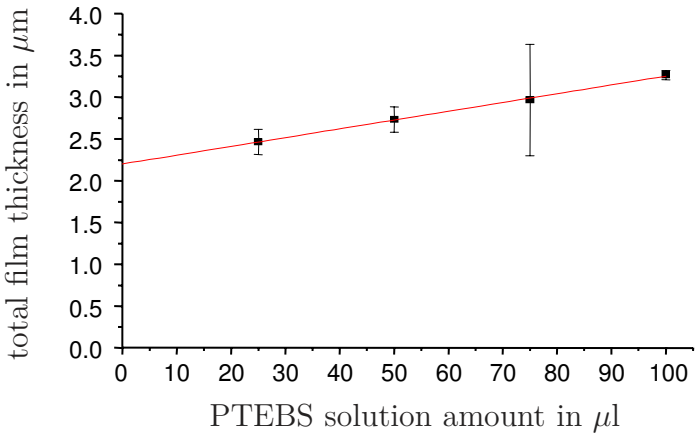

Figure 5.9: Linear fit of drop-cast PTEBS top layer thicknesses. Error bars are empirical standard deviations. Linear fit equation: $y = 2.200 \pm 0.024 + (0.0105 \pm 0.0003)x$.

This result is not in line with the assumption that the pores are filled with PTEBS completely. In that case, the total film thickness should not increase until the absorption capacity of the pores is depleted. Assuming a porosity of 30%, a total solution amount of 69 μl is necessary to fill the pores of the 2.4 μm porous film covering 3.0 cm^2. Therefore, if the pores were being filled by polymers, no increase of the total film thickness would be expected for solution amounts below 69 μl. For larger amounts, a dense layer on top of the filled porous layer would form and a linear increase of the total thickness would be observed. In our case, in contrast, a thickness increase is observed already for much smaller amounts of solution, indicating that the pores are not filled completely. The offset of the linear growth obtained from the linear fit displayed in Fig. 5.9 is 2.2 μm,

200 nm less than the initial thickness of the uncoated film. For a porosity of 30%, this difference, which is, however, inside the margin of error, indicates that PTEBS has penetrated the porous film up to a penetration depth of 600 nm. We conclude that the pore sizes of the porous films are too small for the formation of a continuous PTEBS phase reaching deep into the films.

5.3.2 Photoelectronic characteristics

Photovoltaic effect

We fabricated our devices by sequential deposition of a compact TiO_2 layer, a composite polyion / TiO_2 layer and a PTEBS layer in order to have a defined sequence of contacts. Our methods to fabricate the active layer, layer-by-layer growth of composite polyion / TiO_2 films and frame assisted drop-casting of PTEBS layers, allowed to control the film thicknesses and gave cells with reproducible characteristics. We placed at least four devices on each sample and compared their I/V curves. The exact procedure to measure these curves will be described in the part on time resolved measurements at the end of this section. All fabricated devices showed a diode characteristic in the dark and a pronounced photovoltaic effect. The shapes and positions of the I/V curves were very similar and reproducible for the devices placed on one sample, so that a systematic analysis of relations between sample structure and fabrication and device performance was feasible.

We used PTEBS / TiO_2 films and annealed PDAC / TiO_2 (sample type C) films for the fabrication of the active layer by coating them with PTEBS top layers. Two examples of the obtained I/V characteristics and their reproducibility are given in Fig. 5.10. The graphs show the I/V curves of four individual devices on the same sample. All cells are operational, and the characteristic parameters U_{oc}, I_{sc}, and FF are similar, even though not identical. Graph a) displays I/V curves from devices based on a PTEBS / TiO_2 heterofilm, graph b) displays curves from devices based on a PDAC / TiO_2 heterofilm. Both samples show reproducible device characteristics.

Influence of layer thickness and processing temperature on cell performance

We systematically investigated the dependence of the cell performance on the thickness of the individual layers. The reproducibility of the cell characteristics and thicknesses required for this investigation was achieved by the design and methods described above.

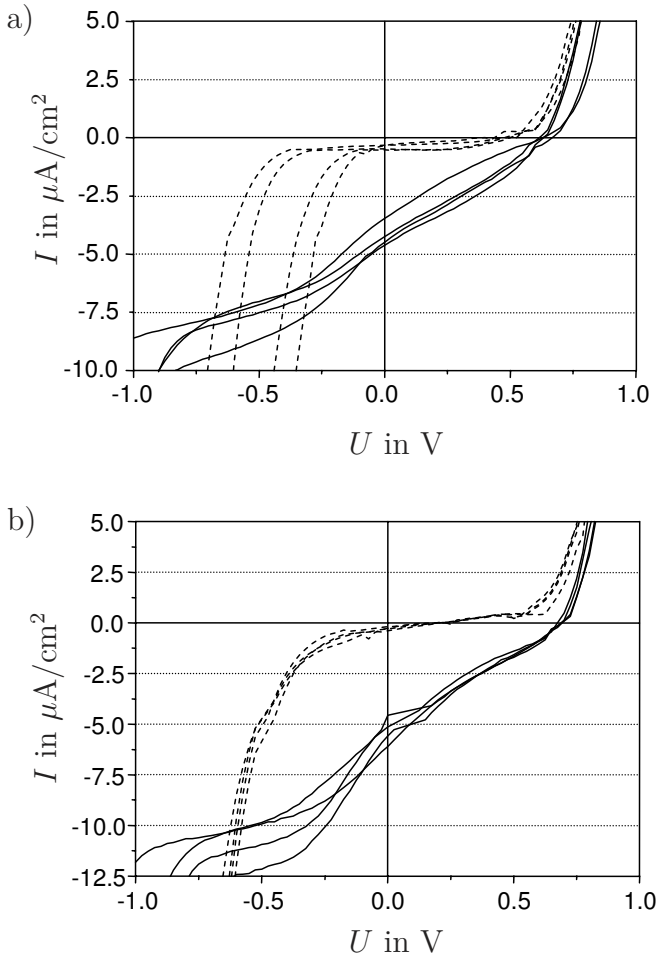

Figure 5.10: I/V curves in the dark (dashed) and in light (intensity 100mW/cm^2, solid) of four TiO_2/PTEBS devices. TiO_2 film grown with a) PTEBS, not annealed, b) PDAC, annealed.

We analyzed the influence of the top layer thickness on cell performance by using different amounts of PTEBS solution for drop-casting. We employed substrates coated with 2.9 μm thick porous TiO_2 films which had been grown with PDAC and annealed at 400°C, as described above. The graphs in Fig. 5.11 display the arithmetic means and standard deviations of the photocurrents I_{sc} and photovoltages U_{oc} of four devices on each sample. Each pair of I_{sc} and U_{oc} values displayed in Fig. 5.11 is based on a series of I/V curve measurements equivalent to the ones shown in Fig. 5.10. The thickness of the PTEBS layer was calculated from the amount of solution used and the amount-thickness relation obtained from the measurements displayed in Fig. 5.9.

The cell performance graphs displayed in Fig. 5.11 show broad maxima of both I_{sc} and U_{oc} for top layer thicknesses between 0.5 and 0.8 μm. For both thinner and thicker top layers, I_{sc} and U_{oc} are significantly lower than the maximum values. The lowered

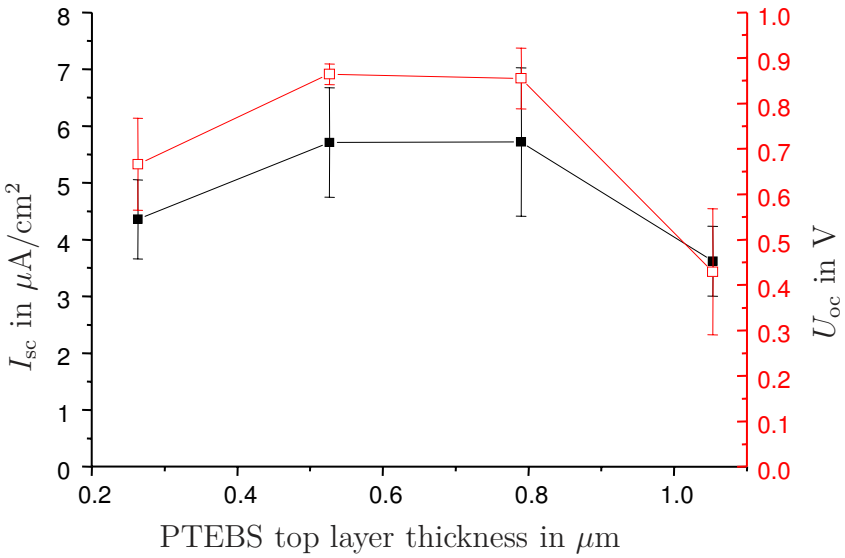

Figure 5.11: Photovoltages (red, open symbols) and photocurrents (black, solid symbols) of hybrid devices with different thicknesses of the PTEBS top layer.

photocurrents and photovoltages for thin top layers are probably caused by insufficient electron blocking properties, leading to recombination channels via the back electrode. The photocurrent decrease for films thicker than 0.8 μm can be attributed to increased resistance of the films. The photovoltage decrease, however, cannot be explained by increased resistance and could rather be induced by another mechanism limiting effective charge separation, such as trapping or recombination of carriers in the PTEBS phase.

For the experiments described in the following, we kept the thickness of the PTEBS top layer fixed at 520 nm, which produced the highest mean photovoltage in the experiments described above. Instead, we varied the thickness of the porous layer. Figure 5.12 displays the relations between the thickness and the photovoltaic properties for the different device types. We investigated devices based on both layer-by-layer grown PTEBS / TiO_2 films (triangles in Fig. 5.12) and annealed PDAC / TiO_2 (type C) films (squares). As in Fig. 5.11, each pair of I_{sc} and U_{oc} values displayed in Fig. 5.12 is based on a series of I/V curve measurements shown before.

Both types of devices showed a similar behaviour for different thicknesses of the TiO_2 layer. Photocurrents (black, solid symbols) decreased when the thicknesses were increased, while photovoltages (red, open symbols) increased. We attribute the former to an increased resistance of thicker porous TiO_2 films. The increased photovoltages can be explained by an improved quality of the contact structure of the device, meaning that in addition to the compact TiO_2 hole blocking layer, a thick porous TiO_2 film shields the

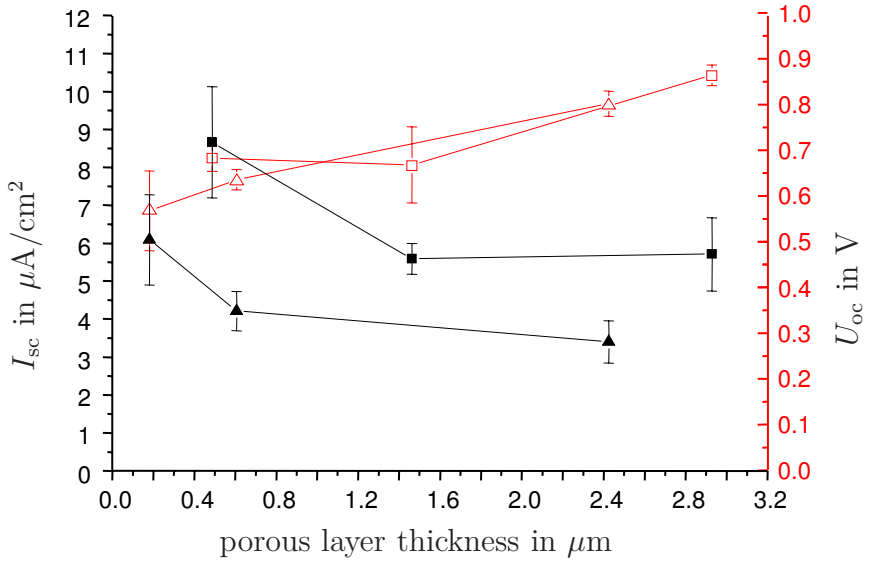

Figure 5.12: Photovoltages (red, open symbols) and photocurrents (black, solid symbols) of hybrid devices based on porous TiO_2 films grown with PTEBS (triangles) or grown with PDAC and annealed (squares).

anode from photogenerated holes in the polymer phase. The devices based on annealed type C films showed higher photocurrents than the ones based on TiO_2 / PTEBS films. Therefore, it stands to reason that the PTEBS incorporated during the layer-by-layer process did not contribute significantly to charge generation. This finding indicates that the PTEBS molecules incorporated during the layer-by-layer growth are not in contact with each other and isolated from the continuous PTEBS phase where it does not penetrate the pores. The transport of photogenerated holes from the ionized molecules to the back electrode is hence not possible, so that the holes do not contribute to the external current. The devices with annealed TiO_2 films (squares) probably benefited from better film cohesion and faster electron transport. We do not expect better PTEBS pore penetration and the creation of a larger interface to be the cause of the higher photocurrents, since annealing decreases the pore sizes of nanoparticulate TiO_2 films [43].

As mentioned before, the sample temperature during drop-casting might influence the degree of pore infiltration by increasing the polymer mobility, and thus also the cell performance [39]. However, we did not observe any difference in performance between cells fabricated at room temperature and at elevated temperatures of up to 70°C. Additionally, we attempted to increase pore infiltration by sintering devices after drop-casting the top layer. We sintered a TiO_2 / PTEBS device at 180°C for 30 min under argon and allowed the device to settle for 1 hr afterwards [87]. The cell survived the treatment and showed similar I/V curves, however, the photocurrent was reduced, as shown in

Fig. 5.13. Surprisingly, the device exhibited a region of negative differential resistance (NDR), a phenomenon known from tunnel diodes. These diodes have a heavily doped and very thin p-n junction which allows carrier tunneling for biases close to $V = 0$. For increased forward voltages, the tunneling stops and a NDR region is created [144]. This model cannot account for the NDR observed in our heterojunction devices, since the band alignment does not allow tunneling for low voltages.

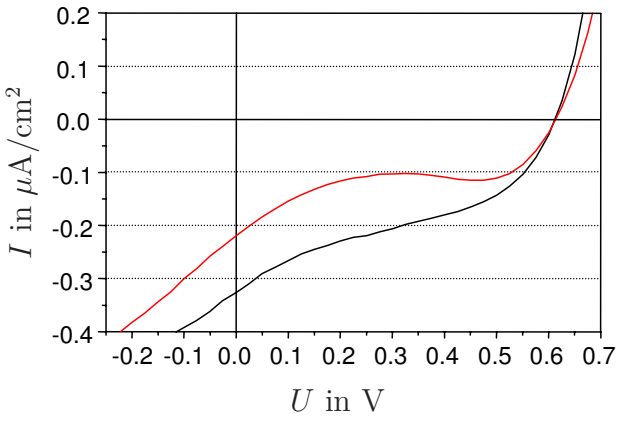

Figure 5.13: I/V curve of a TiO_2 / PTEBS device in white light before (black) and after (red) sintering at 180°C for 30 min.

I / V curve simulation and thin film resistance

We measured the current / voltage behaviour of a PTEBS / TiO_2 device with a 2.9 μm TiO_2 film annealed at 400°C. The device had a Au electrode evaporated in vacuum. The I/V curves of the device, which were obtained at a reduced white light intensity of 20 mW/cm^2, are shown in the top image in Fig. 5.14. The curves are smoother than the ones obtained with devices with sputtered electrodes. In light, a photovoltage $U_{oc} = 0.75$ V and a photocurrent of $I_{sc} = 1.27\,\mu$A/cm^2 were observed. The behaviour in forward bias is diode like as expected for a well defined heterojunction and described in the Sections 2.2.1 and 2.2.2, but in reverse bias it can apparently not be well described by the diode model. Notably, the device showed a region with NDR in the reverse bias region at -0.5 V.

The device behaviour in forward bias was simulated for data between 0 V and 0.85 V with the diode model described in Section 2.2.1. A closed solution to equation (2.30) was used as a fit function for a least squares fit with I_0, n, I_{ph}, R_s, and R_{sh} as fit parameters, which we constrained to positive values. The fit results are displayed in the bottom image of Fig. 5.14. The fit yielded a shunt resistance of R_{sh}=1.61 MΩcm^2,

which is in the range of *p*-*n* junction cells [48]. In the dark, we found an even higher shunt resistance of R_{sh}=14.3 MΩcm^2. For the serial resistance R_{s}, the fit procedure gave a value of zero in both cases. At $U = 1.0\,\mathrm{V}$ in light, we measured a curve slope corresponding to a serial resistance of $R_{\mathrm{s}} = 500\,\Omega\,\mathrm{cm}^2$, which we take as an upper limit for the actual R_{s}. Devices with a TiO_2 film that had not been annealed showed a slope corresponding to $R_{\mathrm{s}} = 1\,\mathrm{k}\Omega\,\mathrm{cm}^2$. The reason that these comparably high serial resistances are not clearly detected by the fit procedure is that they have little effect on the shape of the I/V curves. When the current level is low, high serial resistances have less effect than in the case of high currents, as one can see from a comparison of the curves we simulated for different current levels, displayed in Fig. 2.8.

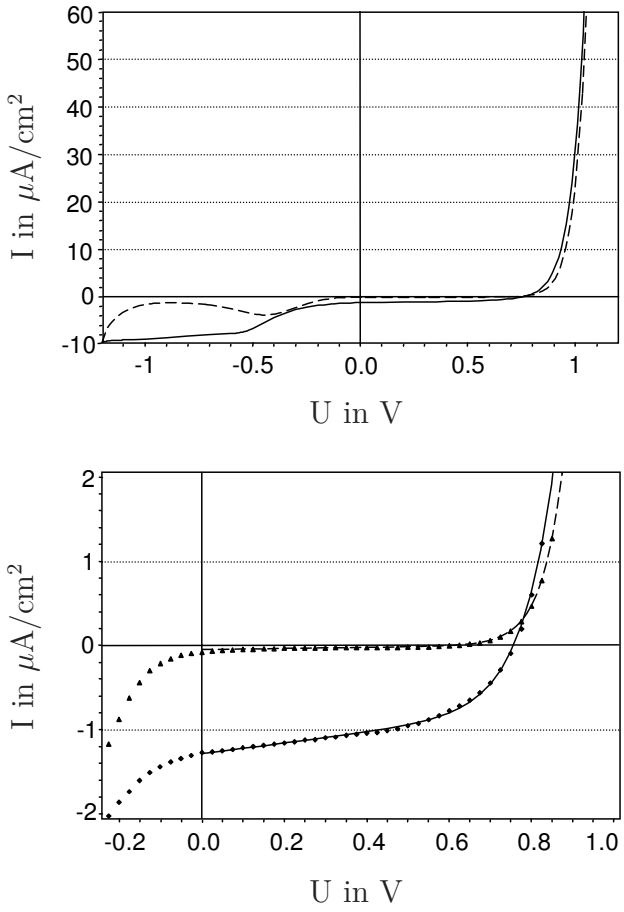

Figure 5.14: I/V curves of a TiO_2 / PTEBS device on different scales. Top: measured curves in light (20 mW/cm^2, solid line) and in the dark (dashed). Bottom: light/dark curves measured (diamonds/triangles) and simulated (solid/dashed line).

Influence of blocking layer

All devices described so far were fabricated with a compact TiO_2 layer underneath the porous film. However, the possibility of the hole conducting PTEBS *not* penetrating the porous film, which cannot be ruled out from the thickness and current measurements described above, raises the question whether the TiO_2 hole blocking layer is necessary at all.

Figure 5.15 shows the I/V curve measured in light ($20\,mW/cm^2$) of a TiO_2 / PTEBS device identical in structure to the one represented in Fig. 5.14, but fabricated *without* a compact TiO_2 layer. It shows neither a pronounced diode behaviour nor any photocurrent, the behaviour around $U = 0\,V$ is rather ohmic, and the curve is almost symmetric for negative and positive voltages up to $U = \pm 3\,V$. This finding leads us to conclude that in this device no effective heterojunction was formed.

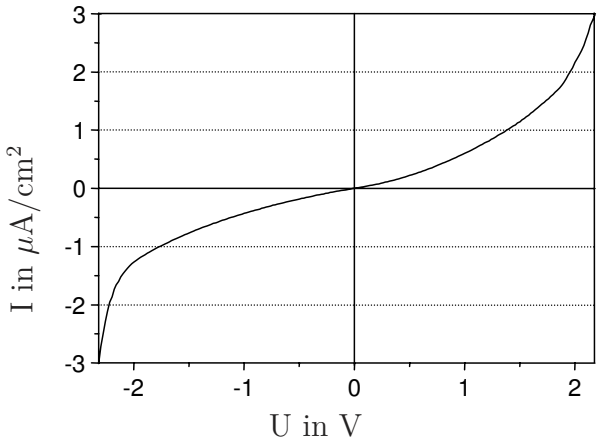

Figure 5.15: I/V curve of a TiO_2 / PTEBS device without a TiO_2 hole blocking layer.

Comparing the photovoltaic performance of devices with (Figs. 5.10 and 5.14) and without (Fig. 5.15) compact TiO_2 layers indicates that hole blocking layers are a vital component of our cell concept. Nevertheless, similar concepts yielded photovoltaic effects even though no hole blocking layer was used [38]. Regarding the question of whether the polymer phase actually penetrates the porous TiO_2 film, this result implies that some degree of deep penetration *does* occur.

Time-resolved measurements

When the voltage applied to TiO_2 / PTEBS devices was changed or the illumination switched on or off during measurements, a long-lasting rise or decay of the currents

through the devices followed and did not settle before up to 30 sec. In the following, we investigate this behaviour, explain the consequences for I/V curve measurements, and give possible explanations. Figure 5.16 shows the current through a TiO_2 / PTEBS device while a 100 mW/cm^2 illumination is switched on and off periodically and the voltage across the device is kept constant at 0 V. At time = 0 sec, the light is turned on and a negative current appears. However, it shows a continuous decay and does not saturate before 20 sec later. The saturation current is approximately a factor of three lower than the initial current. When the light is switched off at time = 40 sec, the current rises to the positive, drops below zero, and then slowly approaches $I = 0$. It does not, however, reach the expected saturation current of $I = 0$ even after another 40 sec, when the light is turned on again and the current behaviour repeats itself.

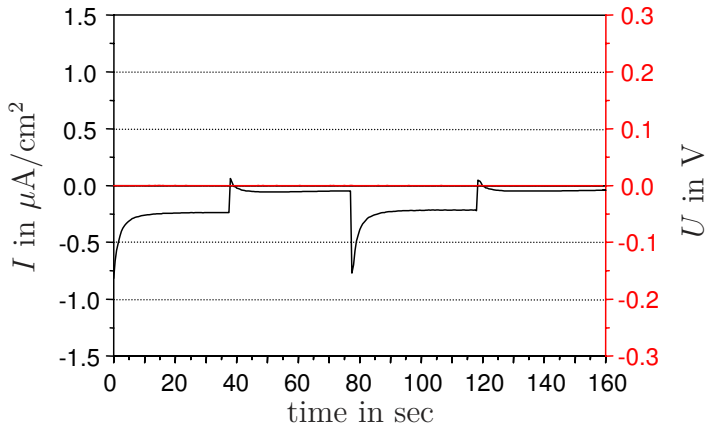

Figure 5.16: Photocurrent changes in time in a TiO_2 / PTEBS device upon switching the light on (at 0 sec, 80 sec) and off (at 40 sec, 120 sec).

In order to determine the decay characteristics we recorded the device behaviour on a longer timescale. We observed that the behaviour can be fitted well with a double-exponential decay, while a single-exponential decay does not fit. Figure 5.17 shows the measured current as well as the two fit functions. According to these results, the current in this case consisted of a constant photocurrent of 0.01 μA/cm^2, and two other components with characteristic decay times of 23.4 sec and 117.1 sec, respectively. We conclude that the constant part is the sustained current of photogenerated electrons. The two-component transient currents can be explained by two independent processes, (i) electrons escaping from traps and (ii) ionic currents, the latter of which might play a role because the PTEBS phase contains Na^+ counterions. The exact mechanism could not be determined, however, the possibility of ion rearrangements upon illumination would offer further applications for PTEBS/TiO_2 devices, as we explain below.

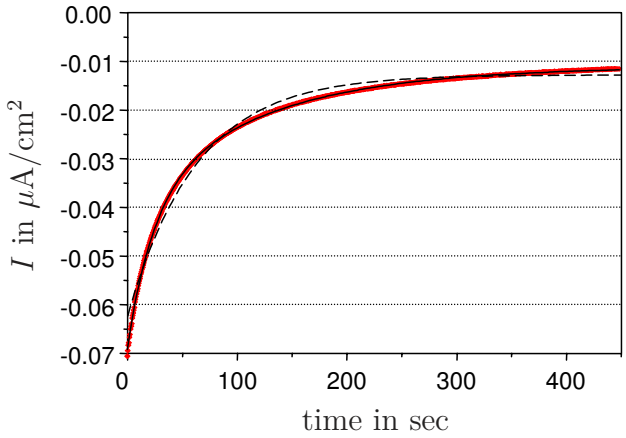

Figure 5.17: Double-exponential (solid black line) and single-exponential (dashed black line) fit of the current decay in a TiO_2 / PTEBS device after the light is turned on (red diamonds). Double-exponential fit: $y = 0.029\exp(-x/23.4)+0.028\exp(-x/117.1)+0.011$.

Current changes in time were also observed after voltage changes. During a typical I/V curve measurement of our devices, the behaviour of the current is similar to the cases depicted in Fig. 5.18. There, the voltage across a TiO_2 / PTEBS device under 100 mW/cm^2 illumination is ramped from negative to positive in the upper image and from positive to negative in the lower image, with switching steps of ± 0.05 V every 10 sec. Note that the sign of the time dependent current peaks depends on the ramping direction.

The current changes in time displayed in the Figs. 5.16 and 5.18 require to take care that the constant part of the current is isolated during I/V curve measurements. Otherwise the curves would depend on the delay time between changing the voltage and measuring the current. The transient behaviour shown in Fig. 5.18 requires measurement delay times of more than 10 sec, since the currents do not saturate fully within this time. The currents are apparently close to saturation, so that the I/V curve obtained with 10 sec delay time would be closer to the 'real' behaviour than a measurement made with the usual delay times in the range of milliseconds.

We took these observations into account for all I/V curve measurements we have described in this chapter. After switching on the light source, device currents were allowed to settle with the voltage kept constant. The I/V curves were recorded as time dependent curves like the ones shown in Fig. 5.18. From these curves, we could check whether current saturation had occurred. If it had occurred, the last current measurement before the following switching was used in the curve, otherwise we repeated the measurement with greater delays. Typical delay times were 10–30 sec for voltage steps of 0.025 V. This procedure made I/V curve measurements very time-consuming,

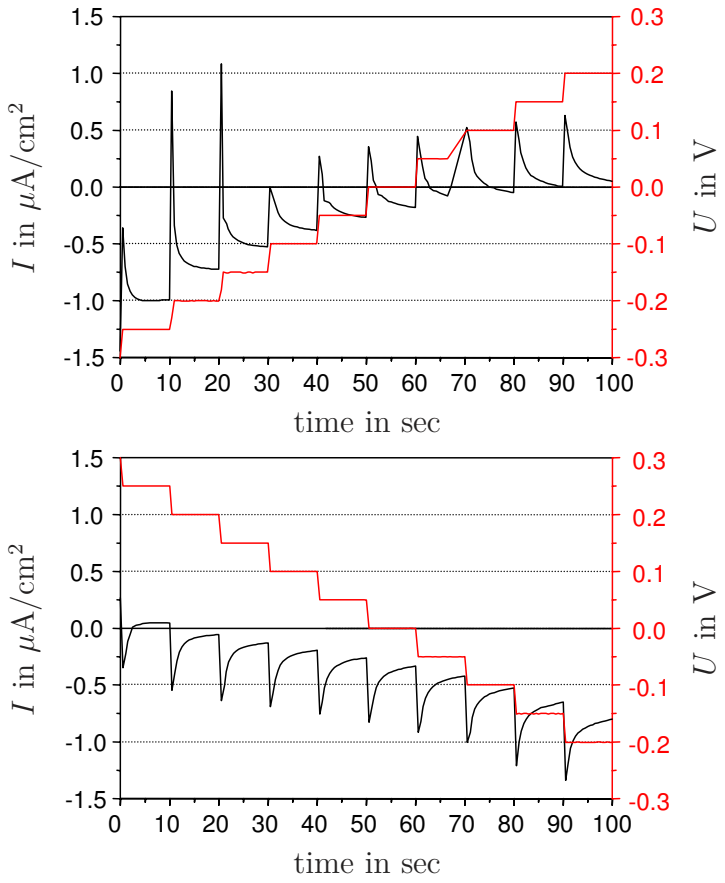

Figure 5.18: Current changes in time (black curve) in a TiO_2 / PTEBS device in light (100 mW/cm^2) induced by voltage switching (red line).

so that a reasonable compromise between measurement time and accuracy of the absolute magnitudes had to be made. We made sure, however, that the photocurrent and photovoltage were determined correctly within the required precision.

As mentioned above, we believe that ionic currents play a role in the electronic behaviour of our devices. An alternative explanation would be a capacitive charging of the device. However, the device behaviour observed in a control experiment cannot be fully explained by capacitive properties. We measured the voltage across a device which we kept in open circuit condition. It was first exposed to light (20 mW/cm^2) and then put in the dark. A few seconds after turning the light off, we short-circuited the device for a few seconds to allow any capacitive charge to discharge. The time dependent voltages measured during this procedure are shown in Fig. 5.19. The light was turned on at point a), resulting in a voltage peak similar in shape to the current peaks described above. The light was then turned off at point b), yielding another voltage peak with opposite sign and a slower decay characteristic. During this decay, at point c), we short-circuited the device and then returned it to open circuit condition. Naturally,

the voltage disappeared during the short circuit period, but then reappeared. This rebuilt voltage, in our opinion, cannot stem from electrostatic charges on the electrodes, since these would have discharged during the short circuit. We believe that less mobile charges, like ions in the polymer material, are responsible for the observed voltage.

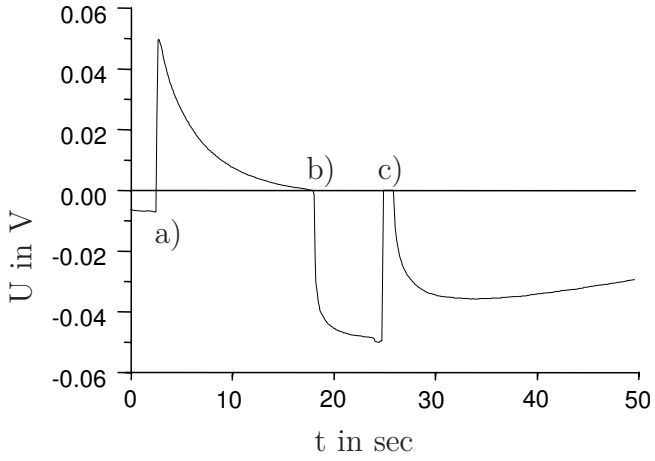

Figure 5.19: Voltage changes of a 'photobattery': the light is a) switched on, b) switched off, c) the circuit is shorted and opened again after 1 sec.

The behaviour of the TiO_2 / PTEBS device shown in Fig. 5.19 is comparable to a battery which is charged by exposing it to light, and then slowly releases charges after the light is switched off. The typical density of stored charges is rather low on the order of 10^5 As/m^3, as can be estimated from the transient photocurrents displayed in Fig. 5.16. This charge density is four orders of magnitude lower than in commercial batteries.

5.4 Summary and conclusions

We have found that functional polymers can be used as charged agents in the layer-by-layer self-assembly process. We successfully combined two functional materials, *n*-type TiO_2 nanoparticles and the light-absorbing *p*-type polymer PTEBS in hybrid hetero-films which we used as a basis for heterojunction devices. For the fabrication of polymer top layers, a refined drop-casting method was developed which gave superior results in terms of film homogeneity when compared to other solution based methods. The devices fabricated with these methods showed reliable and stable photovoltaic performance.

We focused on relations between structure and properties of our devices. We were able to do so because our method provided us with good control of layer thicknesses

and produced very reliable cell properties, with defective cells being basically absent when hole and electron blocking layers were included. We observed photovoltages of 0.6–0.9 V, which are on the order of the expected maximum defined by the effective gap, the difference between the TiO_2 CB and the PTEBS HOMO (estimated as 0.7–1.1 V [59, 71]). The band structure of the device itself is not ideal, in the sense that the effective gap is much smaller than the absorber band gap, see Fig. 5.2. The power conversion efficiency of our cells was very low, the best results were on the order of 2×10^{-3} %. Cells fabricated with the same materials but different fabrication methods were reported with higher photocurrents, but lower photovoltages in the literature [38, 83]. We believe that the low photocurrents are caused by inefficient charge separation and inferior charge transport properties.

We investigated the influence of both the TiO_2 and the PTEBS layers on charge transport in the cell. Decreases in photocurrent were observed if any of the layers was thicker than 1 μm. Especially the thickness and structure of the TiO_2 film had a significant influence. Annealing these films reduced the overall device resistance by a factor of two, improving the charge transport. Still, the resistance of the TiO_2 film was probably too high to allow for efficient cell operation.

We were able to draw conclusions regarding the rate of charge separation as the primary determinant of cell performance by isolating the influence of resistances using I/V curve analysis. The rate of charge separation in the cells was apparently low, indicating that the effective interface area was small. Experimental evidence was ambiguous with respect to the degree of pore filling by the polymer phase, which determines the size of the interface area. We believe that individual channels of penetrating polymers are formed, but that the overall infiltration is low.

Film thickness measurements suggest a penetration depth of PTEBS polymer on the order of a few hundred nanometers. It might be that the layer-by-layer self-assembly method produces a denser structure than other methods, limiting polymer diffusion. The use of larger particles for the porous film, however, might give larger voids which can be filled with polymers to a higher degree. The flexibility of the layer-by-layer self-assembly method with respect to materials, which we have demonstrated in this work, makes this a promising approach.

The investigation of the current / voltage behaviour yielded complex results with constant as well as transient current components. The time-dependent currents may be explained by movements of PTEBS counterions, which are a common feature of all polyelectrolytes that could be used in layer-by-layer self-assembly. These ions might act as traps for electrons, even though the electron density is small in p-type polymers.

Chapter 6

Quantum dot sensitized hybrid photovoltaic devices

6.1 Outline

In Section 2.3.4, we discussed the unique properties of semiconductor QDs as an absorber material in solar cells. We also outlined a hybrid cell design with a heterojunction structure for the efficient separation of photogenerated excitons, see Fig. 2.22. The experimental results reported in Chapter 5 demonstrate that with the layer-by-layer self-assembly method, sensitizing polymers can be incorporated into nanoparticulate TiO_2 thin films.

In this chapter, we present experiments to incorporate QDs as sensitizers into TiO_2 films, and use the films as electrodes in photovoltaic cells. We analyze these QD sensitized devices with respect to the functionality of the sensitizers, and with respect to the influence of device structure on the performance.

6.2 Device fabrication and electronic structure

6.2.1 Material properties

Quantum dot absorbers

The QDs used in this work were CdSe and CdTe nanocrystals capped with thioglycolic acid (TGA), see Table 3.2 for the chemical structure. The capping carries negative

charges on the carboxyl end group and solubilizes the QDs in water. The charges are important for the self-assembly process which relies on electrostatic interactions between different species. Further, the carboxyl end group is known as an efficient anchor group on TiO_2 surfaces and has been used for sensitization with dye molecules [145, 146].

Notice that the TGA capping of the QDs is much thinner than the commonly used TOPO capping. For efficient charge transfer processes, the distance between an absorbing chromophore and the acceptor is important, since the spatial overlap of the wavefunction of the donor state (e.g., the LUMO state of the chromophore) and the acceptor state (e.g., an empty CB state of a semiconductor) affects the transfer rate [25]. In our case, close contact between the chromophore, which is the core of the colloidal QD, and the TiO_2 acceptor is desirable. The effect of adding, e.g., alkane spacer groups between perylene chromophores and TiO_2 is an increase of the timescales of electron transfer [147]. Spacers with up to two CH_2 units, however, were shown to allow for electron transfer times around 50 fs. For comparison, the lifetime of biexcitons in PbSe QDs, described in Section 2.3.4, is on the order of picoseconds [31]. Therefore, we expect the TGA capping of our QDs, with an alkane chain with only one CH_2 unit, to be thin enough to allow for electron transfer on a timescale shorter than exciton annihilation. As discussed in Section 2.3.2, the relative timescales of exciton separation and recombination reactions crucially influence the efficiency of the charge creation in excitonic cells.

The band gaps of both CdSe and CdTe are rather narrow in the bulk, with band gap energies E_{gap} of 1.73 eV for CdSe [148] and 1.5 eV for CdTe [149]. With mean diameters of 3.0 nm (CdSe QDs) and 3.8 nm (CdTe QDs), both types of nanocrystals are in the confinement regime, since the Bohr exciton radii in the bulk are 5 nm (CdSe) [148] and 7.3 nm (CdTe) [149], respectively. Hence, we expect shifts of the CB and VB positions which result in an increased band gap energy. The masses of electrons in the CB and holes in the VB calculated from the band dispersions are $m_e^* = 0.11\, m_0$ and $m_h^* = 0.44\, m_0$ for CdSe according to [95], and CdTe $m_e^* = 0.096\, m_0$ and $m_h^* = 0.4\, m_0$ according to [92], where m_0 is the rest mass of the electron. Hence, from equation (2.37), the shift of the CB is expected to be about four times as large as the shift of the VB for both materials. We note again that we will use the terms CB and VB for the electronic levels of QDs even though they are spatially confined and discrete, corresponding to a quasi zero-dimensional density of states.

The exciton binding energies of the materials are on the order of meV in the bulk, 15 meV for CdSe [150, 151] and 10 meV for CdTe [92]. In confined spaces, an increase of the binding energies is expected [151]. Nevertheless, we will neglect the influence

of the binding energies on the optical properties in the following, since they are small compared to the observed band shifts.

The electron affinity (EA), the position of the CB bottom, is 4.79 eV for CdSe and 4.28 eV for CdTe in the bulk, respectively [152]. The ionization energy (IE), the position of the VB edge, is calculated from these data using the relation

$$\mathrm{IE} = \mathrm{EA} + E_{\mathrm{gap}} \tag{6.1}$$

as 6.52 eV for CdSe and 5.78 eV for CdTe. We will use these bulk values, the band shifts predicted by equation (2.37), and experimentally determined band gaps of the QDs to calculate the band structure of the dots. The corresponding experiments and the results of the calculations will be given in Section 6.3.2.

Hole transport polymer

We used the fluorene-triarylamine co-polymer TFB shown in Table 3.1, which has been used successfully in organic LEDs [153], as a hole conductor for our hybrid cells. It is very well suited for our purpose for several reasons: (i) The HOMO level (IE = 5.3 eV [154]) lies above the VB of both CdSe and CdTe, so that hole injection from both types of QDs seems possible. (ii) TFB is *p*-type and has a comparably high hole mobility of 0.01 $\mathrm{Vs/cm^2}$ [155, 156], so that good hole transport properties are expected. (iii) Since it is *p*-type, and from the position of the HOMO, the Fermi level position of TFB is estimated close to the work function of Au electrodes (5.2 eV, [157]), so that a hole injection barrier at the metal-organic interface is avoided [158]. (iv) The polymer has a HOMO-LUMO gap of 3.0 eV [154] which makes it transparent to most of the solar spectrum.

The benefit of using a transparent polymer is that the illumination of the QDs in the device is increased, leading to more excitons being generated directly at the heterointerface. Also, if the absorption spectra of the QDs and the polymer coincided, then both species would generate excitons in the same wavelength region. It would then be impossible to identify the source of photogenerated carriers from, e.g., spectrally resolved photocurrent measurements. The spectra will show photocurrents in the common absorption region, which could stem from separated excitons generated by absorption in either of the two materials [37].

Device electronic structure

We fabricated QD devices on FTO coated glass slides from Nippon Sheet Glass using the layer-by-layer self-assembly method. FTO with a work function of 4.4 eV served as a front electrode, and evaporated Au with a work function of 5.2 eV as a back electrode. TiO_2 nanoparticles (EA = 4.2–4.3 eV) sensitized with QDs were used as a porous electron transport film. The structure of these devices is shown in Fig. 6.1. The relative position of the Fermi levels of TiO_2 and of FTO yields an ohmic contact without significant injection barriers [59].

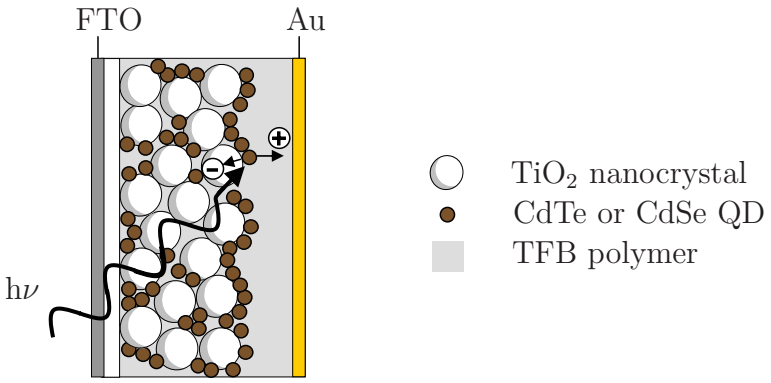

Figure 6.1: Structure of a FTO / TiO_2 / QD / TFB / Au device.

The electronic properties of the electrode materials, of TiO_2, of the absorber materials, and of the hole transport polymer TFB can be combined into the tentative band structure of our devices shown in Fig. 6.2. Notice that the diagrams are preliminary and simplifying in several aspects: (i) The expected confinement effect in the QD absorbers is a priori not quantitatively known and therefore not taken into account in the diagrams. (ii) The surface capping of the QDs might act as a CdS shell interfering with charge transfer [159], which is not shown. (iii) The transparent and isolating polyions which were used for film fabrication are not displayed. We expect that sufficient direct contact was made between the electronically functional materials, so that charge transfer circumvented these molecules. (iv) Direct contact between TiO_2 and TFB, as a further simplification, is also omitted. (v) Any band bending caused by Fermi level misalignment is neglected in this and in the following flat band diagrams. This approximation is justified by the generally low charge carrier densities and by the spatial interpenetration of n-type and p-type phases, which prevent the formation of space charge layers known from p-n homojunctions [54].

From the level diagrams in Fig. 6.2, conclusions with respect to device operation can be drawn, but they are preliminary owing to the simplifications mentioned above. The left

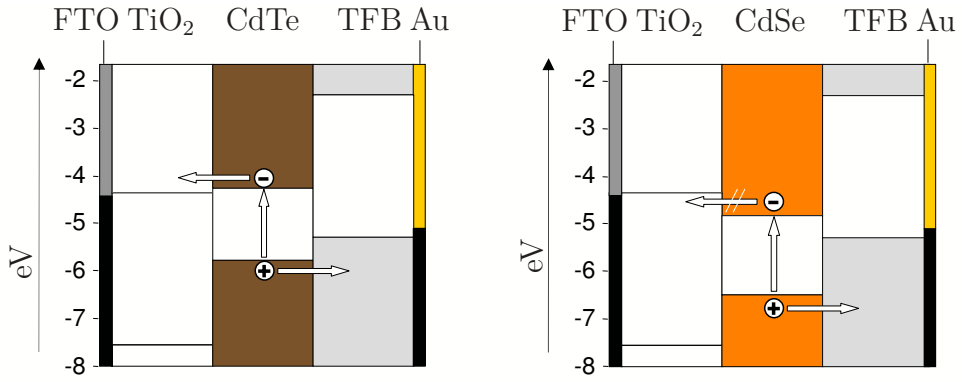

Figure 6.2: Flat band diagrams of the materials used in QD sensitized devices, showing the level positions in the bulk.

image shows the situation for CdTe as absorber material, the right image for CdSe. As discussed before, the contacts between the electrodes and the semiconductors TiO_2 and TFB are expected to be ohmic, yielding efficient charge injection. Hole injection from photoexcited QDs into the TFB hole conductor is allowed, while hole injection into TiO_2 is not allowed. The reason for this situation is that at the energy of the CdSe and CdTe VB edge, the density of electronic states in TiO_2 is zero, while a finite density of states available for hole transfer is present in TFB. Electron injection into TiO_2 seems only allowed from CdTe, and not from CdSe, since the CdSe CB edge is below the TiO_2 CB. Still, the confinement in CdSe QDs might lift the CB above the TiO_2 CB, making electron injection possible. For CdTe QDs, the confinement is not expected to yield qualitative changes of the relative band positions, so that charge injection is expected for CdTe QDs, but uncertain for CdSe QDs. In any case, the effective gap of the heterointerface will be determined by the difference between the TiO_2 CB and the TFB HOMO, which is calculated as 1.0–1.1 eV based on literature values.

6.2.2 Cell fabrication

Growth of QD / TiO_2 films

The layer-by-layer self-assembly method described in detail in Section 2.4 was employed to fabricate porous heterofilms of TiO_2 nanoparticles and either CdSe or CdTe QDs on FTO substrates, using the protocol described in Section 3.2.2. The devices were fabricated with compact TiO_2 underlayers as described in the Sections 3.2.1 and 5.2.2, unless noted otherwise. We obtained very homogeneously coated, brightly colored samples, as shown in Fig. 6.3. The colors were brown for CdTe samples and orange for

CdSe samples, very different from the CdTe solution color (dark red, opaque), but similar to the CdSe solution color (light red, translucent). The incorporated amount of QDs in the films was determined by surface composition analysis with XPS, and will be described in Section 6.3.1. From this data, we calculated the total absorption by the incorporated QDs, using experimentally determined extinction coefficients. We observed photobleaching of the CdTe samples when they were left in air and ambient light over weeks, but the CdSe samples were stable over several months.

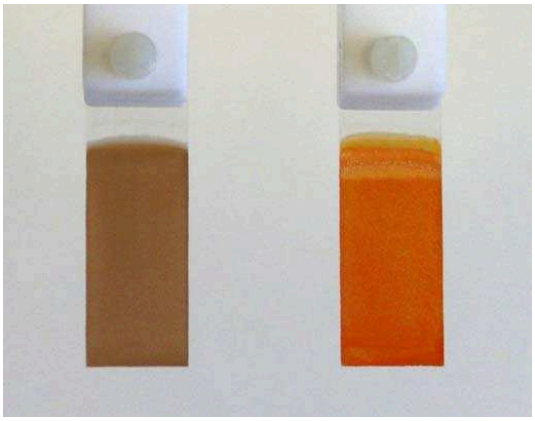

Figure 6.3: Glass slides coated with TiO_2 / QD (left: CdTe, right: CdSe) composite films.

Annealing attempts of QD / TiO_2 films

We attempted to anneal CdTe films in order to improve the contact between the particles and remove excess organic material. We heated samples to 450°C in air, either untreated or after a treatment with aqueous $CdCl_2$ solution (highly toxic), or in Ar. The $CdCl_2$ treatment is reported to prevent oxidation of Cd compounds and is used routinely to increase the performance of CdTe based solar cells [30, 160, 161]. $CdCl_2$ was applied either by dropping a solution onto the samples, or by soaking them in solution and slowly withdrawing the samples after 15 min.

All annealing attempts damaged the samples, as we observed from changes in sample color and from XPS investigations of the chemical structure of the surfaces, displayed in Fig. 6.5 in the results section. When sintered in air, the samples were bleached to an almost white color. XPS revealed that both the Te 3d and Te 4d core levels were shifted about 4 eV to higher binding energies, indicating the oxidation of CdTe to $CdTeO_3$. The oxidation cannot be observed in the Cd 3p and Cd 3d core levels [130]. The carbon content was reduced significantly, indicating the burning of organic material to gaseous

CO_2. $CdCl_2$ treatments only had a very limited effect in any case, yielding a slightly darker sample color in some of the treated areas, but equivalent XPS signals indicating CdTe oxidation. When sintered in Ar, the samples inevitably turned black. The carbon content was not reduced, leading us to conclude that the organic content was carbonized. Oxidation of CdTe was apparently avoided, since no shifts of the Te core levels were observed.

Both carbonization and oxidation rendered the samples unusable for photovoltaic applications. The experiments were not repeated for CdSe samples, instead, all CdTe and CdSe samples used in the experiments described below were not annealed.

Top layer fabrication

The structure requirements for the TFB hole transport phase are the same as for the PTEBS phase discussed in Chapter 5. The porous QD / TiO_2 structure should be filled with polymers so that the QDs are contacted and charges can be transferred to the back electrode. Further, the top surface of the samples should be covered with TFB completely to ensure a homogeneous back contact.

We dropped between 25 and 50 μl of a THF solution with 1.0 wt. % TFB onto a sample area of 3.0 cm^2. In order to distribute the polymers uniformly, we swept the long side of a plastic pipette tip that was in contact with the solution back and forth, until the solvent had evaporated. Unlike the doctor blading method [139], our method relies on only very gentle pressure and continuous and rather fast sweeping. After this initial distribution at room temperature, we placed the samples on a heater plate at 70°C and redissolved the polymers by dropping 100 μl of pure THF onto the sample. We continued the distribution of the solution by sweeping a pipette tip across the liquid film until all THF solvent had evaporated. This two-step process gave functional TFB films with a slightly inferior homogeneity when compared to samples prepared by the wire frame method presented in Chapter 5. This method was not applicable here because the adhesion of THF to copper wires is very low. On top of the polymer layer, Au back electrodes with a thickness of 120 nm and dimensions of $3 \times 6\,mm^2$ were fabricated in vacuum by sputter coating or by metal vapor deposition.

6.3 Results and Discussion

6.3.1 Film structure

We determined the thickness of self-assembled PDAC / TiO_2 / QD films by scratching thin lines of film off the sample and measuring the resulting step height by AFM. We obtained a growth rate of 18.8 nm/dipping cycle. The total thickness of samples with a drop-cast TFB layer on top was also measured by this method. We found a thickness of the top layer of 10.2 nm per dropped μl of 1.0 wt. % TFB solution, comparable to the results reported for PTEBS in Chapter 5.

We investigated the morphology of the bare self-assembled film by SEM. The images displayed in Fig. 6.4 show a rough surface with individual aggregates of particles. Their density, however, was much lower than on the surfaces of the TiO_2/PDAC samples (type C) described in Chapter 4. The cracks visible in the higher magnification image probably appeared while the sample was dried by heating, and, since a porous film structure is desirable, are not expected to decrease device performance. When the samples were left to dry in air for a couple of weeks, the cracks led to the detachment of parts of the film. In order to prevent this effect we processed the samples immediately after self-assembly, which also prevented photobleaching permanently.

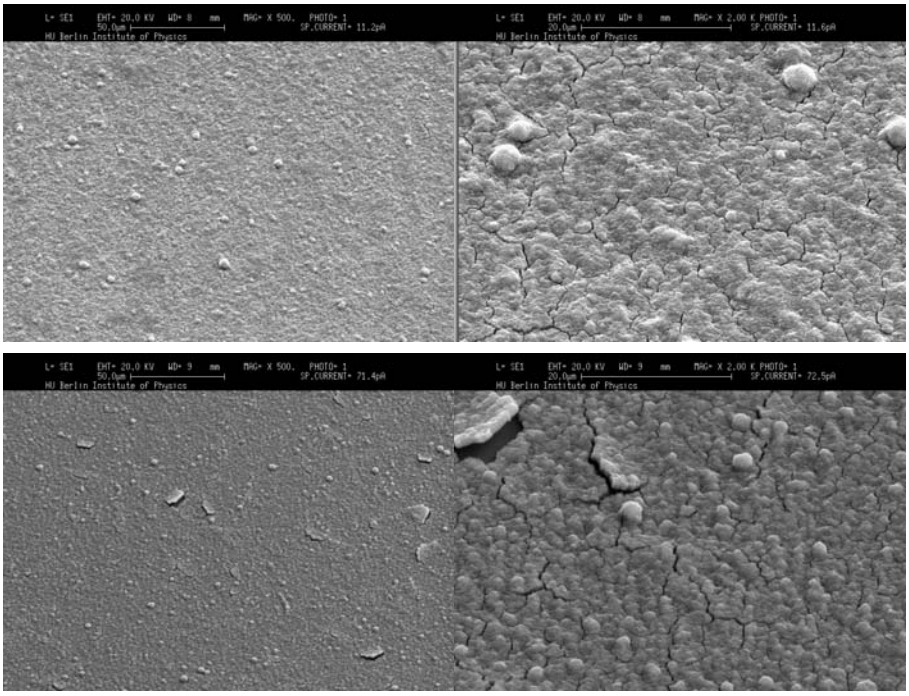

Figure 6.4: SEM images of TiO_2 / CdTe QD films, top: dried rapidly in an oven, bottom: slowly at room temperature, scan areas: $240 \times 160\,\mu m^2$ (left), $60 \times 40\,\mu m^2$ (right).

Surface composition analysis using the XPS data displayed in Fig. 6.5 was conducted to quantify the amount of CdTe QDs in the films. We integrated the count rates of the peak doublets of the core levels Ti 2p and Cd 3p and employed equation (4.7) using the ASFs of 1.8 (Ti 2p) and 1.6 (Cd 3p) [162], and the relative densities of Cd and Ti atoms in the two materials. A coverage ratio of 1.36:1 of Cd vs. Ti was obtained, indicating that 58% of the available TiO_2 surface is covered with QDs. This approach is justified since the escape depths of X-ray photoelectrons in both TiO_2 (2.1 nm) and CdTe (1.2 nm) are less than the particle sizes, so that only the first layer of particles at the film surface contributes to the XPS signal [135, 163]. The calculated coverage decreased to 51% when samples where annealed in air, as described in the preceding section, indicating that TiO_2 areas initially covered with organic material were exposed. This value confirms that more than half a monolayer of QDs has formed, and it corresponds to a ratio of 0.14 between the incorporated masses of CdTe and TiO_2, if one takes into account the different diameters and mass densities of the particles. This analysis was not repeated for CdSe QD samples. Since the surface chemistry governing the adsorption process is identical, we expect a similar coverage and a mass ratio of CdSe to TiO_2 of 0.11, owing to the smaller size of CdSe QDs.

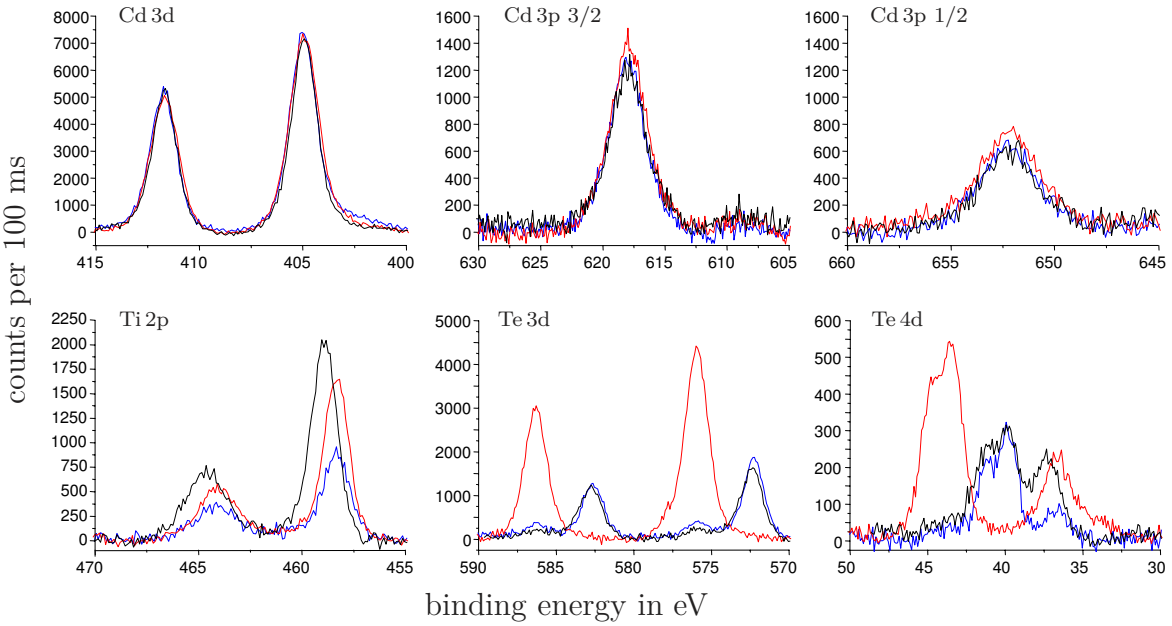

Figure 6.5: XPS signals from a TiO_2/CdTe sample before (blue line) and after annealing in air (red line) and Ar (black line) with the background signal removed and normalized to the Cd 3d peaks.

6.3.2 Photovoltaic behaviour

QD absorption and photocurrent action spectra

We measured the absorption spectra of CdSe QDs, CdTe QDs and TFB in solution and the spectral current behaviour of sensitized cells, in order to determine the band gap of the QDs and the spectral contributions of the respective materials to the photocurrents. The results of absorption and photocurrent measurements with 60 layer devices are displayed in Fig. 6.6 as a combined plot of arbitrarily scaled absorption spectra and the photocurrent spectra, which we display as the external quantum efficiency (EQE) of the cells. We calculated the EQE, a measure which is frequently used for the spectral characterization solar cells [30, 37, 164] using the following definition:

$$\mathrm{EQE} = \frac{N_{\mathrm{electrons}}/t}{N_{\mathrm{photons}}/t} \tag{6.2}$$

Here, $N_{\mathrm{electrons}}$ is the number of electrons that contribute to the external current and N_{photons} is the number of photons striking the cell surface, within a time period t at a certain wavelength. The number of electrons was determined by current measurements, and the number of photons was calculated from the spectrum of the light source. The colors of the graphs in Fig. 6.6 correspond to the different materials, brown for CdTe, orange for CdSe, and grey for TFB.

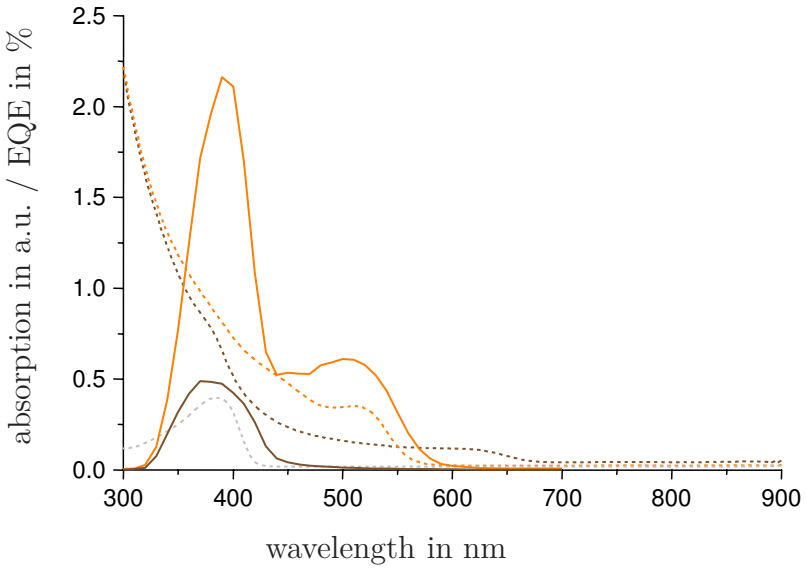

Figure 6.6: Absorption (dashed lines) of CdTe QDs (brown), CdSe QDs (orange), and TFB (grey) in solution and EQE (solid lines) of CdTe QD devices (brown) and CdSe QD devices (orange).

The onsets of absorption are observed between 500 and 600 nm for the QDs in solution (brown and orange dashed lines). We fitted Gaussian peaks to the rising edge of the QD absorption and took the center of these peaks as the energy of the transition with the lowest energy, which defines the optical gap of the dots. We found 516 nm for CdSe and 615 nm for CdTe, respectively. These positions yield gap energies of 2.40 eV (CdSe) and 2.02 eV (CdTe), corresponding to increases from the bulk values by 0.67 eV (CdSe) and 0.52 eV (CdTe). These properties clearly indicate confinement effects, with the gap increase being larger in the CdSe dots, which are smaller in size. According to equation (2.37), the EMA predicts the shifts of the CB and the VB as inversely proportional to the effective masses of electrons and holes, respectively. Using this result and the bulk data given in Section 6.2.1, we can calculate the band positions of our QDs. The following table summarizes the band gap increase, the new band gap, and the band positions relative to the vacuum level:

	CdSe QDs	CdTe QDs
ΔE_{gap}	0.67 eV	0.52 eV
E_{gap}	2.40 eV	2.02 eV
E_{CB}	-4.25 eV	-3.86 eV
E_{VB}	-6.65 eV	-5.88 eV

The photocurrent generated by the CdSe QD cells in the region between 480 nm and 600 nm (orange solid line) provides further indication of confinement effects. The contribution in this region can only stem from QD excitations, since neither TFB nor TiO_2 absorb beyond 480 nm. Therefore, confinement effects have apparently shifted the CdSe CB from the bulk situation shown in Fig. 6.2 to higher energies, so that electron injection from CdSe into TiO_2 is possible.

Unexpectedly, the CdTe QDs do not contribute to the photocurrent (brown solid line), even though their band positions would allow for both electron and hole injection. Evidently, the CdTe devices did not produce any photocurrent in the region between 480 nm and 670 nm, where the QDs absorb light. The only region where photocurrent is observed is between 320 nm and 480 nm, where TFB absorbs also. We believe this photocurrent is generated by excitons that are created in the TFB phase and separated at the TFB / TiO_2 interface.

CdSe devices show their highest photocurrent in the region where both CdSe QDs and TFB absorb, with a maximum EQE of 2.2% at 390 nm. We believe that a part of this photocurrent is generated by absorption in TFB, with a magnitude corresponding to the photocurrent of the CdTe cells which is entirely caused by TFB. However, CdSe QDs

are expected to account for the major part of the photocurrent in the region below 480 nm. The photocurrent cutoff at 320 nm observed for both types of devices is due to absorption by the glass front window.

The results of spectral measurements and the predictions of the EMA about the relative magnitudes of the band shifts allow us to draw the band diagram shown in Fig. 6.7, which depicts the level alignment in our devices. Arrows indicate observed excitations and injections of charge carriers.

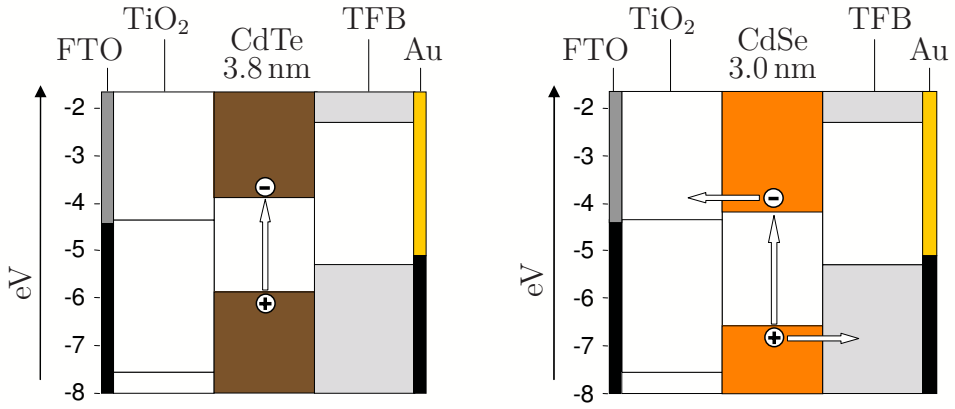

Figure 6.7: Flat band diagrams of QD devices with CdSe and CdTe QD band positions shifted by confinement.

We emphasize that the band structure shown for CdTe devices does *not* explain the absence of photocurrents. However, the existence of an effective CdS shell around the CdTe core, as discussed in Section 6.2.1, can explain this observation. Charge injection barriers between CdTe and TFB or CdTe and TiO_2 may be formed by CdS, since its band gap of 2.42 eV [165] is larger than the gap measured for the CdTe QD core (2.02 eV). The strong photoluminescence observed for this type of CdTe particles supports this explanation [120]. For CdSe QDs, a barrier may also exist, but it will be much more shallow since the observed CdSe QD band gap is 2.40 eV.

The absorption of the composite films cannot be measured by optical spectroscopy directly, because of the strong light scattering by TiO_2 particles. We *calculated* the absorbance of films with different thicknesses from the optical absorption of CdSe QDs measured in solution and the spatial concentration of QDs in the films obtained from XPS data in Section 6.3.1. Figure 6.8 shows the decadic absorbance A and the corresponding transmission T calculated from $T = 10^{-A}$. The displayed results indicate that close to the absorption edge, only 30% of the light is absorbed by the CdSe QDs in a 120 layer film, which is the thickest film we used, and correspondingly less in thinner films. Below 400 nm, more than 50% of the light is absorbed in thick films.

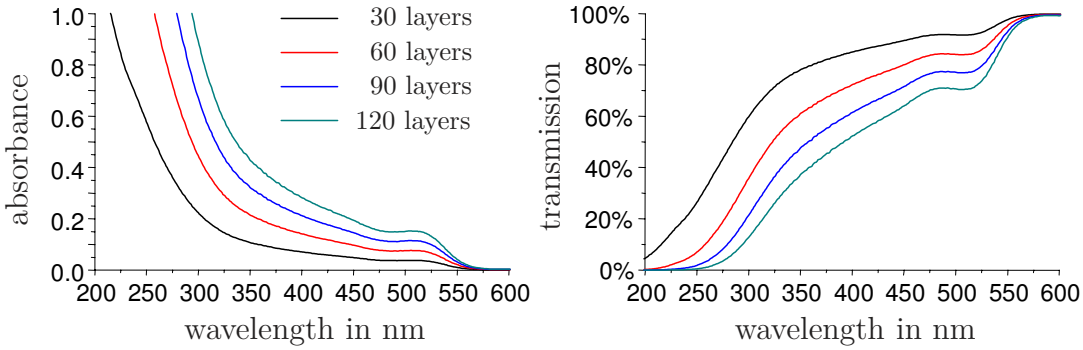

Figure 6.8: Calculated absorbance and transmission of films with a different number of CdSe QD layers.

From the transmission T and the EQE defined by equation (6.2), the internal photon-to-current conversion efficiency (IPCE) was calculated to characterize the efficiency of the QD absorbers [23, 139]:

$$\text{IPCE} = \frac{N_{\text{electrons}}/t}{(1-T)N_{\text{photons}}/t} \tag{6.3}$$

Here, $(1-T)N_{\text{photons}}$ is the number of photons that are absorbed by QDs. For a 60 layer CdSe device we calculated an IPCE of 3.8% at the absorption onset of the CdSe QDs (510 nm). Since QD sensitization was observed for CdSe QD cells, I/V curve characterizations with this type of cells were conducted and will be described below.

I / V curve characteristics and influence of film thickness

We fabricated CdSe QD sensitized cells with different thicknesses of both the porous inorganic layer and the polymer top layer, and measured their characteristics with the methods and equipment described in Chapter 3. Shorter delay times for I/V curve measurements than for the PTEBS cells described in Chapter 5 could be chosen, since no significant current changes over time were observed. Again, our cell fabrication method reliably produced operational cells. Figure 6.9 shows typical I/V curves from four devices placed on one sample with a 570 nm thick porous layer and a 250 nm thick TFB top layer. The solid lines represent the current under 100 mW/cm^2 white light illumination, the dashed lines, almost identical to the zero current level for all displayed voltages, were measured in the dark.

The curves measured in light show an S-like shape, characterized by a non-exponential current increase in forward bias. Similar curve shapes were observed for most devices. Also typical are the very low dark currents below the on-voltage, which was in the range

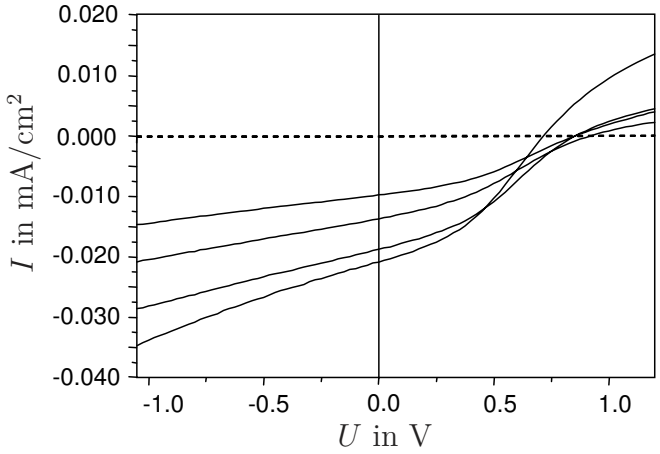

Figure 6.9: I/V curves of four devices on one TiO_2/CdSe QD/TFB sample in light (intensity 100 mW/cm^2, solid curves) and in the dark (dashed, very close to $I = 0$).

of 1 V. The photocurrents and photovoltages we measured for the devices depended on the layer thicknesses, which we varied systematically. The results of these variations are displayed in Fig. 6.10. The black lines and solid symbols are photocurrents, and the red lines and open symbols are photovoltages measured for different thicknesses of the porous TiO_2 / CdSe QD layer, which are plotted on the x-axis. Different symbols refer to different thicknesses of the TFB top layer, either 250 nm, marked with squares, or 510 nm, marked with triangles. The error bars are empirical standard deviations.[1] Each pair of I_{sc} and U_{oc} values displayed in Fig. 6.10 is based on a series of I/V curve measurements as shown in Fig. 6.9.

The highest photocurrents (solid black symbols) of up to 0.02 mA/cm^2 were observed for the thinnest porous layer (570 nm) combined with a thin TFB top layer (250 nm). I_{sc} decreased by a factor of five if either the TFB layer thickness or the porous layer thickness was doubled. Doubling both thicknesses gave a decrease by a factor of 10. Further increase of the porous layer thickness gave no systematic changes. Overall, the current behaviour is similar to the observations of the TiO_2 / PTEBS devices discussed in Chapter 5, as the currents tend to decrease with increasing film thicknesses.

The photovoltage U_{oc}, on the other hand, showed comparably little variation with layer thicknesses. U_{oc} maximum values above 1.1 V were observed for both TFB thicknesses at the medium porous layer thickness of 1140 nm. The thicker TFB layers (red open triangles) always gave a higher U_{oc} than the thin layers (red open squares). The smallest

[1] We note that the negative part of the I_{sc} confidence interval of the 570 nm porous layer / 510 nm TFB layer devices is, of course, not physical. Included photocurrents were all positive. The interval extension into the negative is an artefact produced by the calculation of the I_{sc} standard deviation as stddev $= \sqrt{\Sigma_i^n (x_i - \bar{x})^2/(n-1)}$, which is not strictly valid since the I_{sc} is not expected to be symmetrically distributed.

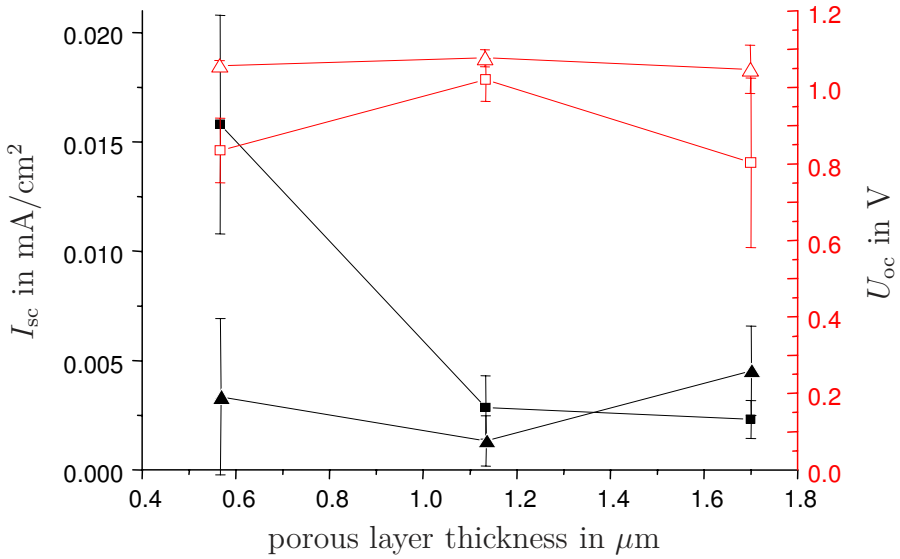

Figure 6.10: Photocurrents (black, solid symbols) and photovoltages (red, open symbols) of TiO_2/CdSe QD/TFB devices for different thicknesses of the TiO_2/CdSe QD film (x-axis) and of the TFB top layer (squares: 250 nm, triangles: 510 nm).

mean value of U_{oc} of approximately 0.8 V was measured for thin TFB layers combined with either very thin or very thick porous layers.

Apparently, the resistance of the individual layers has a dominant effect on the photocurrents. Thin films showed the highest currents, even though their absorption is lower than the absorption of thick films. Therefore, the higher currents must be caused by better transport properties. We believe that the thicker devices did not convert the larger number of photogenerated excitons into current because the hole conducting polymer TFB did not infiltrate the porous TiO_2 / CdSe structure deep enough. The device reproducibility was very high, especially for thick TFB top layers. These layers created the highest photovoltages, which matched or even slightly exceeded the calculated effective gap of the TiO_2 / TFB junction. A quantitative discussion of the photovoltaic parameters will be given in Section 6.4.

Performance of sintered devices

We attempted to reduce the resistance of the films by sintering our devices at 250°C for 2 hrs. Higher temperatures were not used in order to ensure that the polymer films were not damaged. Bare TiO_2 nanoparticle films are usually sintered at temperatures of 400–450°C [56], but we expect an enhancement of particle connectivity and contact between the phases also at lower sintering temperatures. Figure 6.11 shows the I/V curve measured in 100 mW/cm^2 illumination both before (dashed) and after sintering

(solid). The unsintered curves have already been displayed in Fig. 6.9, and are shown again here for comparison. The sintering dramatically changed the forward current behaviour of all devices and also increased all photocurrents and fill factors. These effects can be explained by a reduction of the serial resistance of the device, caused by an improved contact between the particles or between the electrodes and the transport phases.

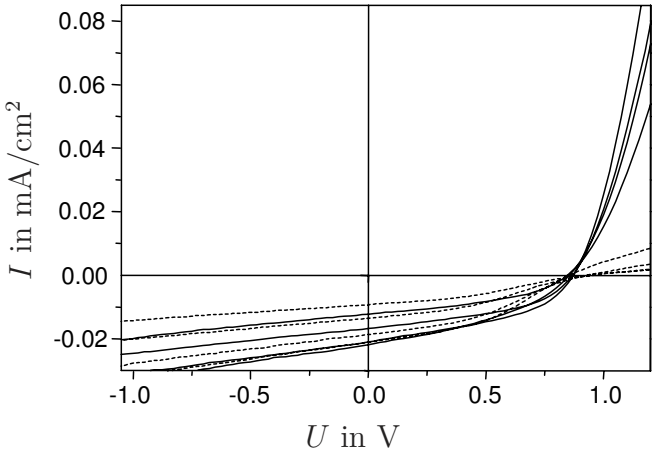

Figure 6.11: I/V curves in light of four devices on one TiO_2/CdSe QD/TFB sample before (dashed curves) and after sintering at 250°C (solid curves).

For a simulation of the I/V curve, we used a cell with a 280 nm thick porous TiO_2 / CdSe layer and a 250 nm thick TFB layer. The device had no compact TiO_2 layer and was sintered as described above. We measured I/V characteristics in 100 mW/cm^2 light and in the dark, and fitted the obtained curves using the diode model discussed in Section 2.2.1. A closed solution to equation (2.30) was employed as a fit function with I_0, n, I_{ph}, R_s, and R_{sh} as fit parameters, which we constrained to positive values. The light and dark curves were fitted with different sets of parameters and are displayed in Fig. 6.12.

For the illuminated device, we obtained $R_s = 3.8\,k\Omega cm^2$ and $R_{sh} = 21\,k\Omega cm^2$ for the device resistances. The shunt resistance R_{sh} is about a factor of 20 higher than in commercially available multicrystalline Si cells and therefore very satisfactory. Since high recombination rates are associated with low shunt resistances [166], recombination is apparently low here. The serial resistance, in contrast, falls dramatically short of the conductivity required for efficient operation. E.g., highly efficient silicon cells typically have serial resistances in the range of 0.5-1.3 Ωcm^2 [48, 167]. This deficiency reduces power output considerably. In the dark, both resistances were even higher, we found $R_s = 12\,k\Omega cm^2$ and $R_{sh} > 10\,M\Omega cm^2$.

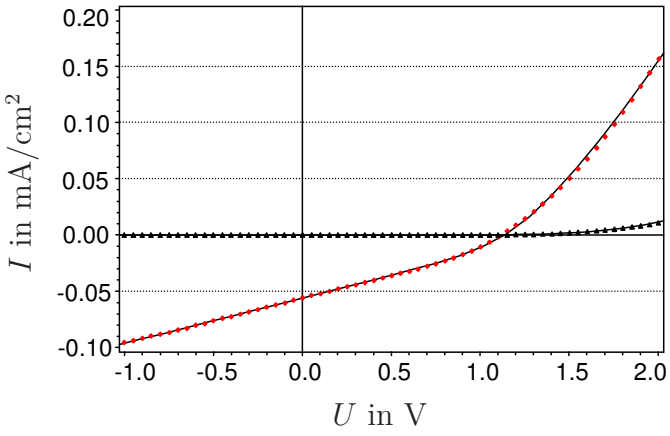

Figure 6.12: Measured I/V curves of a TiO_2/CdSe QD/TFB device in light (red diamonds), in the dark (black triangles), and fitted curves (diode model, solid lines).

The curve parameters of the I/V curve displayed in Fig. 6.12 are $I_{sc} = 0.058\,\mathrm{mA/cm^2}$, $U_{oc} = 1.08\,\mathrm{V}$, and $\mathrm{FF} = 31\%$ in white light. Combined according to equation (2.34), they give a power conversion efficiency of $\eta = 0.020\%$. The IPCE calculated according to equation (6.3) was 14.2% at the absorption onset of the CdSe QDs (510 nm), indicating that one in seven absorbed photons contributed to the external current. The photovoltage matches the effective gap of the cell and is also very satisfactory in absolute terms. The curve shape gives a rather low FF, but the dominating factor limiting cell performance is the photocurrent.

The curve measured in light shown in Fig. 6.12 is very similar to the simulated dot-dashed curve in the top image in Fig. 2.8. From a comparison with the long dashed simulated curve in that image, it is evident that lowering the serial resistance dramatically to $0.5\,\Omega\mathrm{cm^2}$ will increase the photocurrent by merely $0.006\,\mathrm{mA/cm^2}$. Apparently, the photocurrent of our cells is low *not only* because of the high serial resistance. Higher currents also require an improvement of independent factors such as the rate of carrier generation. If one achieves higher generation rates, then the high serial resistance will have an effect, as depicted in the middle and bottom images in Fig. 2.8. E.g., for the highest photocurrent, depicted in the bottom image, lowering the serial resistance to $0.5\,\Omega\mathrm{cm^2}$ will increase the photocurrent by more than $5\,\mathrm{mA/cm^2}$. Therefore, both the serial resistance and the carrier generation rate need to be addressed to increase performance.

6.4 Summary and conclusions

A combination of the layer-by-layer self-assembly method and drop-casting techniques was employed to fabricate hybrid heterojunction devices. All processing steps resulted in macroscopically homogeneous heterofilms. We used TiO_2 nanoparticles, colloidal CdX QDs (X = Se or Te), and TFB polymer as active components. The band alignments of these materials favor charge separation at the interfaces. The produced devices showed a pronounced photovoltaic effect and very reproducible and stable performance over months. From photocurrent action spectra we observed that CdTe QDs did not contribute to the generation of charge carriers. We attribute this finding to interface barriers created by the QD capping layer. CdSe QDs, in contrast, contributed to the photocurrents by carrier injection. The CdSe CB was shifted by confinement effects so that it allowed for carrier separation at the TiO_2 / CdSe QD / TFB interfaces.

Devices performed best when the active layer thickness was below $1\,\mu$m. High serial resistances of thicker films apparently limited the photocurrents. We found that brief sintering at 250°C improved device performance significantly and changed the behaviour in forward bias, indicating a reduced serial resistance. Fitting the observed I/V curves with the diode model from Section 2.2.1 revealed that the serial resistance of $R_s = 3.7\,\mathrm{k\Omega cm^2}$ was still too high to allow for efficient cell performance. Annealing the nanoparticle film in order to reduce the resistance was not successful, since the QDs did not survive the heating process.

We observed photovoltages of up to 1.15 V, indicating a well defined contact structure of the devices. High shunt resistances were measured, proving that carrier recombination in the devices was low. The photocurrents of up to $0.058\,\mathrm{mA/cm^2}$ obtained for sintered devices were almost one order of magnitude higher than in TiO_2 / PTEBS devices. We believe that this difference is caused by both better hole transport in the TFB polymer and higher rates of charge injection at the interface. The hole mobility in TFB is more than two orders of magnitude higher than the value of $6\times10^{-5}\,\mathrm{cm^2/Vs}$ reported for poly(3-hexylthiophene) (P3HT), a polymer with a chemical structure similar to PTEBS [155, 168]. Higher rates of charge injection can be explained by a more efficient charge separation at the TiO_2 / CdSe / TFB double-heterojunction. The higher rates were achieved even though the amount of absorber material was only a sub-monolayer on the TiO_2 surface, and not a bulk film as in the TiO_2 / PTEBS devices.

The measured power conversion efficiency of CdSe QD sensitized devices was up to $\eta = 0.020\%$. Limiting factors include insufficient absorption and low overall carrier generation efficiencies. Low values of the EQE with the maximum of a typical device found

at 2.2% indicated that the area of the charge separating interface was small. We believe that the porous heterofilms were not infiltrated completely by the hole conducting polymer. The carrier injection efficiency of colloidal CdSe QDs was calculated as an IPCE ratio of 14.2% at the absorption onset for very thin devices. This property also leaves space for device improvement. The performance of our cells is comparable to other cell concepts based on TiO_2 and polymers as conducting phases [169, 170], while cells with bulk QD phases performed significantly better [30]. We expect that a complete interpenetration of the semiconducting phases will improve performance considerably [39, 87]. Thicker films in the range of several micrometers with higher overall absorption could be used, if the film resistances are reduced significantly, e.g., by a sintering process which avoids oxidation of the QDs.

Chapter 7

Conclusions and outlook

In this work we investigated the potential of the electrostatic layer-by-layer self-assembly method with respect to the fabrication of solid state photovoltaic devices. The layer-by-layer growth process was improved so that it reliably produced macroscopically homogeneous thin films with controlled uniform thicknesses. Hybrid films composed of n-conductive, photocatalytic TiO_2 nanoparticles and polymers were grown with the self-assembly method and showed favorable structural properties in terms of the size and accessibility of the internal surface, the film composition, and light-scattering properties. In a second step, we grew films with incorporated light-absorbing polymers and semiconductor QDs with electronic level structures matching TiO_2. The self-assembly method proved to be very flexible with respect to materials as long as electrostatic interaction is present. This finding opens up a variety of constituent materials with useful optical properties, since ionic groups could possibly be added chemically to various light-absorbing particles and molecules without losing their optical properties.

We fabricated hybrid photovoltaic devices by further processing the layer-by-layer grown sensitized films, and characterized their electronic behaviour. Our methods produced highly reliable and very stable photovoltaic devices. We obtained comparably high photovoltages indicating a good choice of materials and well defined device structures.

TiO_2 / PTEBS cells showed photovoltages of up to 0.8 V, but the photocurrents were below 0.01 mA/cm^2 and the power conversion efficiencies were on the order of 2×10^{-3} % in standard illumination. We investigated the influence of device thickness and high temperature treatments on cell performance and concluded that low photocurrents were caused by incomplete interpenetration of the n-type and p-type phases and also by high film resistances. Further research work is necessary to increase the effective interface area formed during polymer drop-casting.

QD sensitized films were used to fabricate TiO_2 / CdX / TFB (X = Se, Te) devices. Effective sensitization by QDs could be proved for CdSe, and ruled out for CdTe by spectral measurements. The CdSe devices showed photovoltages of up to 1.15 V and photocurrents above 0.05 mA/cm^2, but TiO_2 / CdSe QD film thicknesses above 1 μm considerably reduced the latter. Sintering had a significant influence on cell characteristics and increased the power conversion efficiency to 0.020%. We attribute the conversion efficiencies, which exceed the performance of TiO_2 / PTEBS devices by one order of magnitude, to better *p*-type conductivity of the polymer and more efficient charge injection by the QDs. An increase of the interpenetration of *n*-type and *p*-type phases is again expected to raise the performance significantly. Further, increasing the conductivity of nanoparticulate films by, e.g., annealing remains a critical issue, since the oxidation of QDs has to be prevented in the process.

The structure of the hybrid devices needs to be improved in terms of particle contact and phase interpenetration. Polymer diffusion into the porous films could be increased by using larger particles and increasing pore sizes, or by reducing polymer molecular weight. The power conversion efficiency of a cell with the desired structural properties, i.e., a large interface area and efficient charge carrier transport, will depend crucially on the performance of the absorber materials. The requirements for efficient sensitizers include the following: (i) A high absorption cross section, which allows to keep the total film thicknesses and resistances low, (ii) an efficient charge injection behaviour, which is influenced by the shape and position of electronic donor and acceptor states, and (iii) a spectral absorption range reaching into the infrared combined with a mechanism to suppress thermalization losses in the high energy spectrum.

An exploitation of the charge carrier multiplication effect induced by confinement in several types of QDs could utilize excess energy of high energy photons and minimize thermalization, if multiple excitons are separated with high efficiencies [31–33]. This feature is most significant for small band gap, e.g., lead sulfide QDs absorbing in the infrared [109, 171–173], which make most of the solar spectrum accessible for photovoltaic energy conversion. Composite CdSe / CdTe QDs with tetrapod shape have been reported to feature spatially separated CB and VB, opening the perspective of highly efficient exciton separation [174]. We believe that the components and production methods described in this work represent a flexible cell design to utilize the novel optical properties of nanostructured materials for solar energy conversion.

Bibliography

[1] Y. Hamakawa. Solar PV energy conversion and the 21st century's civilization. *Solar Energy Materials and Solar Cells*, 74:13–23(11), October 2002.

[2] M. R. Smith. *The World Oil Supply Report 2004–2050*. Douglas-Westwood Limited, Canterbury, 2004.

[3] C. J. Campbell and J. H. Laherrere. The end of cheap oil. *Scientific American*, 278(3):60–5, 1998.

[4] C. Mandil. *International Energy Agency: World Energy Outlook 2006*. International Energy Agency, Paris, 2006.

[5] S. McDade. *United Nations Development Programme: Energizing the Millennium Development Goals*. International Energy Agency, Paris, 2005.

[6] J. Bohannon. Climate Change: IPCC Report Lays Out Options for Taming Greenhouse Gases. *Science*, 316(5826):812, 2007.

[7] R. R. Judkins, W. Fulkerson, and M. K. Sanghvi. The dilemma of fossil fuel use and global climate change. *Energy & Fuels*, 7(1):14–22, 1993.

[8] P. D. Quay, B. Tilbrook, and C. S. Wong. Oceanic Uptake of Fossil Fuel CO_2: Carbon-13 Evidence. *Science*, 256(5053):74, 1992.

[9] K. Caldeira and M. E. Wickett. Anthropogenic carbon and ocean pH. *Nature*, 425(6956):365–365, 2003.

[10] J. A. Turner. A Realizable Renewable Energy Future. *Science*, 285(5428):687–689, 1999.

[11] A. E. Becquerel. On electric effects under the influence of solar radiation. *Comptes Rendus de l'Académie des Sciences*, 9:711–4, 1839.

[12] J. Nitsch, W. Krewitt, M. Nast, P. Viebahn, S. Gärtner, M. Pehnt, G. Reinhardt, R. Schmidt, A. Uihlein, C. Barthel, M. Fischedick, and F. Merten. *Ökologisch optimierter Ausbau der Nutzung erneuerbarer Energien in Deutschland*. DLR Stuttgart, IFEU Heidelberg, WI Wuppertal, 2004.

[13] D. M. Chahn, C. S. Fuller, and G. L. Pearson. A new silicon p-n junction photocell for converting solar radiation into electrical power. *Journal of Applied Physics*, 25(5):676–680, 1954.

[14] M. A. Green. Crystalline and thin-film silicon solar cells: state of the art and future potential. *Solar Energy*, 74(3):181–192, 2003.

[15] M. A. Green. Recent developments in photovoltaics. *Solar Energy*, 76(1-3):3–8, 2004.

[16] J. Nijs, R. Mertens, R. van Overstraeten, J. Szlufcik, D. Hukin, and L. Frisson. Energy payback time of crystalline silicon solar modules. *Advances in Solar Energy*, 11:291–328, 1997.

[17] U. Fritsche. *Treibhausgasemissionen und Vermeidungskosten der nuklearen, fossilen und erneuerbaren Strombereitstellung*. Öko-Institut, Darmstadt, 2007.

[18] Wikipedia — The Free Encyclopedia. Online article: Photovoltaic array, 11/20/2007. `http://en.wikipedia.org/wiki/Photovoltaic_array`.

[19] M. A. Green. *Third Generation Photovoltaics: Advanced Solar Energy Conversion*. Springer, Hamburg, 2006.

[20] D. E. Carlson, S. T. F. Div, and P. A. Newtown. Amorphous-silicon solar cells. *IEEE Transactions on Electron Devices*, 36(12):2775–2780, 1989.

[21] M. A. Contreras, B. Egaas, K. Ramanathan, J. Hiltner, A. Swartzlander, F. Hasoon, and R. Noufi. Progress toward 20% efficiency in Cu(In,Ga)Se_2 polycrystalline thin-film solar cells. *Progress in photovoltaics*, 7(4):311–316, 1999.

[22] J. Fritsche, D. Kraft, A. Thißen, T. Mayer, A. Klein, and W. Jaegermann. Band energy diagram of CdTe thin film solar cells. *Thin Solid Films*, 403:252–257, 2002.

[23] S. E. Shaheen, C. J. Brabec, N. S. Sariciftci, F. Padinger, T. Fromherz, and J. C. Hummelen. 2.5% efficient organic plastic solar cells. *Applied Physics Letters*, 78 (6):841, 2001.

[24] H. Hoppe and N. S. Sariciftci. Organic solar cells: An overview. *Journal of Materials Research*, 19(7):1924–1945, 2004.

[25] A. Hagfeldt and M. Grätzel. Light-Induced Redox Reactions in Nanocrystalline Systems. *Chemical Reviews*, 95(1):49–68, 1995.

[26] A. J. Nozik. Quantum dot solar cells. *Physica E: Low-dimensional Systems and Nanostructures*, 14(1-2):115–120, 2002.

[27] M. Nanu, J. Schoonman, and A. Goossens. Nanocomposite three-dimensional solar cells obtained by chemical spray deposition. *Nano Letters*, 5(9):1716–1719, 2005.

[28] B. C. O'Regan and M. Grätzel. A low-cost, high-efficiency solar cell based on dye-sensitized colloidal TiO_2 films. *Nature*, 353(6346):737–740, 1991.

[29] C. J. Brabec, N. S. Sariciftci, and J. C. Hummelen. Plastic solar cells. *Advanced Functional Materials*, 11(1):15–26, 2001.

[30] I. Gur, N. A. Fromer, M. L. Geier, and A. P. Alivisatos. Air-Stable All-Inorganic Nanocrystal Solar Cells Processed from Solution. *Science*, 310(5747):462–465, 2005.

[31] R. D. Schaller and V. I. Klimov. High Efficiency Carrier Multiplication in PbSe Nanocrystals: Implications for Solar Energy Conversion. *Physical Review Letters*, 92(18):186601, 2004.

[32] R. J. Ellingson, M. C. Beard, J. C. Johnson, P. Yu, O. I. Micic, A. J. Nozik, A. Shabaev, and A. L. Efros. Highly Efficient Multiple Exciton Generation in Colloidal PbSe and PbS Quantum Dots. *Nano Letters*, 5(5):865–871, 2005.

[33] M. C. Beard, K. P. Knutsen, P. Yu, J. M. Luther, Q. Song, W. K. Metzger, R. J. Ellingson, and A. J. Nozik. Multiple Exciton Generation in Colloidal Silicon Nanocrystals. *Nano Letters*, 7(8):2506–2512, 2007.

[34] W. Shockley and H. J. Queisser. Detailed Balance Limit of Efficiency of p-n Junction Solar Cells. *Journal of Applied Physics*, 32(3):510, 1961.

[35] P. K. Chiang, C. L. Chu, Y. C. M. Yeh, P. Iles, and F. Ho. Progress toward high-efficiency ($> 24\%$) and low-cost multi-junction solar cell production. *Solar Energy Materials and Solar Cells*, 66(1):615–620, 2001.

[36] M. Yamaguchi. III-V compound multi-junction solar cells: present and future. *Solar Energy Materials and Solar Cells*, 75(1):261–269, 2003.

[37] W. U. Huynh, J. J. Dittmer, and A. P. Alivisatos. Hybrid Nanorod-Polymer Solar Cells. *Science*, 295(5564):2425–2427, 2002.

[38] Q. Qiao and J. T. McLeskey Jr. Water-soluble polythiophene/nanocrystalline TiO_2 solar cells. *Applied Physics Letters*, 86:153501, 2005.

[39] K. M. Coakley and M. D. McGehee. Photovoltaic cells made from conjugated polymers infiltrated into mesoporous titania. *Applied Physics Letters*, 83:3380, 2003.

[40] G. Decher. Fuzzy nanoassemblies: Toward Layered Polymeric Multicomposites. *Science*, 277:1232–1237, 1997.

[41] Y. Lvov, K. Ariga, M. Onda, I. Ichinose, and T. Kunitake. Alternate assembly of ordered multilayers of SiO_2 and other nanoparticles and polyions. *Langmuir*, 13(23):6195–6203, 1997.

[42] A. G. Agrios, I. Cesar, P. Comte, M. K. Nazeeruddin, and M. Grätzel. Nanostructured composite films for dye-sensitized solar cells by electrostatic layer-by-layer deposition. *Chemistry of materials*, 18(23):5395–5397, 2006.

[43] J. A. He, R. Mosurkal, L. A. Samuelson, L. Li, and J. Kumar. Dye-sensitized Solar Cell Fabricated by Electrostatic Layer-by-Layer Assembly of Amphoteric TiO_2 Nanoparticles. *Langmuir*, 19(6):2169–2174, 2003.

[44] B. A. Gregg. The photoconversion mechanism of excitonic solar cells. *MRS Bulletin*, 30(1):20–22, 2005.

[45] S. M. Sze. *Physics of Semiconductor Devices*. Wiley-Interscience, New York, 2007.

[46] B. Van Zeghbroeck. *Principles of Semiconductor Devices*. Electrical and Computer Engineering Department, University of Colorado at Boulder, 2004.

[47] H. Freyhardt, F. U. Hillebrecht, E. Kisker, H. Kronmüller, M. Lambeck, P. Luger, H. Nelkowski, U. Scherz, W. Schilling, and L. Thomas. *Bergmann-Schäfer, Lehrbuch der Experimentalphysik, Festkörper, Band 6*. Walter de Gruyter, Berlin-New York, 1992.

[48] C. Honsberg and S. Bowden. *Photovoltaics: devices, systems and applications PVCDROM 1.0*. University of Delaware, 1999.

[49] H. J. Queisser. Forward Characeristics and Efficiencies of Silicon Solar Cells. *Solid-State Electronics*, 5:1–10, 1962.

[50] N. W. Ashcroft and N. D. Mermin. *Festkörperphysik*. Oldenbourg, München, 2001.

[51] M. Wolf and H. Rauschenbach. Series resistance effects on solar cell measurements. *Advanced Energy Conversion*, 3(2):455–479, 1963.

[52] Q. Qiao. *Green Organic Solar Cells from a Water Soluble Polymer and Nancrystalline TiO_2*. PhD thesis, Virginia Commonwealth University, 2006.

[53] M. S. Tyagi. *Introduction to semiconductor materials and devices*. Wiley, New York, 1991.

[54] B. A. Gregg and M. C. Hanna. Comparing organic to inorganic photovoltaic cells: Theory, experiment, and simulation. *Journal of Applied Physics*, 93(6): 3605, 2003.

[55] J. A. Barker, C. M. Ramsdale, and N. C. Greenham. Modeling the current-voltage characteristics of bilayer polymer photovoltaic devices. *Physical Review B*, 67(7): 75205, 2003.

[56] M. Grätzel. Photoelectrochemical cells. *Nature*, 414:338–344, 2001.

[57] J. Bisquert, D. Cahen, G. Hodes, S. Ruhle, and A. Zaban. Physical chemical principles of photovoltaic conversion with nanoparticulate, mesoporous dye-sensitized solar cells. *The Journal of Physical Chemistry B*, 108(24):8106–8118, 2004.

[58] L. M. Peter. Characterization and Modeling of Dye-Sensitized Solar Cells. *Journal of Physical Chemistry C*, 111(18):6601–6612, 2007.

[59] Q. Qiao, J. Beck, R. Lumpkin, J. Pretko, and J. T. McLeskey Jr. A comparison of fluorine tin oxide and indium tin oxide as the transparent electrode for P3OT/TiO_2 solar cells. *Solar Energy Materials and Solar Cells*, 90(7-8):1034–1040, 2006.

[60] K. D. Benkstein, N. Kopidakis, J. van de Lagemaat, and A. J. Frank. Influence of the percolation network geometry on electron transport in dye-sensitized titanium dioxide solar cells. *The Journal of Physical Chemistry B*, 107(31):7759–7767, 2003.

[61] S. R. Forrest. The Limits to Organic Photovoltaic Cell Efficiency. *MRS Bulletin*, 5(V30), 2005.

[62] C. J. Brabec, J. A. Hauch, P. Schilinsky, and C. Waldauf. Production Aspects of Organic Photovoltaics and Their Impact on the Commercialization. *MRS Bulletin*, 30:51, 2005.

[63] M. C. Scharber, D. Mühlbacher, M. Koppe, P. Denk, C. Waldauf, A. J. Heeger, and C. J. Brabec. Design Rules for Donors in Bulk-Heterojunction Solar Cells—Towards 10% Energy-Conversion Efficiency. *Advanced Materials*, 18:789–794, 2006.

[64] P. Peumans, S. Uchida, and S. R. Forrest. Efficient bulk heterojunction photovoltaic cells using small-molecular-weight organic thin films. *Nature*, 425(6954): 158–162, 2003.

[65] F. Yang, M. Shtein, and S. R. Forrest. Controlled growth of a molecular bulk heterojunction photovoltaic cell. *Nature Materials*, 4(1):37–41, 2005.

[66] P. Peumans and S. R. Forrest. Very-high-efficiency double-heterostructure copper phthalocyanine/C_{60} photovoltaic cells. *Applied Physics Letters*, 79(1):126–128, 2001.

[67] J. Xue, B. P. Rand, S. Uchida, and S. R. Forrest. A hybrid planar-mixed molecular heterojunction photovoltaic cell. *Advanced Materials*, 17(1):66–71, 2005.

[68] M. Law, L. E. Greene, J. C. Johnson, R. Saykally, and P. Yang. Nanowire dye-sensitized solar cells. *Nature Materials*, 4(6):455–459, 2005.

[69] S. Hore, P. Nitz, C. Vetter, C. Prahl, M. Niggemann, and R. Kern. Scattering spherical voids in nanocrystalline TiO_2 - enhancement of efficiency in dye-sensitized solar cells. *Chemical Communications*, 2005(15):2011–2013, 2005.

[70] S. Hore, C. Vetter, R. Kern, H. Smit, and A. Hinsch. Influence of scattering layers on efficiency of dye-sensitized solar cells. *Solar Energy Materials and Solar Cells*, 90(9):1176–1188, 2006.

[71] F. Boccuzzi, E. Guglielminotti, and G. Spoto. Vibrational and electronic effects of NO chemisorption on TiO_2 and Ru/TiO_2. *Surface Science*, 251:1069–1074, 1991.

[72] H. Reiss. The Fermi level and the redox potential. *The Journal of Physical Chemistry*, 89(18):3783–3791, 1985.

[73] J. R. Durrant, S. A. Haque, and E. Palomares. Photochemical energy conversion: from molecular dyads to solar cells. *Chemical Communications*, 2006(31):3279–3289, 2006.

[74] W. R. Duncan and O. V. Prezhdo. Theoretical Studies of Photoinduced Electron Transfer in Dye-Sensitized TiO_2. *Annual Review of Physical Chemistry*, 58:143–84, 2007.

[75] M. Grätzel. Solar Energy Conversion by Dye-Sensitized Photovoltaic Cells. *Inorganic Chemistry*, 44(20):6841–6851, 2005.

[76] I. Mora-Seró and J. Bisquert. Fermi Level of Surface States in TiO_2 Nanoparticles. *Nano Letters*, 3(7), 2003.

[77] A. Hagfeldt, B. Didriksson, T. Palmqvist, H. Lindstroem, S. Soedergren, H. Rensmo, and S. E. Lindquist. Verification of high efficiencies for the Graetzel-cell. *Solar Energy Materials and Solar Cells*, 31:481–488, 1994.

[78] U. Bach, D. Lupo, P. Comte, J. E. Moser, F. Weissörtel, J. Salbeck, H. Spreitzer, and M. Grätzel. Solid-state dye-sensitized mesoporous TiO_2 solar cells with high photon-to-electron conversion efficiencies. *Nature*, 395(6702):583–585, 1998.

[79] G. M. Lowman, H. Tokuhisa, J. L. Lutkenhaus, and P. T. Hammond. Novel solid-state polymer electrolyte consisting of a porous layer-by-layer polyelectrolyte thin film and oligoethylene glycol. *Langmuir*, 20(22):9791–9795, 2004.

[80] B. C. O'Regan and F. Lenzmann. Charge Transport and Recombination in a Nanoscale Interpenetrating Network of n-Type and p-Type Semiconductors: Transient Photocurrent and Photovoltage Studies of TiO_2/Dye/CuSCN Photovoltaic Cells. *The Journal of Physical Chemistry B*, 108(14):4342–4350, 2004.

[81] K. M. Coakley, Y. Liu, C. Goh, and M. D. McGehee. Ordered Organic–Inorganic Bulk Heterojunction Photovoltaic Cells. *MRS Bulletin*, 30:37, 2005.

[82] D. C. Olson, J. Piris, R. T. Collins, S. E. Shaheen, and D. S. Ginley. Hybrid photovoltaic devices of polymer and ZnO nanofiber composites. *Thin Solid Films*, 496(1):26–29, 2006.

[83] Q. Qiao, L. Su, J. Beck, and J. T. McLeskey Jr. Characteristics of water-soluble polythiophene:TiO_2 composite and its application in photovoltaics. *Journal of Applied Physics*, 98:094906, 2005.

[84] B. Peng, G. Jungmann, C. Jäger, D. Haarer, H. W. Schmidt, and M. Thelakkat. Systematic investigation of the role of compact TiO_2 layer in solid state dye-sensitized TiO_2 solar cells. *Coordination Chemistry Reviews*, 248(13-14):1479–1489, 2004.

[85] Q. Fan, B. McQuillin, A. K. Ray, M. L. Turner, and A. B. Seddon. High density, non-porous anatase titania thin films for device applications. *Journal of Physics D: Applied Physics*, 33(21):2683–2686, 2000.

[86] C. Y. Kwong, W. C. H. Choy, A. B. Djurisic, P. C. Chui, K. W. Cheng, and W. K. Chan. Poly(3-hexylthiophene)-TiO_2 nanocomposites for solar cell applications. *Nanotechnology*, 15(9):1156–1161, 2004.

[87] K. M. Coakley, Y. Liu, M. D. McGehee, K. L. Frindell, and G. D. Stucky. Infiltrating Semiconducting Polymers into Self-Assembled Mesoporous Titania Films for Photovoltaic Applications. *Advanced Functional Materials*, 13(4):301–306, 2003.

[88] A. P. Alivisatos. Semiconductor clusters, nanocrystals, and quantum dots. *Science*, 271(5251):933–937, 1996.

[89] S. Coe, W. K. Woo, M. Bawendi, and V. Bulovic. Electroluminescence from single monolayers of nanocrystals in molecular organic devices. *Nature*, 420(6917):800–803, 2002.

[90] W. C. W. Chan, D. J. Maxwell, X. Gao, R. E. Bailey, M. Han, and S. Nie. Luminescent quantum dots for multiplexed biological detection and imaging. *Current Opinion in Biotechnology*, 13(1):40–46, 2002.

[91] D. Loss and D. P. DiVincenzo. Quantum computation with quantum dots. *Physical Review A*, 57(1):120–126, 1998.

[92] Y. Masumoto and K. Sonobe. Size-dependent energy levels of CdTe quantum dots. *Physical Review B*, 56(15):9734–9737, 1997.

[93] J. Perez-Conde and A. K. Bhattacharjee. Electronic structure of CdTe nanocrystals: A tight-binding study. *Solid State Communications*, 110(259-264), 1999.

[94] S. Sapra and D. D. Sarma. Evolution of the electronic structure with size in II-VI semiconductor nanocrystals. *Physical Review B*, 69(12):125304, 2004.

[95] A. E. Raevskaya, A. L. Stroyuk, S. Y. Kuchmiy, Y. M. Azhniuk, V. M. Dzhagan, V. O. Yukhymchuk, and M. Y. Valakh. Growth and spectroscopic characterization

of CdSe nanoparticles synthesized from $CdCl_2$ and Na_2SeSO_3 in aqueous gelatine solutions. *Colloids and Surfaces A: Physicochemical and Engineering Aspects*, 290 (1-3):304–309, 2006.

[96] J. Y. Marzin, J. M. Gérard, A. Izraël, D. Barrier, and G. Bastard. Photoluminescence of Single InAs Quantum Dots Obtained by Self-Organized Growth on GaAs. *Physical Review Letters*, 73(5):716–719, 1994.

[97] C. B. Murray, S. Sun, W. Gaschler, H. Doyle, and T. Betley. Colloidal synthesis of nanocrystals and nanocrystal superlattices. *IBM Journal of Research and Development*, 45(1):47–56, 2001.

[98] C. B. Murray, D. J. Norris, and M. G. Bawendi. Synthesis and characterization of nearly monodisperse CdE(E= S, Se, Te) semiconductor nanocrystallites. *Journal of the American Chemical Society*, 115(19):8706–8715, 1993.

[99] M. Kuno, J. K. Lee, B. O. Dabbousi, F. V. Mikulec, and M. G. Bawendi. The Band-Edge Luminescence of Surface-Modified CdSe Nanocrystallites-Probing the Luminescing State. *Journal of Chemical Physics*, 106(23):9869–9882, 1997.

[100] V. I. Klimov. Optical nonlinearities and ultrafast carrier dynamics in semiconductor nanocrystals. *The Journal of Physical Chemistry B*, 104(26):6112–6123, 2000.

[101] A. Zaban, O. I. Micic, B. A. Gregg, and A. J. Nozik. Photosensitization of Nanoporous TiO_2 Electrodes with InP Quantum Dots. *Langmuir*, 14(12):3153–3156, 1998.

[102] S. Gunes, H. Neugebauer, N. S. Sariciftci, J. Roither, M. Kovalenko, G. Pillwein, and W. Heiss. Hybrid solar cells using HgTe nanocrystals and nanoporous TiO_2 electrodes. *Advanced Functional Materials*, 16(8):1095–1099, 2006.

[103] A. J. Nozik. SPECTROSCOPY AND HOT ELECTRON RELAXATION DYNAMICS IN SEMICONDUCTOR QUANTUM WELLS AND QUANTUM DOTS. *Annual Review of Physical Chemistry*, 52(1):193–231, 2001.

[104] R. Heitz, H. Born, F. Guffarth, O. Stier, A. Schliwa, A. Hoffmann, and D. Bimberg. Existence of a phonon bottleneck for excitons in quantum dots. *Physical Review B*, 64(24):241305, 2001.

[105] Y. Yin and A. P. Alivisatos. Colloidal nanocrystal synthesis and the organic-inorganic interface. *Nature*, 437(7059):664–670, 2005.

[106] I. Robel, V. Subramanian, M. Kuno, and P. V. Kamat. Quantum Dot Solar Cells. Harvesting Light Energy with CdSe Nanocrystals Molecularly Linked to Mesoscopic TiO_2 Films. *Journal of the American Chemical Society*, 128(7):2385–2393, 2006.

[107] L. Cuadra, A. Martí, and A. Luque. Present status of intermediate band solar cell research. *Thin Solid Films*, 451:593–599, 2004.

[108] N. C. Greenham, X. Peng, and A. P. Alivisatos. Charge separation and transport in conjugated-polymer/semiconductor-nanocrystal composites studied by photoluminescence quenching and photoconductivity. *Physical Review B*, 54(24):17628–17637, 1996.

[109] R. Vogel, P. Hoyer, and H. Weller. Quantum-Sized PbS, CdS, Ag_2S, Sb_2S_3, and Bi_2S_3 Particles as Sensitizers for Various Nanoporous Wide-Bandgap Semiconductors. *The Journal of Physical Chemistry*, 98(12):3183–3188, 1994.

[110] R. Könenkamp, L. Dloczik, K. Ernst, and C. Olesch. Nano-structures for solar cells with extremely thin absorbers. *Physica E: Low-dimensional Systems and Nanostructures*, 14(1-2):219–223, 2002.

[111] K. Ernst, A. Belaidi, and R. Könenkamp. Solar cell with extremely thin absorber on highly structured substrate. *Semiconductor Science and Technology*, 18(6): 475–479, 2003.

[112] G. Decher, J. D. Hong, and J. Schmitt. Buildup of ultrathin multilayer films by a self-assembly process. III: Consecutively alternating adsorption of anionic and cationic polyelectrolytes on charged surfaces. *Thin solid films*, 210(1-2):831–835, 1992.

[113] Y. Lvov, G. Decher, and H. Möhwald. Assembly, structural characterization, and thermal behavior of layer-by-layer deposited ultrathin films of poly(vinylsulfate) and poly(allylamine). *Langmuir*, 9(2):481–486, 1993.

[114] N. A. Kotov, I. Dekany, and J. H. Fendler. Layer-by-Layer Self-Assembly of Polyelectrolyte-Semiconductor Nanoparticle Composite Films. *The Journal of Physical Chemistry*, 99(35):13065–13069, 1995.

[115] K. Schulze and S. Kirstein. Layer-by-layer deposition of TiO_2 nanoparticles. *Applied Surface Science*, 246(4):415–419, 2005.

[116] D. S. Kommireddy, A. A. Patel, T. G. Shutava, D. K. Mills, and Y. M. Lvov. Layer-by-Layer Assembly of TiO_2 Nanoparticles for Stable Hydrophilic Biocompatible Coatings. *Journal of Nanoscience and Nanotechnology*, 5(7):1081–1087, 2005.

[117] H. Ai, H. Meng, I. Ichinose, S. A. Jones, D. K. Mills, Y. M. Lvov, and X. Qiao. Biocompatibility of layer-by-layer self-assembled nanofilm on silicone rubber for neurons. *Journal of Neuroscience Methods*, 128(1-2):1–8, 2003.

[118] G. B. Sukhorukov, E. Donath, H. Lichtenfeld, E. Knippel, M. Knippel, and A. Budde. Layer-by-layer self assembly of polyelectrolytes on colloidal particles. *Colloids and Surfaces A: Physicochemical and Engineering Aspects*, 137(1): 253–266, 1998.

[119] H. Ai, M. Fang, S. Jones, and Y. Lvov. Electrostatic layer-by-layer nano-assembly on biological microtemplates: platelets. *Biomacromolecules*, 3(3):560–564, 2002.

[120] C. Lesser, M. Gao, and S. Kirstein. Highly luminescent thin films from alternating deposition of CdTe nanoparticles and polycations. *Materials science & engineering C: Biomimetic materials, sensors and systems*, 8:159–162, 1999.

[121] M. Gao, C. Lesser, S. Kirstein, H. Möhwald, A. L. Rogach, and H. Weller. Electroluminescence of different colors from polycation/CdTe nanocrystal self-assembled films. *Journal of Applied Physics*, 87(5), 2000.

[122] S. Bourbon, M. Gao, and S. Kirstein. Electroluminescence of self-assembled films of poly(p-phenylene vinylene) and J-aggregates. *Synthetic Metals*, 101(1-3):152–153, 1999.

[123] A. L. Rogach, L. Katsikas, A. Kornowski, D. Su, A. Eychmüller, and H. Weller. Synthesis and characterization of thiol-stabilized CdTe nanocrystals. *Berichte der Bunsen-Gesellschaft für Physikalische Chemie*, 100(11):1772–1778, 1996.

[124] M. Gao, S. Kirstein, H. Möhwald, A. L. Rogach, A. Kornowski, A. Eychmüller, and H. Weller. Strongly Photoluminescent CdTe Nanocrystals by Proper Surface Modification. *The Journal of Physical Chemistry B*, 102(43):8360–8363, 1998.

[125] H. Zhang, Z. Cui, Y. Wang, K. Zhang, X. Ji, C. Lue, B. Yang, and M. Gao. From Water-Soluble CdTe Nanocrystals to Fluorescent Nanocrystal–Polymer Transparent Composites Using Polymerizable Surfactants. *Advanced Materials*, 15(10): 777–780, 2003.

[126] H. Bao, Y. Gong, Z. Li, and M. Gao. Enhancement Effect of Illumination on the Photoluminescence of Water-Soluble CdTe Nanocrystals: Toward Highly Fluorescent CdTe/CdS Core-Shell Structure. *Chemistry of Materials*, 16(20):3853–3859, 2004.

[127] C. Tedeschi, H. Möhwald, and S. Kirstein. Polarity of layer-by-layer deposited polyelectrolyte films as determined by pyrene fluorescence. *Journal of the American Chemical Society*, 123(5):954–960, 2001.

[128] A. K. Hassan, N. B. Chaure, A. K. Ray, A. V. Nabok, and S. Habesch. Structural and electrical studies on sol-gel derived spun TiO_2 thin films. *Journal of Physics D: Applied Physics*, 36(9):1120–1125, 2003.

[129] N. B. Chaure, A. K. Ray, and R. Capan. Sol-gel derived nanocrystalline titania thin films on silicon. *Semiconductor Science and Technology*, 20(8):788–792, 2005.

[130] J. F. Moulder, W. F. Stickle, P. E. Sobol, K. D. Bomben, and J. Chastain. *Handbook of X-ray Photoelectron Spectroscopy: A Reference Book of Standard Spectra for Identification and Interpretation of XPS Data*. Physical Electronics, Minnesota, 1995.

[131] D. Briggs, D. M. Brewis, and M. B. Konieczo. X-ray photoelectron spectroscopy studies of polymer surfaces. *Journal of Materials Science*, 11(7):1270–1277, 1976.

[132] R. Steitz, V. Leiner, R. Siebrecht, and R. v. Klitzing. Influence of the ionic strength on the structure of polyelectrolyte films at the solid/liquid interface. *Colloids and Surfaces A: Physicochemical and Engineering Aspects*, 163(1):63–70, 2000.

[133] R. Steitz, W. Jaeger, and R. v. Klitzing. Influence of charge density and ionic strength on the multilayer formation of strong polyelectrolytes. *Langmuir*, 17(15): 4471–4474, 2001.

[134] H. G. M. Van de Steeg, M. A. Cohen Stuart, A. De Keizer, and B. H. Bijsterbosch. Polyelectrolyte adsorption: a subtle balance of forces. *Langmuir*, 8(10):2538–2546, 1992.

[135] W. Göpel, J. A. Anderson, D. Frankel, M. Jaehnig, K. Phillips, J. A. Schäfer, and G. Rocker. Surface defects of TiO_2 (110): A combined XPS, XAES and ELS study. *Surface Science*, 139(2–3):333–346, 1984.

[136] D. A. Shirley. High-Resolution X-Ray Photoemission Spectrum of the Valence Bands of Gold. *Physical Review B*, 5(12):4709–4714, 1972.

[137] J. Végh. The Shirley-equivalent electron inelastic scattering cross-section function. *Surface Science*, 563(1-3):183–190, 2004.

[138] J. Végh. The Shirley background revised. *Journal of Electron Spectroscopy and Related Phenomena*, 151(3):159–164, 2006.

[139] M. K. Nazeeruddin, A. Kay, I. Rodicio, R. Humphry-Baker, E. Müller, P. Liska, N. Vlachopoulos, and M. Grätzel. Conversion of light to electricity by *cis*-X_2Bis(2,2'-bipyridyl-4,4'-dicarboxylate)ruthenium(II) charge-transfer sensitizers (X= Cl^-, Br^-, I^-, CN^-, and SCN^-) on nanocrystalline TiO_2 electrodes. *Journal of the American Chemical Society*, 115(14):6382–6390, 1993.

[140] A. H. Gemeay. Adsorption Characteristics and the Kinetics of the Cation Exchange of Rhodamine-6G with Na+-Montmorillonite. *Journal of Colloid And Interface Science*, 251(2):235–241, 2002.

[141] S. Kambe, K. Murakoshi, T. Kitamura, Y. Wada, S. Yanagida, H. Kominami, and Y. Kera. Mesoporous electrodes having tight agglomeration of single-phase anatase TiO_2 nanocrystallites: Application to dye-sensitized solar cells. *Solar Energy Materials and Solar Cells*, 61(4):427–441, 2000.

[142] F. Tran-Van, M. Carrier, and C. Chevrot. Sulfonated polythiophene and poly(3,4-ethylenedioxythiophene) derivatives with cations exchange properties. *Synthetic Metals*, 142(1-3):251–258, 2004.

[143] A. Burke, S. Ito, H. Snaith, U. Bach, J. Kwiatkowski, and M. Grätzel. The Function of a TiO_2 Compact Layer in Dye-Sensitized Solar Cells Incorporating 'Planar' Organic Dyes. *Nano Letters*, 8(4):977–981, 2008.

[144] W. F. Chow. *Principles of tunnel diode circuits*. Wiley, New York, 1964.

[145] A. Hagfeldt and M. Grätzel. Molecular photovoltaics. *Accounts of Chemical Research*, 33(5):269, 2000.

[146] T. Hannappel, B. Burfeindt, W. Storck, and F. Willig. Measurement of Ultrafast Photoinduced Electron-Transfer from Chemically Anchored Ru-Dye Molecules into Empty Electronic States in a Colloidal Anatase TiO_2 Film. *Journal of Physical Chemistry B*, 101(35):6799–6802, 1997.

[147] P. Persson, M. J. Lundqvist, R. Ernstorfer, W. A. Goddard III., and F. Willig. Quantum Chemical Calculations of the Influence of Anchor-Cum-Spacer Groups on Femtosecond Electron Transfer Times in Dye-Sensitized Semiconductor Nanocrystals. *Journal of Chemical Theory and Computation*, 2(2):441–451, 2006.

[148] M. C. Neves, J. Soares, R. Hempelmann, T. Monteiro, and T. Trindade. Growth of cadmium selenide nanocrystals on submicron silica. *Journal of Crystal Growth*, 279(3-4):433–438, 2005.

[149] F. Wu, J. W. Lewis, D. S. Kliger, and J. Z. Zhang. Unusual excitation intensity dependence of fluorescence of CdTe nanoparticles. *The Journal of Chemical Physics*, 118:12, 2002.

[150] R. G. Wheeler and J. O. Dimmock. Exciton structure and zeeman effects in cadmium selenide. *Physical Review*, 125(6):1805–1815, 1962.

[151] H.-C. Ko, D.-C. Park, Y. Kawakami, S. Fujita, and S. Fujita. Self-organized CdSe quantum dots onto cleaved GaAs (110) originating from Stranski-Krastanow growth mode. *Applied Physics Letters*, 70(24):3278–3280, 1997.

[152] R. K. Swank. Surface Properties of II-VI Compounds. *Phys. Rev.*, 153(3):844–849, 1967.

[153] S. A. Choulis, M. K. Mathai, V. E. Choong, and F. So. Highly efficient organic electroluminescent device with modified cathode. *Applied Physics Letters*, 88(20): 203502, 2006.

[154] H. E. Yan, P. Lee, N. R. Armstrong, A. Graham, G. A. Evmenenko, P. Dutta, and T. J. Marks. High-performance hole-transport layers for polymer light-emitting diodes. Implementation of organosiloxane cross-linking chemistry in polymeric electroluminescent devices. *Journal of the American Chemical Society*, 127(9): 3172–3183, 2005.

[155] M. Redecker, D. D. C. Bradley, M. Inbasekaran, W. W. Wu, and E. P. Woo. High Mobility Hole Transport Fluorene-Triarylamine Copolymers. *Advanced Materials*, 11(3):241–246, 1999.

[156] J. C. Sancho-García, C. L. Foden, I. Grizzi, G. Greczynski, M. P. de Jong, W. R. Salaneck, J. L. Brédas, and J. Cornil. Joint Theoretical and Experimental Characterization of the Structural and Electronic Properties of Poly(dioctylfluorene-alt-N-butylphenyl diphenylamine). *The Journal of Physical Chemistry B*, 108 (18):5594, 2004.

[157] I. D. Parker. Carrier tunneling and device characteristics in polymer light-emitting diodes. *Journal of Applied Physics*, 75(3):1656, 1994.

[158] I. G. Hill. Molecular level alignment at organic semiconductor-metal interfaces. *Applied Physics Letters*, 73(5):662, 1998.

[159] A. L. Rogach. Nanocrystalline CdTe and CdTe(S) particles: wet chemical preparation, size-dependent optical properties and perspectives of optoelectronic applications. *Materials Science & Engineering B*, 69:435–440, 2000.

[160] B. E. McCandless, L. V. Moulton, and R. W. Birkmire. Recrystallization and sulfur diffusion in $CdCl_2$-treated CdTe/CdS thin films. *Progress in Photovoltaics Research and Applications*, 5(4):249–260, 1997.

[161] O. Vigil-Galán, A. Arias-Carbajal, R. Mendoza-Pérez, G. Santana-Rodríguez, J. Sastre-Hernández, J. C. Alonso, E. Moreno-García, G. Contreras-Puente, and A. Morales-Acevedo. Improving the efficiency of CdS/CdTe solar cells by varying the thiourea/$CdCl_2$ ratio in the CdS chemical bath. *Semiconductor Science and Technology*, 20(8):819–822, 2005.

[162] D. Briggs and M. P. Seah. *Practical surface analysis by Auger and X-ray photoelectron spectroscopy*. Wiley, New York, 1990.

[163] M. A. George, M. Azoulay, H. N. Jayatirtha, A. Burger, W. E. Collins, and E. Silberman. X-ray photoelectron spectroscopy and atomic force microscopy characterization of the effects of etching $Zn_xCd_{1-x}Te$ surfaces. *Surface Science*, 296(2):231–240, 1993.

[164] F. Yang and S. R. Forrest. Organic solar cells using transparent SnO_2-F anodes. *Advanced Materials*, 18(15):2018–2022, 2006.

[165] C. Kittel. *Introduction to solid state physics*. Wiley, New York, 1986.

[166] J. B. Baxter and E. S. Aydil. Nanowire-based dye-sensitized solar cells. *Applied Physics Letters*, 86:053114, 2005.

[167] J. Zhao, A. Wang, P. Altermatt, and M. A. Green. Twenty-four percent efficient silicon solar cells with double layer antireflection coatings and reduced resistance loss. *Applied Physics Letters*, 66:3636, 1995.

[168] F. M. Nodari, M. Koehler, M. G. E. da Luz, and L. S. Roman. Electrical aspects of photovoltaic devices based on bi-layer organic semiconducting materials. *Microelectronics Journal*, 36(11):995–997, 2005.

[169] A. J. Breeze, Z. Schlesinger, S. A. Carter, and P. J. Brock. Charge transport in TiO_2/MEH-PPV polymer photovoltaics. *Physical Review B*, 64(12):125205, 2001.

[170] A. C. Arango, L. R. Johnson, V. N. Bliznyuk, Z. Schlesinger, S. A. Carter, and H. H. Hoerhold. Efficient Titanium Oxide/Conjugated Polymer Photovoltaics for Solar Energy Conversion. *Advanced Materials*, 12(22):1689–1692, 2000.

[171] S. A. McDonald, G. Konstantatos, S. Zhang, P. W. Cyr, E. J. D. Klem, L. Levina, and E. H. Sargent. Solution-processed PbS quantum dot infrared photodetectors and photovoltaics. *Nature Materials*, 4(2):138–142, 2005.

[172] E. H. Sargent. Infrared Quantum Dots. *Advanced Materials*, 17(5):515–522, 2005.

[173] S. Günes, K. P. Fritz, H. Neugebauer, N. S. Sariciftci, S. Kumar, and G. D. Scholes. Hybrid solar cells using PbS nanoparticles. *Solar Energy Materials and Solar Cells*, 91(5):420–423, 2007.

[174] D.J. Milliron, S.M. Hughes, Y. Cui, L. Manna, J. Li, L.W. Wang, and A.P. Alivisatos. Colloidal nanocrystal heterostructures with linear and branched topology. *Nature*, 430(6996):190–195, 2004.

List of publications

Publications in refereed journals based on the present work

R. Kniprath, S. Duhm, H. Glowatzki, N. Koch, S. Rogaschewski, J. P. Rabe, and S. Kirstein. Internal Structure of Nanoporous TiO_2/Polyion Thin Films Prepared by Layer-by-layer Deposition. *Langmuir*, 23(19):9860–9865, 2007.

R. Kniprath, J. T. McLeskey Jr., J. P. Rabe, and S. Kirstein. Nanostructured solid-state hybrid photovoltaic cells fabricated by electrostatic layer-by-layer deposition. *Journal of Applied Physics*, submitted, 2008.

R. Kniprath, J. T. McLeskey Jr., D. Wang, J. P. Rabe, and S. Kirstein. Layer-by-layer deposited hybrid photovoltaic cells with II-VI quantum dot sensitizers. *Solar Energy Materials and Solar Cells*, submitted, 2008.

Other publications not directly related to the present work

A. Eisfeld, R. Kniprath, and J. S. Briggs. Theory of the absorption and circular dichroism spectra of helical molecular aggregates. *The Journal of Chemical Physics*, 126:104904, 2007.

N. Severin, S. Gröper, R. Kniprath, H. Glowatzki, N. Koch, I. M. Sokolov, and J. P. Rabe. Data scattering in scanning tunneling spectroscopy. *Ultramicroscopy*, submitted, 2008.

I. Salzmann, S. Duhm, G. Heimel, M. Oehzelt, R. Kniprath, J. P. Rabe, R. L. Johnson, and N. Koch. Tuning the ionization energy of organic-semiconductor films: The role of polar intra-molecular bonds. *Journal of the American Chemical Society*, submitted, 2008.

Presentations at scientific meetings

R. Kniprath, H. Glowatzki, S. Duhm, N. Koch, J. P. Rabe, and S. Kirstein. Composite Thin Films of Nanocrystals and Polyions for Solar Cells (Poster contribution). *Deutsche Physikalische Gesellschaft Spring Meeting*, Dresden, 2006.

R. Kniprath and S. Kirstein. Hybrid TiO_2/polyion films as porous electrodes for solar cell applications (Oral contribution). *Solar 06*, Cairo, 2006.

R. Kniprath, J. P. Rabe, and S. Kirstein. Electronic transport properties of self-assembled nanoparticle/polymer thin films (Poster contribution). *Deutsche Physikalische Gesellschaft Spring Meeting*, Regensburg, 2007.

R. Kniprath and S. Kirstein. Photovoltaic devices based on self-assembled thin films of TiO_2 nanoparticles, polymers and quantum dots (Oral contribution). *International Workshop on Spin- and Optoelectronics*, Berlin, 2007.

R. Kniprath, J. P. Rabe, and S. Kirstein. Photovoltaic effect in layer-by-layer self-assembled composite films of TiO_2 nanoparticles, polymers and quantum dots (Oral contribution). *Deutsche Physikalische Gesellschaft Spring Meeting*, Berlin, 2008.

R. Kniprath, J. T. McLeskey Jr., J. P. Rabe, and S. Kirstein. Layer-by-layer self-assembled hybrid thin films as active electrodes in photovoltaic cells (Oral contribution). *11*$^{\text{th}}$ *European Conference on Organized Films*, Potsdam, 2008.

Declaration

I declare that this thesis is a presentation of my original research work. Wherever contributions of others are involved, every effort is made to indicate this clearly, with due reference to the literature, and acknowledgement of collaborative research and discussions.

. . . . . .

Rolf Kniprath